# MECHANICS AND VIBRATION MODELING OF VERTICAL-AXIS WIND-TURBINE BLADES AND ANALYSIS OF SYSTEMS WITH PARAMETRIC EXCITATION

By

Fatemeh Afzali

A DISSERTATION

Submitted to
Michigan State University
in partial fulfillment of the requirements
for the degree of

Mechanical Engineering – Doctor of Philosophy

2023

## ABSTRACT

Wind turbines are one of the fastest-growing energy sources. Based on their axis of rotation they fall into two basic categories: horizontal-axis wind turbines (HAWTs) and vertical-axis wind turbines (VAWTs). Darrieus VAWTs exploit aerodynamic lift. This study entails the vibration analysis of large vertical-axis Darrieus wind turbine blades. Very large wind turbines are becoming more abundant due to their ability to harvest greater wind power. VAWTs are less common than HAWTs for large wind applications, but have some favorable characteristics, for example in offshore applications, and so further development of large VAWTs is anticipated. However, VAWTs are known to have vibration issues. VAWT blade vibration is the focus of this work.

The straight-bladed H-rotor/Giromill is the simplest type of VAWT. We first derive the equations of motion of a H-rotor blade modeled as a uniform straight elastic Euler-Bernoulli beam under transverse bending and twist deformation. The reduced-order model suggests the existence of periodic damping, periodic stiffness, and direct excitation generated by a cyclic aeroelastic load. The model also indicates spin softening, which could be detrimental as the turbines become large. Periodic damping and stiffness are examples of parametric excitation and are likely to carry over to other types of VAWT blades. Systems with parametric excitation have been studied with various methods. Floquet theory has been classically used to study the stability characteristics of linear systems with periodic coefficients, and has been commonly applied to Mathieu's equation, which represents a vibration system with periodic stiffness. We apply the Floquet theory combined with the harmonic-balance method to a linear vibration system with a periodic damping coefficient. Based on this theory, the approximated solution includes an exponential part, with an unknown exponent, and a periodic part. Our analysis investigates the initial conditions response, the boundaries of instability, and the characteristics of free response solution of the system. The coexistence phenomenon, in which some of the transition curves overlap

so that the instability wedges disappear, is recovered in this approach, and is examined closely.

An additional case of the parametric excitation is the combination of parametric damping and parametric stiffness. The Floquet-based analysis shows that the combined parametric excitation reshapes the stability characteristics, compared to the system with only parametric damping or stiffness and disrupts the coexistence which is observed in the parametric damping case.

The aeroelastic forces encountered by the wind turbines can cause self-excitation in blades, the mechanism of which can be loosely modeled with van-der-Pol-type nonlinearity. We seek to understand the combined effect of parametric excitation and van der Pol nonlinearity, as both can induce instabilities and oscillations. The oscillator is studied under nonresonant conditions and secondary resonances, with and without external excitation. We analyze the system using the method of multiple scales and numerical solutions. For the case without external excitation, the analysis reveals nonresonant phase drift (quasi-periodic responses), and subharmonic resonance with possible phase drift or phase locking (periodic responses). Hard excitation is treated for nonresonant conditions and secondary resonances, and similar phenomena are uncovered.

Some Darrieus VAWTs consist of curved blades. We lastly study the modal analysis of curved Darrieus wind-turbine blades and obtain the mode shapes and modal frequencies. The governing equations are derived using the fundamental deformation mechanics, and thin beam approximations are employed to express the strain and kinetic energies. The assumed-modes method is applied to the energies, and the Euler-Lagrange equation is used to discretize the equations of motion. Implementing these equations, mode shapes are calculated and mapped back onto the curved beam for visualization. This analysis is conducted for pinned-pinned and hinged-hinged blades. The results are compared with Finite element analysis using Abaqus and with the literature.

## ACKNOWLEDGMENTS

I would like to thank my highly esteemed advisor, Prof. Brian Feeny for his invaluable advice and continuous support during my PhD program. His enormous knowledge and inexhaustible experiences, enthusiasm, and kindness have encouraged me in all the time of my academic research and daily life.

My gratitude extends to Prof. Daniel Segalman for all his guidance, outstanding feedback, and exceptional support. I also thank Prof. Ahmed Naguib, and Prof. Chang Y Wang for their mentorship and being part of my committee members. I would like to thank my friends, lab mates, colleagues and research team, Wei Che Tai, Venkat Ramakrishnan, Rickey Caldwell, Gizem Dilber Acar, Mustafa Acar, Ayse Sapmaz, Mahdieh Tanha, Gaurav Chauda, Zhaobin Zhan, Jun Guo, Aakash Gupta, and Jamal Ardister, for an amusing time spent together in the lab, and in social settings, like hiking, biking, camping. Their presence made the Vib Lab a supportive, collaborative, insightful place to work along with great friendship experience.

My appreciation also goes out to my family, my parents, Mahtaj and Rahim, my sister, Zahra, and my brothers, Saeed and Reza for being the most fun family, full of joy and love. I'd like to thank my dear Ayse, Bilal, Burak, and Lena for your genuine and unconditional love and having me as your family member. My very special word of thanks goes to my dear Ehsan, for all he has done to encourage me, support me, and uplift me through my study.

This work is based on a project supported by the National Science Foundation, under grant CMMI-1435126. Any opinions, findings, and conclusions or recommendations expressed in this material are those of the author(s) and do not necessarily reflect the views of the National Science Foundation.

## TABLE OF CONTENTS

# CHAPTER 1

# INTRODUCTION

There exist several methods of absorbing wind power and converting it into a useful energy form. Wind turbines are the most popular setups to accomplish this purpose and are distinguished into two main classes depending on the orientation of the rotor: horizontal axis wind turbines (HAWTs) and vertical axis wind turbines (VAWTs). In this notation, "axis" represents the axis of rotation of the rotor (Fig. 1.1). In this study, we focus on

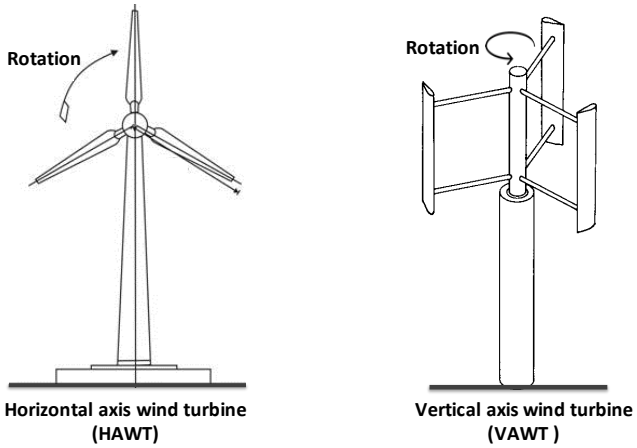


Figure 1.1: Wind turbine categories.

the VAWTs. Figure 1.2 shows different types of VAWTs configurations. They are mainly differentiated into two types based on the energy extraction from the wind: Savonius and Darrieus. Savonius wind turbines generate power using drag over the rotor, while Darrieus wind turbines use lift over the airfoil to extract energy (Fig. 1.3).

Savonius turbines are used in high-torque and low-speed applications, e.g., centrifugal ventilators and water pumping [64, 103]. This design also has been used for harnessing tidal power and for measuring ocean currents as low as 0.5 knots [31]. However they suffer from low efficiency, reported as less than half of the Betz limit [98]. The maximum power that can be extracted from the wind by a wind turbine, regardless of the design of the turbine, is indicated by Betz's law which states that wind turbines can absorb at most

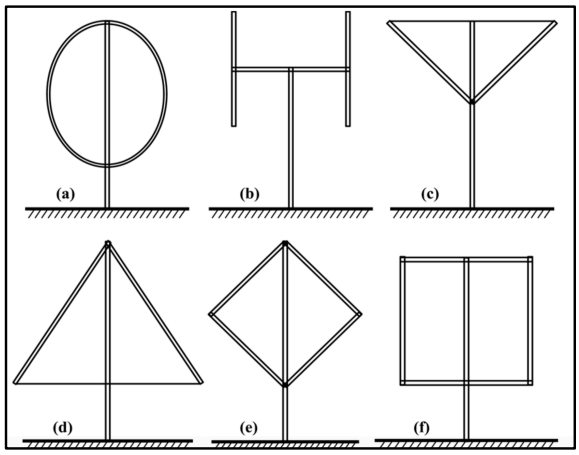


Figure 1.2: (a) "The Full-Darrieus", (b) "H", (c) "V", (d) "Δ", (e) "Diamond", (f) "Giromill".

59.3% of the kinetic energy of the wind. This is known as Betz's coefficient. In practice wind turbines reach 75 – 80% of the Betz limit at their highest. The highest efficiency of the Savonius happens at a rotational speed less than the wind speed. At higher rotational speeds the efficiency of the rotor decreases drastically. The Darrieus configuration, however, has been shown to have a much higher efficiency than the Savonius type. In some cases, the efficiency can approach the Beltz limit. Moreover, they can operate at a high rotational speed, which makes them a more desirable design candidate. The main focus of our investigation in this research is to study VAWTs with Darrieus configurations.

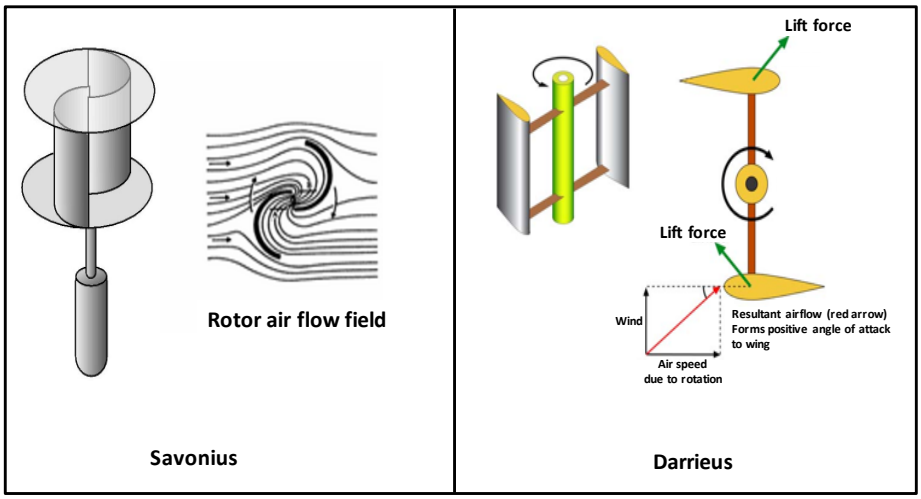


Figure 1.3: Vertical axis wind turbine categories.

## 1.1 Background

Extracting energy from the wind originated a very long time ago. Fleming and Probert [31] and Eldridge [27] declared that the vertical axis wind turbines probably originated around 200 BC in the east region of Iran, Sistan, Nashtifan, which is a sandy region and has enduring high winds. These turbines (Fig. 1.4) were used for the purpose of grinding and water pumping. However, Horwitz [41] suggested that wind turbines developed in Tibet and were rotated by vertical axis waterwheels.

Figure 1.4: Vertical axis wind turbine in Nashtifan, Iran [27].

In 1925, in France, George Jean Marie Darrieus designed a configuration of vertical axis wind turbines which was named after him as the “Darrieus configuration", and is also often known as “eggbeater windmill” [103]. The development of Darrieus turbines started in 1930s, but was stopped due to design complexity, manufacturing costs, several failures, limited funds, and more importantly HAWT success. Decrease in fuel cost lessened the interest in renewable energy and terminated the research on VAWTs, although studies on developing HAWTs continued [93]. Nonetheless, investigations on VAWTs restarted in 1970s by focusing on optimizing the design in order to have a simpler design, reduce the costs and decrease the failures. The VAWTs were under extensive development by the National Research Council of Canada (NRC) [27] and Sandia National Laboratories (SNL)

[103] in the 1970's, and then later by FloWind[1]. Due to high efficiency, SNL was mainly investigating Darrieus wind turbines, although they also studied other configurations such as Savonius. The NRC developed an experimental Darrieus VAWT and a numerical aerodynamic model [19]. At the same time the multi-megawatt VAWTs were introduced. In 1980s, NRC and Hydro-Québec (a Canadian electric-utility company) designed and constructed the world's largest Darrieus type VAWT, Éole, shown in Fig. 1.5. Nevertheless, the turbines encountered high maintenance costs and operated only from 1987 to 1993.

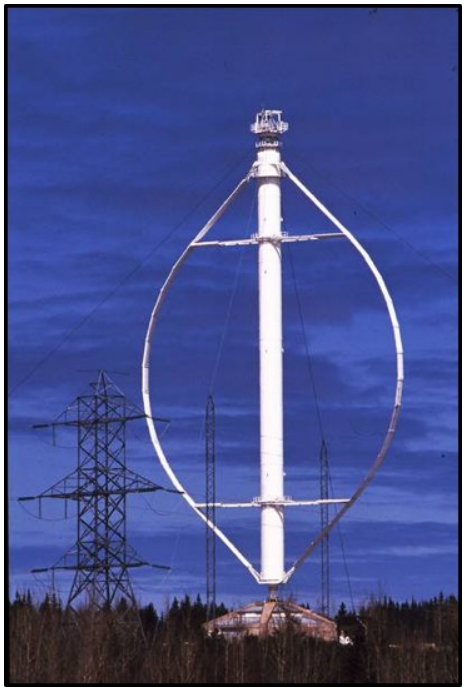

Figure 1.5: Éole, the largest VAWT, Québec, Canada [19].

Technical analyses accompanied these studies. NRC developed a numerical aerodynamic model for their VAWT studies [19].

For the Sandia VAWT, using Finite Element Analysis (FEA), the modal frequencies and shapes were determined for a single blade, and frequencies for the full system [10]. Flutter studies were also done [37]. In followup to the 17-m VAWT, a 34-m test bed

[1]Now out of business

was developed, and modal characteristics were measured and predicted by FEA [14, 103]. Damping was also estimated [48].

Recently, renewable energies have come back into focus especially for the purpose of electricity production. Wind turbines have been developed for offshore deployment due to the availability of strong winds. The first offshore wind farm, consisting of 11450 kW turbines, was created in Vindeby, Denmark, in 1991. Sandia National Laboratory and its partners (TU Delft, University of Maine, Iowa State, and TPI Composites) believe that VAWTs offer many advantages for the offshore farms [33]. For the purpose of improving VAWTs for offshore applications, the Offshore Wind ENergy Simulation (OWENS) toolkit has been developed as a design tool to analyze and determine optimized floating VAWT configurations with the collaboration of SNL and Texas A&M University [33, 76].

The performance of a Darrieus wind-turbine was first studied by Rangi and South [101] using wind tunnel measurements in the NRC of Canada. They discussed the machine design and aerodynamic efficiency under a high relative velocity. In another study Rangi and South [100] and their team investigated Darrieus turbine parameters including spoilers and aero-brake effects on turbine performance and reliability, in addition to the effect of efficiency related parameters like the number of blades and the rotor's solidity. In 1979 Kaza and Kvaternik [51] developed second-degree nonlinear aeroelastic partial differential equations of motion for a slender, flexible, non-uniform, Darrieus vertical-axis wind-turbine blade using Hamilton's principle. In this analysis they considered a blade undergoing combined flat-wise bending, edgewise bending, torsion, and extension. The blade aerodynamic loading was developed based on a quasi-steady approximation of two-dimensional incompressible unsteady airfoil theory.

Owens and Griffith [79] developed a structural dynamic design tool for large scale VAWTs for studying the effect of geometry, configuration, blade material, and number of blades on the aeroelastic stability of VAWTs. This tool can describe quantitatively

the aeroelastic instabilities in a VAWT design. Their work has addressed the modeling of aeroelastic loading and the vibration responses, ultimately for guiding the design and manufacture of VAWT systems, and has involved the development of the finite-element-based OWENS simulation toolkit, modal analysis of blade-tower systems, the potential for resonances, and field tests on the Sandia 34-m VAWT test bed [77–79].

Studying wind farms and optimizing wind-farm layout has always been of significant concern. The turbine positions and the effect of the vicinity of turbines, and therefore the wake effect downstream of a wind farm alters the power coefficient of the wind turbines [94]. Most wind farms are populated with HAWTs, for which the downstream flow is influenced by the wake effect such that it reduces the power coefficient. However, Thomas, in a US Patent study [106], indicated that in a wind farm of VAWTs (instead of HAWTs) the coupled-vortex interaction between two wind turbines with opposite rotational directions increased the aerodynamic efficiency. In a study of the wind farm layout optimization problem, Whittlesey et al. [114] investigated how the power coefficient in a VAWT farm is affected by turbine spacing. They suggested that optimally positioning the VAWTs showed a significant increase in the power output compared to the HAWTs.

## 1.2 VAWs versus HAWTs

The offshore wind energy became of interest for clean renewable electricity production in coastal regions because of the sources of wind with high speed. Furthermore, placing the wind farm in the coastal zone facilitates the transmission of energy, compared with the transmission distances from many land based farms [32, 71].

The design characteristics of the VAWTs are favorable for extracting energy from the wind in offshore regions. A typical Darrieus turbine consists of a central vertical shaft, curved or straight blades, a gearbox (speed transmission), and a generator, as shown in Fig. 1.6. There are a variety of properties of vertical axis wind turbines that advocate them for the use of offshore configurations. Figure 1.6 illustrates the characteristics of a

floating vertical axis wind turbine and compare it with the horizontal axis wind turbine. As indicated, one of the primary feature is the height of the center of gravity (C.G.) in VAWTs, compare to HAWTs. HAWTs have a high C.G. since the gearbox and generator are elevated, while in VAWTs the gearbox and generator are mounted below the rotor, lowering the C.G. This layout decreases the substructure costs [33, 103].

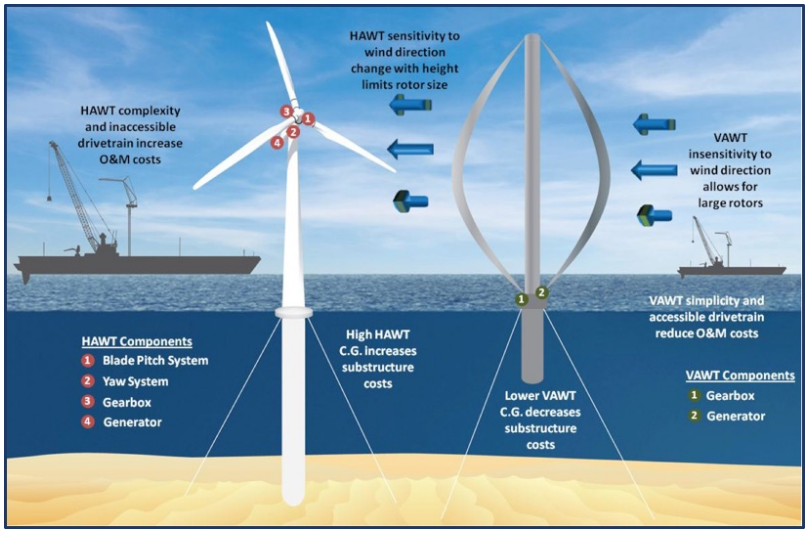


Figure 1.6: VAWT vs HAWT [63].

Another significant characteristic is the sensitivity of the wind turbines to the wind direction. HAWTs are not omni-directional in regards to wind direction and need a yaw system to extract energy from all wind directions. VAWTs are omni-directional and operate with wind in all directions and do not require a yaw system. Large scale wind turbines require large yaw systems. In consequence, the yaw of very large turbine rotors and their drive-train components increase the cost of operation and maintenance [103]. In order to produce a full Darrieus VAWT with equivalent rotor swept area as that of HAWT, the dimensions of VAWTs are approximately twice that of the HAWTs. Therefore, the cost of production of VAWTs notably increases. In order to decrease the cost there has been some modifications in the design of VAWTs, like designing the blade with a uniform chord length and using fiber-glass composites.

## 1.3 Motivation and Overview

During the past decades different sources of renewable energy have thrived but the wind power is the fastest developing form of renewable energy. Global Wind Energy Council (GWEC) produces graphs showing the exciting growth of the wind power industry around the world [24]. In Fig. 1.7, according to GWEC, by the end of 2017 the total global installed wind capacity reached about 540 GW.

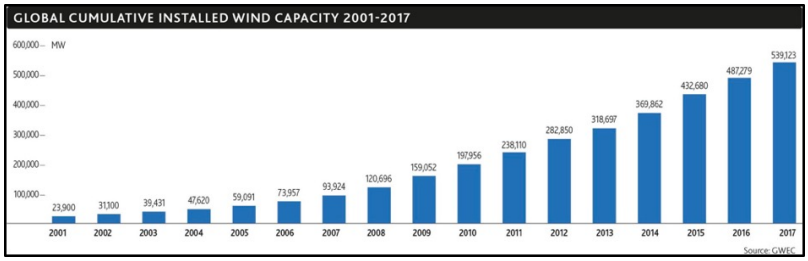


Figure 1.7: Global cumulative installed capacity 2001 – 2017[24].

At the end of 2010, the installations of global wind power was 197956 MW, which is recorded as 2% of global energy supply. A GWEC report approximated an 160% improvement in the global wind energy capacity from 2010 – 2015. However, Fig. 1.7 indicates an approximately 120% improvement in 2015 (the accumulated capacity reach 432680 MW) [102].

On the other hand, the cost of electricity generation by wind turbine can be compared with other methods of energy production. Figure 1.8 compares the cost of electricity for EU countries. The wind production cost is between 50 – 80 and 75 – 120 €/MWh for onshore and offshore, respectively [50].

The development of the offshore wind turbine, the potential to lessen the cost, increasing the efficiency, and the limited available space onshore, made the offshore wind farms become of more interest. Figure 1.9 suggests that by 2030, 400 GW (250 GW onshore and 150 GW offshore) of wind power in the EU and 20% in the USA electricity demand covered by wind power [50].

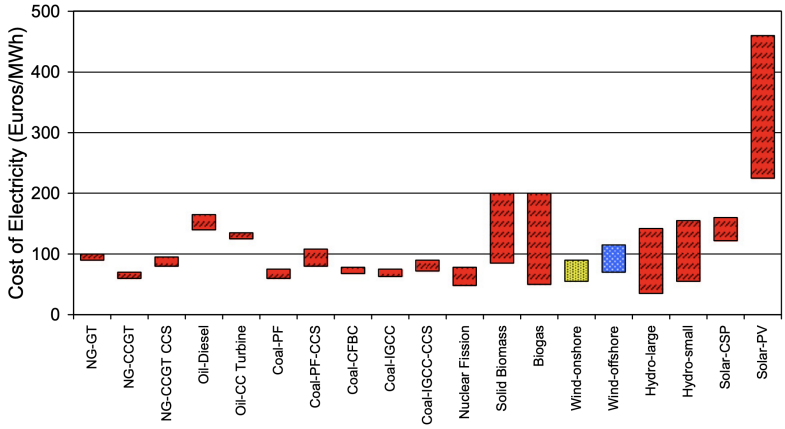


Figure 1.8: Electricity generation production cost: 2020 estimation [50].

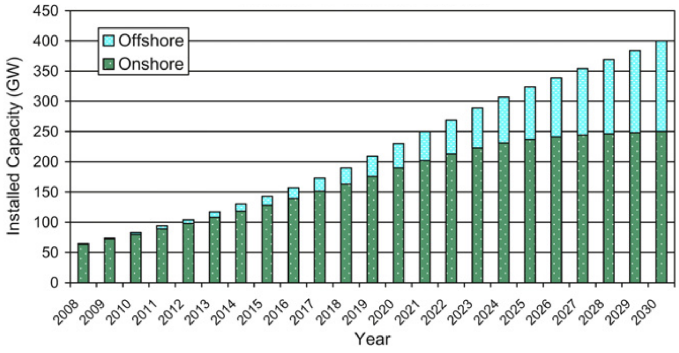


Figure 1.9: Future targets of wind energy in the EU [28, 50].

Figure 1.10 indicates that from 2011 to 2017 the world-wide offshore wind capacity increases $\approx$ 4 times. As seen in 2016 there is a total value of 4334 MW increase while 4091 units, i.e. $\approx$ 94% corresponding to UK, Germany and China.

The environmental impact by fossil fuels compared with wind turbines shows that although the wind power does not pollute the atmosphere, it comes with certain environmental impacts. The visual and noise impact and bird fatalities are big concerns associated with wind power. The life cycle of birds may be effected by wind turbines. but studies show that the number of birds killed by turbines compared to other human activities such as deforestation and urbanization is negligible (Fig. 1.11).

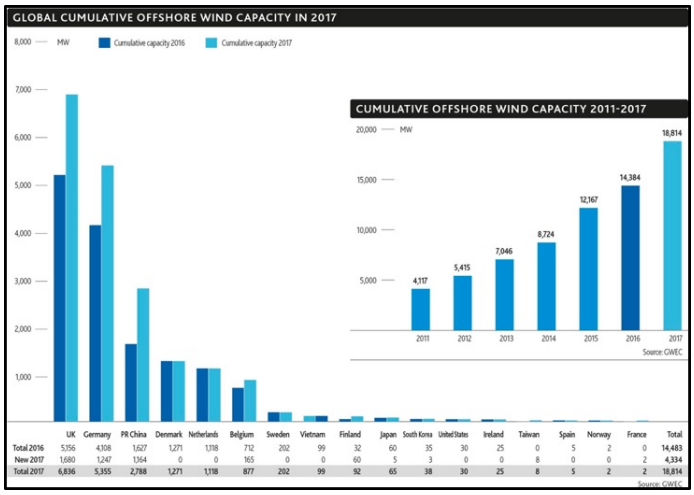


Figure 1.10: Global cumulative and annual offshore wind capacity at the end of 2017 [24].

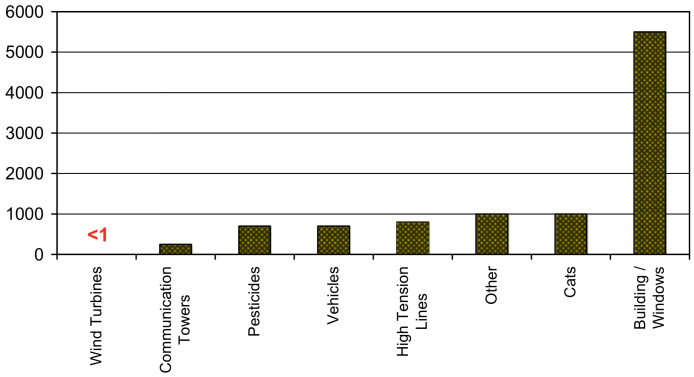


Figure 1.11: Cause of bird fatalities per 10000 fatalities [50].

## 1.4 Research Outline

One obstacle to VAWT development is the belief that VAWTs undergo large cyclic loading and thereby suffer from vibration and fatigue issues [16, 23, 29, 111]. However, not many vibration studies have been dedicated to VAWTs. Investigations suggest VAWTs over HAWTs for offshore applications but the design challenges due to the complexity of the structure should be resolved. VAWTs have a complicated 3-D dynamics which includes the fluid-structure and solid interaction, material design, manufacturing challenges, dynamics and kinematic analysis, fluid flow analysis, stable and accurate numerical solvers, parameter estimation, time varying mathematical models etc. Here we accent attention on the vertical-axis wind turbines, and simplifying the complicated dynamics to carry out analysis.

In general a wind blade can endure bend-bend-twist deflections and axial deformations. Here, we start with transverse bending and twist of a vertical, straight, uniform Euler blade. In chapter 2, a blade vibration model for an H-rotor/Giromill type VAWT considering bend and twist deflections, is formulated. An energy method is applied on an Eulerian beam under transverse bend and twist deflections to obtain the governing equations. An aero-elastic model is derived based on quasi steady airfoil theory. We formulated lift and drag forces and moments for an airfoil with changing angle of attack, where stall effects were neglected. The analysis suggested the existence of periodic damping and periodic stiffness in the equations of motion generated by a cyclic angle of attack.

To follow up these observations in chapter 3 we study a linear differential equation with parametric excitation when the excitation is through damping coefficient. For this purpose, we use a Floquet solution combined with harmonic balance method and study the stability and response characteristics of the system.

Since the study in chapter 2 also indicated small levels of parametric stiffness in the example studied, in chapter 4, we address parametric excitation through stiffness. For dynamical interest, we include two-harmonics. We use the Floquet solution combined with harmonic balance, as done in chapter 3, to analyze the response and stability characteristics.

Superposition is not applicable in studying systems with parametric excitation. Therefore various combinations of the cyclic excitation cannot be obtained from individual studies of cyclic stiffness and cyclic damping, and must be analyzed specifically. In chapter 5 we focus on a system with a combination of parametric damping and stiffness. We study this system using an analysis based on Floquet theory. We aim to uncover how the cyclic stiffness and damping combine and together affect the initial conditions responses and stability.

In chapter 6 we study the responses of an oscillator with van der Pol terms, parametric damping and direct excitation. A potential application of this system is a vertical-axis

wind-turbine blade, which can endure direct excitation and parametric damping, as well as aeroelastic self-excitation, the mechanism of which can be loosely modeled with van-der-Pol-type nonlinearity. Here, the general behavior of this system is studied, rather than the specific responses of a specific model of an application system. As both parametric excitation and van-der-Pol nonlinearity can induce instabilities and oscillations, we seek to understand the combined effect of such terms in this system. We apply the first-order method of multiple scales to probe an unforced and externally forced van der Pol equation with parametric damping. We study the sub-harmonic resonance of order $1/2$ as well as the nonresonant dynamics.

The study on straight blades indicated that vibration problems are inherent for large blades under spinning conditions unless structural stiffening is added. Curved blades are likely to have spin stiffening. As such, we are motivated to study the vibration modeling of curved blades of Darrieus turbines. Modal analysis of vertical axis wind turbine blades is studied in chapter 7, where the Darrieus wind turbine blade is modeled as a curved beam. The blade experiences in-plane and out-of-plane bending, axial extension, and twist around the shear center. The dynamics of the blade is derived from the fundamental mechanics of strain, and is compared to a finite element model. Assumed-modes method is applied to the differential equations and the modal frequencies and mode shapes for the associated curved beam are obtained.

In the last chapter we aim to develop an analytical model for the vibration of a generalized curved beam with a variable-curvature profile, symmetric or asymmetric cross section with uniform or non-uniform cross sectional areas, and various boundary conditions, with or without the external forces, under bend-bend-twist-extend deformations. That is, deformation variables include flatwise (about the axis of minimum second moment of cross sectional area) and edgewise (about the axis of maximum second moment of cross sectional area) bending, torsion (about the centroidal axis), and axial extension. Lateral

shear (such as in a Timoshenko beam [66]) is neglected. The work starts by following [51], but includes some features not included in this reference. Other work on curved slender beams includes [118, 119], which focused on in-plane motion.

The differential equations of motion are discretized using the Rayleigh-Ritz method and “assumed-mode" basis functions [66], and Euler-Lagrange equations are applied to obtain a multi-degree-of-freedom model in terms of the assumed-modal coordinates. We linearize the equations of motion and apply modal analysis to find the modal frequencies and mode shapes. The structure of the curved beam imposes coupling between the deformations, and hence the modes of vibration involve combinations of deformation variables. For numerical studies, the specific case is examined where the beam is modeled as a curved beam with half-circular profile and a symmetric uniform cross section.

After obtaining the modal frequencies and modal vectors from the assumed-modes multi-degree-of-freedom approximation, the mode shapes are reconstructed in terms of the original bend-bend-twist-extend variables to illustrate the modal deformations. The results for the modal frequencies, normal modes and the deformed configurations of curved beam with different boundary conditions (pin-pin and clamp-clamp) are obtained and compared with the FE analysis performed in Abaqus and also those reported in literature.

## CHAPTER 2

## VIBRATION ANALYSIS OF H-ROTOR/GIROMILL WIND TURBINE BLADES

VAWTs are designed such that the blades may be supported at the endpoints or interior points (H-rotor/Giromill). We consider a blade supported at the endpoints. The strut supports provide an axial and torsional stiffness to the blade at its connection points. As such, the blade is modeled as a pin-and-spring supported beam at distance $R$ from the axis of rotation under transverse displacement ($y(x,t)$) and twist ($\psi(x,t)$) where $x$ is a point along the axis of the blade (Fig. 2.1).

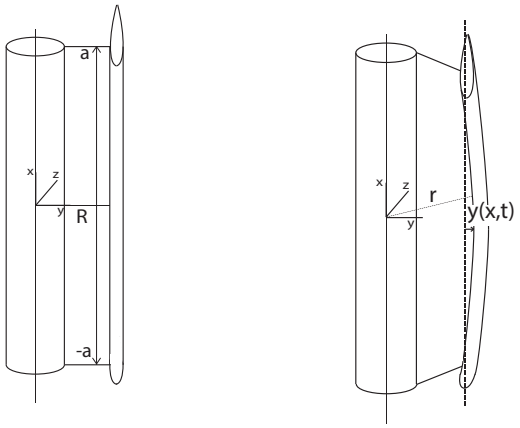


Figure 2.1: H-rotor/Giromill wind turbine.

Kinetic and potential energies for an arbitrary point on the beam are expressed such that the extended Hamilton's principle can be used to obtain the partial differential equations of motion. Alternatively, a Lagrange formulation based on assumed modes can be applied to the energy terms. The position of point $x$ on the undeformed beam from an origin at the center of the rotor and in line with the center of mass of the beam in the undeformed state is

$$\vec{r}(x,t) = (x - s(x,t))\vec{i} + (R + y(x,t))\vec{e}_r \tag{2.1}$$

where $s(x,t) \cong \int_0^x (\frac{y'^2}{2} + \frac{y'^4}{8})dz$ is the foreshortening term for an Euler-Bernouli beam [84].

From Eqn. (2.1) the velocity is

$$\vec{v_b} = \vec{\dot{r}} = -\dot{s}\vec{i} + \dot{y}\vec{e}_r + \Omega(y(x,t) + R)\vec{k}, \tag{2.2}$$

where $\Omega$ is the rotor speed. For steady rotor speed, $\Omega$, and neglecting the effects of transverse deflection in the circumferential direction on the energy, the kinetic energy of the particles on the beam can be formulated as

$$T = \int_{-a}^{+a} \frac{1}{2} m(x) v_b(x,t)^2 dx + \int_{-a}^{+a} \frac{1}{2} I_{xx}(x)(\dot{\psi} + \Omega)^2 dx + \frac{1}{2} I_0 \Omega^2, \tag{2.3}$$

where $I_0$ is mass moment of inertia of the rotor, $m(x)$ is mass per unit length of the beam and $I_{xx}$ is mass moment of inertia per unit length about the twist axis, $x$, through the blade-section center of mass. Similarly, potential energy can be formulated as the summation of the gravitational potential energy, $V_{mg}$, strain energy due to nonlinear bending [21] and twist, $V_s$, and the elastic potential energy of the boundaries of the beam, $V_b$ as

$$V_{mg} = \int_{-a}^{+a} m(x) g(x - s(x,t)) dx, \tag{2.4}$$

$$V_s = \int_{-a}^{+a} \frac{1}{2} E I_z(x) [y''^2 (1 - 3y'^2)] dx + \int_{-a}^{+a} \frac{1}{2} G J_{xx}(x) \psi'^2 dx, \tag{2.5}$$

$$V_b = \frac{1}{2} k_1 (u_g - s(-a,t))^2 + \frac{1}{2} k_{T_1} (y'(-a,t))^2 + \frac{1}{2} k_2 (u_g - s(a,t))^2 + \frac{1}{2} k_{T_2} (y'(a,t))^2 \tag{2.6}$$

These energies accommodate nonlinear bending strain and nonlinear foreshortening up to the cubic term.

## 2.1 Reduced Order Modeling

In this section, the bend and twist deformation of the blade (Fig. 2.2) is projected onto the assumed modes based on hinged-hinged beam modes and results in the second-order nonlinear ordinary differential equations. By considering assumed mode formulation [68], we let

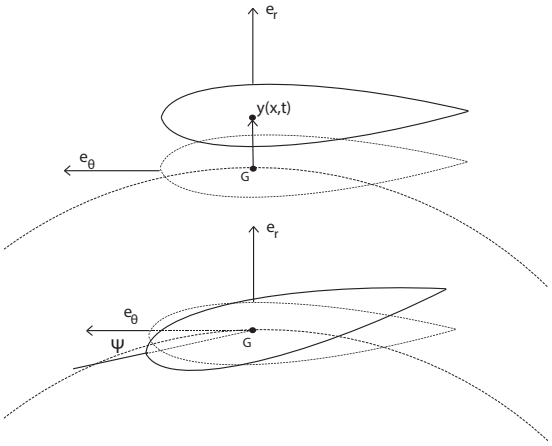


Figure 2.2: Top view representation of transverse deflection on top and twist on bottom.

$$y(x,t) \cong \sum_{i=1}^{N_b} q_i(t)\xi_i(x), \tag{2.7}$$

$$\psi(x,t) \cong \sum_{i=1}^{N_t} b_i(t)\rho_i(x), \tag{2.8}$$

where $N_b$ is the number of modes in bending displacement, $N_t$ is the number of modes in twist and $N = N_b + N_t$ is the total number of assumed modes. $\xi_i(x)$ and $\rho_i(x)$ are respectively, the bend and twist assumed modal functions, and $q_i(t)$ and $b_i(t)$ are the respective assumed modal coordinates. For a single assumed modes assumption, $N_t = N_b = 1$,

$$y(x,t) \approx q(t)\xi(x), \tag{2.9}$$

$$\psi(x,t) \approx b(t)\rho(x). \tag{2.10}$$

Substituting Eqns. (2.9) and (2.10) into (2.3)-(2.6), the energy expressions are

$$\begin{aligned} T(q,\dot{q},b,\dot{b},t) &= \int_{-a}^{+a} \frac{1}{2} I_{xx}(x) \left(\dot{b}(t)\rho(x) + \Omega\right)^2 dx + \int_{-a}^{+a} \frac{1}{2} m(x) \left((-\dot{s})^2 + (\dot{q}(t)\xi(x))^2\right. \\ &+ \left.(\Omega(q(t)\xi(x) + R))^2\right) dx + \frac{1}{2} I_o \Omega^2, \end{aligned} \tag{2.11}$$

$$V_{mg}(q,\dot{q},t) = \int_{-a}^{+a} m(x)g(x - s(q,\dot{q},t)dx, \tag{2.12}$$

$$\begin{aligned} V_s(q,\dot{q},b,\dot{b},t) &= \int_{-a}^{+a} \frac{1}{2} EI_z(x)[\left(q(t)\xi''(x)\right)^2 + \left(1 - 3\left(q(t)\xi'(x)\right)^2\right)]dx \\ &+ \int_{-a}^{+a} \frac{1}{2} GJ_{xx}(x)\left(b(t)\rho'(x)\right)^2 dx, \end{aligned} \tag{2.13}$$

$$\begin{aligned} V_b(q,\dot{q},b,\dot{b},t) &= \frac{1}{2}k_1\left(u_g - s(-a,t)\right)^2 + \frac{1}{2}k_{T_1}\left(q(t)\xi'(-a)\right)^2 + \frac{1}{2}k_2\left(u_g - s(a,t)\right)^2 \\ &+ \frac{1}{2}k_{T_2}\left(q(t)\xi'(a)\right)^2. \end{aligned} \tag{2.14}$$

Lagrange's equation is applied on the energy of the system in modal coordinates. The generalized forces, $Q_q$ and $Q_b$ are obtained from the virtual work of the non-conservative forces expressed as

$$\delta W_{nc} = Q_q \delta q + Q_b \delta b, \tag{2.15}$$

where $Q_q$ and $Q_b$ accommodate the non-conservative aeroelastic forces. The resulting equations of motion are

$$\begin{aligned} & 2q\dot{q}^2 \int_{-a}^{a} m(x)\left[\int_0^x (\xi')^2 dz\right]^2 dx + q^2\ddot{q}\int_{-a}^{a} m(x)\left[\int_0^x (\xi')^2 dz\right]^2 dx + \ddot{q}\int_{-a}^{a} m(x)\xi^2 dx \\ - & q\dot{q}^2 \int_{-a}^{a} m(x)\left[\int_0^x (\xi')^2 dz\right]^2 dx - q\int_{-a}^{a} m(x)\Omega^2\xi^2 dx - q\int_{-a}^{a} gm(x)\left[\int_0^x (\xi')^2 dz\right] dx \\ - & q^3 \int_{-a}^{a} g\frac{m(x)}{2}\left[\int_0^x (\xi')^4 dz\right] dx - \int_{-a}^{a} m(x)\Omega^2 R\xi dx + q\int_{-a}^{a} EI_z(x)\xi''^2 dx \\ - & q^3 \int_{-a}^{a} 6EI_z(x)\xi''^2\xi'^2 dx + q^3\frac{k_1 + k_2}{2}\left[\int_0^{\pm a} (\xi')^2 dx\right]^2 + q(k_{T_1} + k_{T_2})(\xi'|_{\pm a})^2 = Q_q, \end{aligned} \tag{2.16}$$

$$\ddot{b}\int_{-a}^{a} I_{xx}\rho^2 dx + b\int_{-a}^{a} J_{xx}G\rho'^2 dx = Q_b. \tag{2.17}$$

## 2.2 Aeroelastic Modeling

Under a constant rotation rate of the rotor and blades, the relative velocity and angle of the wind hitting the blade is changing periodically and creates cyclic lift and drag forces and moments on the blade. These forces are associated with the nonconservative work, $W_{nc}$, in Hamilton's or Lagrange's principle.

In order to simplify the aeroelastic model, the assumption is a flow field with constant direction and velocity. This assumption also neglects the effects of the blades on the fluid particles. Blades have their own velocity due to rotation and deflection. Therefore the relative flow velocity (to the airfoil) has a cyclic and displacement dependent behavior. For now we apply a very simple "quasi steady" aeroelastic model. This approximation will not capture some effects such as hysteresis and reduced frequency [49, 56]. In this method, lift and drag are formulated using an instantaneous airfoil model.

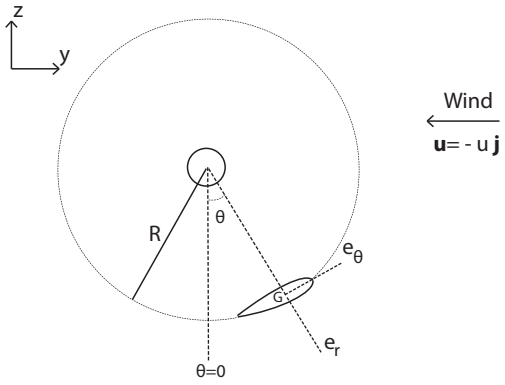


Figure 2.3: Cross section of VAWT showing the coordinate axis.

Figure 2.3 shows a sketch of the turbine rotating under the effect of constant wind speed $u$, such that the wind velocity is $\mathbf{u} = -u\mathbf{j}$, where $\mathbf{j}$ is a unit vector in $y$ direction. Note that in Fig. 2.3, $y$ axis is fixed and is not to be confused with transverse deflection, $y(x,t)$, which is in the $\mathbf{e}_r$ direction that rotates with the turbine. $\mathbf{e}_r$ and $\mathbf{e}_\theta$ are radial and tangential

unit vectors and $\theta$ is the coordinate that represents the orientation of the unit vector $\mathbf{e}_\theta$ with respect to the $y$-axis, therefore, $\mathbf{j} = \mathbf{e}_r \sin\theta + \mathbf{e}_\theta \cos\theta$. The constant $\dot{\theta} = \Omega$ gives $\dot{\mathbf{e}}_r = \dot{\theta}\mathbf{e}_\theta$ and $\dot{\mathbf{e}}_\theta = -\dot{\theta}\mathbf{e}_r$

The planar flow velocity relative to the blade (neglecting the $x$ component) is obtained as $\mathbf{v} = \mathbf{u} - \mathbf{v}_b = -u\mathbf{j} - \mathbf{v}_b$, and hence using Eqns. (2.1) and (2.2),

$$\mathbf{v} = -[\dot{y} + u\sin\theta]\mathbf{e}_r - [(R+y)\dot{\theta} + u\cos\theta]\mathbf{e}_\theta \tag{2.18}$$

As shown in Fig. 2.4, $\phi$ denotes the angle between the relative flow velocity and tangential axis $\mathbf{e}_\theta$, where

$$\tan\phi = \mathbf{v}_r/\mathbf{v}_\theta = \frac{\dot{y} + u\sin\theta}{(R+y)\dot{\theta} + u\cos\theta} \tag{2.19}$$

So the angle of attack, $\alpha$, is $\alpha = \psi + \beta + \phi$, where, $\psi$ is the twist deformation angle and $\beta$ is the pretwist angle which is considered to be zero.

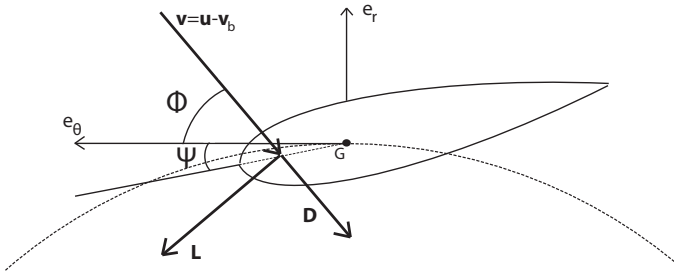


Figure 2.4: Twist angle $\psi$ and relative wind angle $\phi$, for the case when the pretwist $\beta = 0$.

Applying the Taylor series expansion for small values of $\mathbf{v}_r/\mathbf{v}_\theta$ to expand the angle $\phi$ we have

$$\phi = \arctan\frac{\dot{y} + u\sin\theta}{(R+y)\dot{\theta} + u\cos\theta} \approx \frac{\dot{y} + u\sin\theta}{(R+y)\dot{\theta} + u\cos\theta} - \frac{1}{3}\left(\frac{\dot{y} + u\sin\theta}{(R+y)\dot{\theta} + u\cos\theta}\right)^3. \tag{2.20}$$

The small $\phi$ assumption should be valid for typical operation condition; for which the tip speed ($R\dot{\theta}$) is larger than wind speed (u), (approximately 5 times). Equation (2.20) is plugged into the lift and drag forces formula and the forces per unit length acting on the blade are obtained,

$$\vec{L} = \frac{1}{2} C_L(\alpha) c \rho v^2 (-\cos\phi \vec{e_r} + \sin\phi \vec{e_\theta}) = L_r \vec{e_r} + L_\theta \vec{e_\theta} \tag{2.21}$$

$$\vec{D} = \frac{1}{2} C_D(\alpha) c \rho v^2 (-\sin\phi \vec{e_r} - \cos\phi \vec{e_\theta}) = D_r \vec{e_r} + D_\theta \vec{e_\theta}, \tag{2.22}$$

where $C_L$ and $C_D$ coefficients of lift and drag, respectively, are functions of $y, \dot{y}$ and $\psi$, through the angle of attack, as

$$C_L \approx c_1 \alpha(y, \dot{y}, \psi) + c_3 \alpha(y, \dot{y}, \psi)^3 \tag{2.23}$$

$$C_D \approx c_0 + c_2 \alpha(y, \dot{y}, \psi)^2 \tag{2.24}$$

and coefficients $c_i$ are found by curve fitting. In the case of transverse deflection and twist, the lift and drag forces and moments contribute to the $\delta\hat{W}_{nc}$ terms as

$$\delta\hat{W}_{nc} = \hat{f}_y(y, \dot{y}, \psi, t)\delta y + \hat{M}_y(y, \dot{y}, \psi, t)\delta\psi \tag{2.25}$$

which define the radial forces as

$$\hat{f}(y, \dot{y}, \psi, t) = L_r(y, \dot{y}, \psi, t) + D_r(y, \dot{y}, \psi, t) \tag{2.26}$$

and a lift moment function $\hat{M}$ as

$$\hat{M}(y, \dot{y}, \psi, t) = (L\cos\alpha + D\sin\alpha)\, l_c \tag{2.27}$$

where $l_c$ is the distance between the aerodynamic center of the airfoil and its center of gravity, while lift and drag are cyclic functions. Applying the multi-variable Taylor series expansion up to cubic terms on the functions $\hat{f}(y, \dot{y}, \psi, t)$ and $\hat{M}(y, \dot{y}, \psi, t)$ around

$(y,\dot{y},\psi)$=(0,0,0) yields

$$\begin{aligned}\hat{f}_y(y,\dot{y},\psi,t) &= \hat{f}_{000} + \hat{f}_{100}y + \hat{f}_{010}\dot{y} + \hat{f}_{001}\psi + \hat{f}_{200}y^2 + \hat{f}_{020}\dot{y}^2 + \hat{f}_{002}\psi^2 \\ &+ \hat{f}_{110}y\dot{y} + \hat{f}_{101}y\psi + \hat{f}_{011}\dot{y}\psi + \hat{f}_{300}y^3 + \hat{f}_{030}\dot{y}^3 + \hat{f}_{003}\psi^3 + \hat{f}_{210}y^2\dot{y} + \hat{f}_{201}y^2\psi \\ &+ \hat{f}_{021}\dot{y}^2\psi + \hat{f}_{120}y\dot{y}^2 + \hat{f}_{102}y\psi^2 + \hat{f}_{012}\dot{y}\psi^2 + \hat{f}_{111}y\dot{y}\psi \end{aligned} \tag{2.28}$$

$$\begin{aligned}\hat{M}_y(y,\dot{y},\psi,t) &= \hat{M}_{000} + \hat{M}_{100}y + \hat{M}_{010}\dot{y} + \hat{M}_{001}\psi + \hat{M}_{200}y^2 + \hat{M}_{020}\dot{y}^2 + \hat{M}_{002}\psi^2 \\ &+ \hat{M}_{110}y\dot{y} + \hat{M}_{101}y\psi\hat{M}_{011}\dot{y}\psi + \hat{M}_{300}y^3 + \hat{M}_{030}\dot{y}^3 + \hat{M}_{003}\psi^3 + \hat{M}_{210}y^2\dot{y} \\ &+ \hat{M}_{201}y^2\psi + \hat{M}_{021}\dot{y}^2\psi + \hat{M}_{120}y\dot{y}^2 + \hat{M}_{102}y\psi^2 + \hat{M}_{012}\dot{y}\psi^2 + \hat{M}_{111}y\dot{y}\psi \end{aligned} \tag{2.29}$$

When $\Omega$ is constant, coefficients $\hat{f}_{ijk}(x,t)$ and $\hat{M}_{ijk}(x,t)$ are time periodic and functions of $x$. The virtual work terms in Hamilton's principle are found by plugging $y = q(t)\xi(x)$ and $\psi = b(t)\rho(x)$ in Eqns. (2.25), (2.28) and (2.29), to write $\hat{f}_y(y(q,\xi(x)),\dot{y}(\dot{q},\xi(x)),\psi(b,\rho(x)),t) = \hat{f}_q(q,\dot{q},b,t;x)$, and $\hat{M}_y(y(q,\xi(x)),\dot{y}(\dot{q},\xi(x)),\psi(b,\rho(x)),t) = \hat{M}_q(q,\dot{q},b,t;x)$. Then the coefficients in force and moment terms are integrated along the length of the blade to derive

$$\begin{aligned}\int_{-a}^{a}\hat{f}_q(q,\dot{q},b,t;x)\xi(x)dx &= f_{000} + f_{100}q + f_{010}\dot{q} + f_{001}b + f_{200}q^2 + f_{020}\dot{q}^2 \\ &+ f_{002}b^2 + f_{110}q\dot{q} + f_{101}qb + f_{011}\dot{q}b + f_{300}q^3 + f_{030}\dot{q}^3 + f_{003}b^3 + f_{210}q^2\dot{q} \\ &+ f_{201}q^2b + f_{021}\dot{q}^2b + f_{120}q\dot{q}^2 + f_{102}qb^2 + f_{012}\dot{q}b^2 + f_{111}q\dot{q}b, \end{aligned} \tag{2.30}$$

and

$$\begin{aligned}\int_{-a}^{a}\hat{M}_q(q,\dot{q},b,t;x)\rho(x)dx &= M_{000} + M_{100}q + M_{010}\dot{q} + M_{001}b + M_{200}q^2 \\ &+ M_{020}\dot{q}^2 + M_{002}b^2 + M_{110}q\dot{q} + M_{101}qb + M_{011}\dot{q}b + M_{300}q^3 + M_{030}\dot{q}^3 \\ &+ M_{003}b^3 + M_{210}q^2\dot{q} + M_{201}q^2b + M_{021}\dot{q}^2b + M_{120}q\dot{q}^2 + M_{102}qb^2 \\ &+ M_{012}\dot{q}b^2 + M_{111}q\dot{q}b, \end{aligned} \tag{2.31}$$

where the coefficients $f_{ijk}(t)$ and $M_{ijk}(t)$ are cyclic in time and can be related to $\hat{f}_{ijk}$ and $\hat{M}_{ijk}$. For example $f_{111}(t) = \int_{-a}^{a}\hat{f}_{111}(x,t)(\xi(x))^2(\rho(x))dx$. Using Eqns. (2.9) and

(2.10), $\delta y = \xi(x)\delta q$ and $\delta\psi = \rho(x)\delta b$, the non-conservative work in Eqn. (2.25) can be expressed as

$$\delta\hat{W}_{nc} = \hat{f}_q(q, \dot{q}, b, t; x)\xi(x)\delta q + \hat{M}_q(q, \dot{q}, b, t; x)\rho(x)\delta b \tag{2.32}$$

Based on Eqn. (2.32) the generalized forces in Eqns. (2.16) and (2.17) in modal coordinate system have the form

$$Q_q = \int_{-a}^{a} \hat{f}_q(q, \dot{q}, b, t; x)\xi(x)dx, \tag{2.33}$$

$$Q_b = \int_{-a}^{a} \hat{M}_q(q, \dot{q}, b, t; x)\rho(x)dx, \tag{2.34}$$

which are in terms of the expansions in Eqns.(2.30) and (2.31).

## 2.3 Linearization

We attained a formulation of equations of motion that accommodate cubic nonlinearity and conduct a simple initial numerical analysis and simulate the linearized model. Several linearization methods were discussed in order to decrease the complexity of the model.

Since the system of (2.16) and (2.17) has direct periodic excitation via $f_{000}(t)$ and $M_{000}(t)$, equilibria do not exist. To find the “unforced" equilibria, the direct excitation is dropped. The resulting equations are nonlinear, with many terms, and with parametric excitation. Considering the case that all cyclic time varying terms are omitted, the resulting equations are still nonlinear with many terms, and so the equilibrium will be difficult to express and use as a reference point. As such, the linearization is to be performed about the equilibrium of the non rotating system, which is zero. Thus, the “linearized" model is obtained by assuming small $y$ and $\psi$. Hence quadratic and cubic terms in $q$ and $b$ and their derivatives are dropped. The resulting equations for small deflections of the rotating system within direct and parametric excitations are

$$\ddot{q}(t) + \omega_q^2 q(t) + a_1(t)q(t) + a_2(t)\dot{q}(t) + a_3(t)b(t) = a_0 + f_0(t) \tag{2.35}$$

$$\ddot{b}(t) + \omega_b^2 b(t) + e_1(t)q(t) + e_2(t)\dot{q}(t) + e_3(t)b(t) = e_0 + g_0(t) \tag{2.36}$$

where

$$a_0 = \frac{\int_{-a}^{a} m\Omega^2 \xi R dx}{\int_{-a}^{a} m\xi^2 dx}\,, \quad a_1(t) = \frac{\int_{-a}^{a} \hat{f}_{q100}\xi^2(x)dx}{\int_{-a}^{a} m\xi^2 dx}\,, \quad a_2(t) = \frac{\int_{-a}^{a} \hat{f}_{q010}\xi^2(x)dx}{\int_{-a}^{a} m\xi^2 dx}$$
$$a_3(t) = \frac{\int_{-a}^{a} \hat{f}_{q001}\xi(x)\rho(x)}{\int_{-a}^{a} m\xi^2 dx}\,, \quad f_0(t) = \frac{-\int_{-a}^{a} \hat{f}_{q000}\xi(x)dx}{\int_{-a}^{a} m\xi^2 dx} \tag{2.37}$$

$$\omega_q^2 = \frac{-\int_{-a}^{a} m\Omega^2\xi(x)^2 dx - \int_{-a}^{a} gm\left(\int_0^x \xi(x)'^2 dz\right)dx}{\int_{-a}^{a} m\xi(x)^2 dx}$$
$$+ \quad \frac{\int_{-a}^{a} EI_z(x)\xi(x)''^2 dx + k_T\left[(\xi(x)'|_{-a})^2 + (\xi(x)'|_a)^2\right]}{\int_{-a}^{a} m\xi(x)^2 dx}$$

and,

$$e_0 = 0\,, \quad e_1(t) = \frac{-\int_{-a}^{a} \hat{M}_{q100}\xi(x)\rho(x)dx}{\int_{-a}^{a} I_{xx}\rho^2 dx}\,, \quad e_2(t) = \frac{-\int_{-a}^{a} \hat{M}_{q010}\xi(x)\rho(x)dx}{\int_{-a}^{a} I_{xx}\rho^2 dx}$$
$$e_3(t) = \frac{-\int_{-a}^{a} \hat{M}_{q001}\rho(x)^2}{\int_{-a}^{a} I_{xx}}\,, \quad g_0(t) = \frac{\int_{-a}^{a} \hat{M}_{q000}\rho(x)dx}{\int_{-a}^{a} I_{xx}\rho^2 dx}\,, \quad \omega_b^2 = \frac{\int_{-a}^{a} J_{xx}G(\rho')^2 dx}{\int_{-a}^{a} I_{xx}\rho^2 dx}$$

### 2.3.1 Blade with Quasi-steady Aeroelastic Airfoil Model

The time varying lift and drag coefficients with varying angle of attack vary with the type of blade used. Figure 2.5 indicates the lift and drag coefficients with angle of attack for a NACA0012 airfoil. From Eqns. 2.23 and 2.24 and curve fitting the data points, the lift and drag coefficients are approximated as

$$C_L(\alpha) \approx 4.4287\alpha - 2.9916\alpha^3, \tag{2.38}$$

$$C_D(\alpha) \approx 0.0094 + 1.185\alpha^2. \tag{2.39}$$

These relations contribute to load coefficients $f_{ijk}$ in Eqns. (2.30) and (2.31) by means of (2.19)-(2.24). As such, the coefficients shown in Eqns. (2.35) and (2.36) are listed for

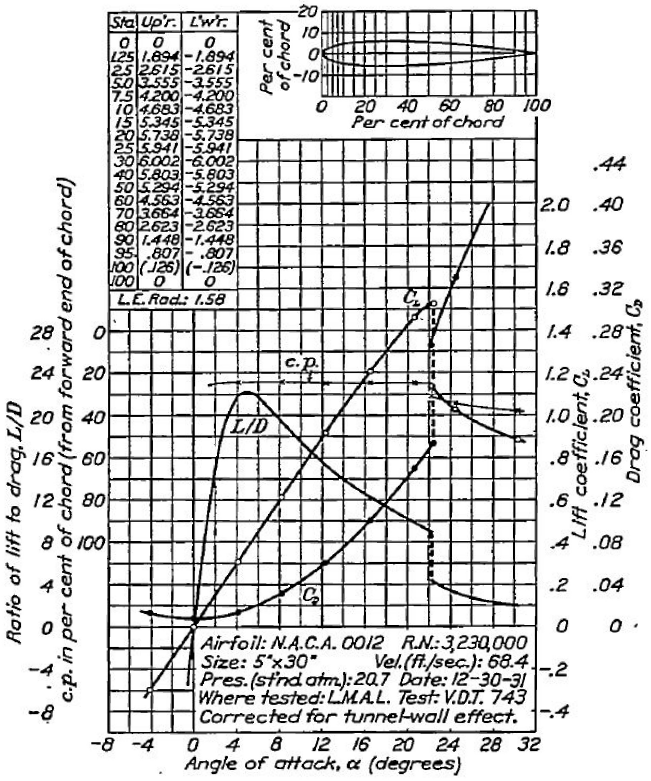


Figure 2.5: NACA0012 $C_L$ and $C_D$ values with respect to angle of attack [47].

specified values of parameters, but for arbitrary $\Omega$, $u$, and $a$. The coefficients $a_1(t)$ through $a_3(t)$ and $e_1(t)$ through $e_3(t)$ are complicated functions of time, each with fundamental frequency $\Omega$ and harmonics representing parametric excitation terms. The terms $a_0$ and $f_0(t)$ and $e_0$ and $g_0(t)$ represent constant plus periodic direct excitation.

## 2.4 Numerical Analysis and Simulation

Formulating the energy equations and modeling the non-conservative forces, the equations of motion were obtained. These equations are then used to make a vibration simulation and numerical analysis for the blade. Instead of focusing on the effects of different variables on VAWT blade vibration, the focus would be on simulating the behavior of a selected type of blade and accommodate reliability of our models.

### 2.4.1 Case Studies

Among the numerous existing configurations, we investigate the Giromill/H-rotors, which are common types of Darrieus turbines, due to their simplicity. In this study, the energy and aeroelastic models are based on Giromill style VAWTs, with straight blades parallel to the axis of rotation [103] (Fig. 2.7). Since we do not have access to a benchmark Giromill model, a set of parameters from the Sandia 17-m "egg-beater" style Darrieus turbine is taken as a reference [116, 117].

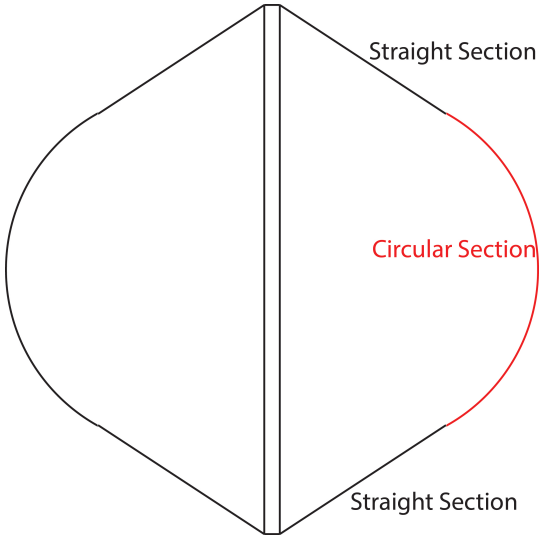


Figure 2.6: Sandia 17-m front view(Darrieus turbine).

Experimental data obtained from Sandia 17-m indicates the maximum turbine performance is obtained around a tip ratio, $R\Omega/u$, of 5 [116, 117]. According to Sandia's performance tests we can assume a constant rate of rotation of 37 revolutions per minute, or similarly $\Omega = 3.875$ rad/s, as a representative example for the numerical study which provides with the velocity of wind $u \approx 4.7$ m/s.

For a half circle shape for the Sandia 17-m blade, one can calculate an average radius either for the lift force, $L$, or effective torque by lift on rotor, $T$. Our calculations offered an average radius of 19.40 ft and 20.62 ft in order to obtain the same lift and the same torque on rotor, respectively. Referring to the calculated values, $R = 20$ ft (6m) is picked for our

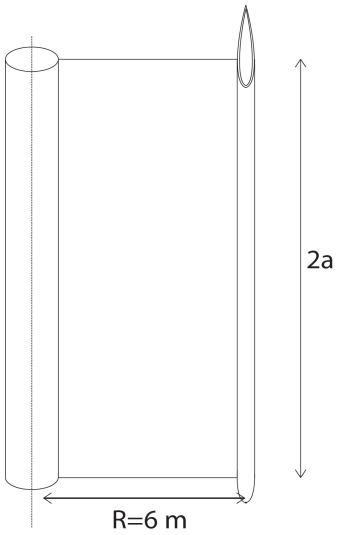


Figure 2.7: Giromill (Our model).

reference Giromill turbine.

The cross section of a Sandia 17-m blade has a joint construction of extruded aluminium, Nomex core, and fiberglass skin (See Fig. 2.8). The blade is a NACA 0012 airfoil an its cross-sectional surface is described by the function

$$\begin{aligned} \hat{y}(\hat{x}) &= \pm 0.53\frac{0.12}{0.2}(0.2969\sqrt{\frac{\hat{x}}{0.53}} - 0.1260\left(\frac{\hat{x}}{0.53}\right) - \\ &\quad 0.3516\left(\frac{\hat{x}}{0.53}\right)^2 + 0.2843\left(\frac{\hat{x}}{0.53}\right)^3 - 0.1015\left(\frac{\hat{x}}{0.53}\right)^4), \end{aligned} \tag{2.40}$$

where $\hat{x}$ is the horizontal location along the chord line of the airfoil and $\hat{y}$ defines the surface of the airfoil as a function of $\hat{x}$.

We will use information about the straight sections of the Sandia 17-m and approximate the blades to be hollow and constructed only of extruded aluminum. Straight sections of Sandia 17-m weigh 10.137 lb/ft and thus has a mass per unit length of $m = 15.09$ kg/m [117]. In order to have the same mass/length ratio, based on Eqn. (2.40) the wall thickness of our extruded aluminum airfoil with density of $\rho_{aluminium} = 2700$ kg/m$^3$ should be 0.2 inches or rounded to 0.005 meters [55] (see Fig. 2.9).

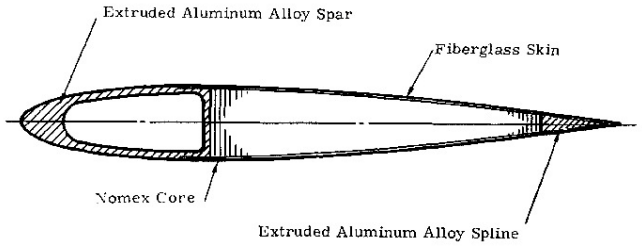


Figure 2.8: SANDIA 17m blade cross section showing aluminum spar and apine, nomax core and fiberglass skin [115].


Figure 2.9: Blade dimensions for calculations.

Table 2.1: Selected aluminum alloy's material properties [17].

| Property | Value |
|---|---|
| Density | 2700 kg/m$^3$ |
| Young's Modulus | 70 GPa |
| Shear Modulus | 26 Gpa |

Using the NACA0012 with extruded aluminum of thickness 0.005 m and chord length of 0.53 m, we can calculate the mass moment of inertia per unit length around centroid of blade cross section as $I_{xx} = 0.37$ kg.m, and second moment of area around chord line as $I_{\hat{z}} = 3.1034 \times 10^{-6}$ m$^4$. A summary of blade parameters is given in Tabs. 2.1 and 2.2.

### 2.4.2 Modal Frequency

In this section, the effects of varying blade length and rotation rate on the natural frequencies of the blade are investigated. For this purpose, the blade is examined when rotating under no aeroelastic forces, such that $Q_q$ and $Q_b$ are equal to zero. Assuming zero torsional stiffness on struts, i.e. the strut connections are ideal pin connections, and also neglecting the effect of gravity, Eqns. (2.35) and (2.36) will be

Table 2.2: Specifications of the model created.

| Blade | NACA0012 |
|---|---|
| Material and Construction | Extruded Aluminum Shell |
| Radius | 6 m |
| Cross sectional weight | 15.09 kg/m |
| Second moment of area around chord line | $3.1034 \text{x} 10^{-6}$ $m^4$ |
| Second moment of area around centroid | 0.000137 $m^4$ |
| Tip Speed Ratio | 5 |

$$\ddot{q} \int_{-a}^{a} m\xi^2 dx - q \int_{-a}^{a} m\Omega^2 \xi^2 dx - \int_{-a}^{a} m\Omega^2 \xi R dx + q \int_{-a}^{a} EI_z \xi''^2 dx = 0, \quad (2.41)$$

$$\ddot{b} \int_{-a}^{a} I_{xx} \rho^2 dx - b \int_{-a}^{a} J_{xx} G \rho'^2 dx = 0 \quad (2.42)$$

where $\xi(x)$ and $\rho(x)$ are approximated by $\cos \pi x/2a$ for the first mode shapes.

#### 2.4.2.1 Reference Case

The approximate modal frequencies for bend and twist for a stationary blade (rotor speed $\Omega = 0$) are shown in Fig. 2.10 as functions of half length $a$. Note that the torsional frequency is much higher than the transverse bending frequency. This is consistent with individual models of bending and torsion of slender members[68]. Since the frequencies are greatly separated, we focus on bending only, where Eqn. (2.41) simplifies to

$$ma\ddot{q} - ma\Omega^2 q + EIa(\frac{\pi}{2a})^4 q = mR\Omega^2(\frac{4a}{\pi}) \quad . \quad (2.43)$$

The modal frequency $\omega_{nq} = \sqrt{\frac{EI}{m}(\frac{\pi}{2a})^4 - \Omega^2} = \sqrt{\omega_0^2 - \Omega^2}$ has the equation of a circle (Fig. 2.11). In the steady-state case, the equilibrium solution for the modal coordinate, $q_{eq}$, is defined as

$$q_{eq} = \frac{mR\Omega^2(\frac{4a}{\pi})}{EIa(\frac{\pi}{2a})^4 - ma\Omega^2} \quad . \quad (2.44)$$

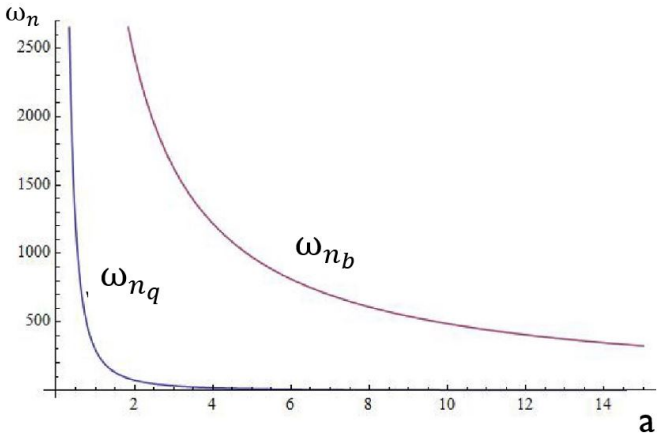


Figure 2.10: Variation $w_{nq}$ and $w_{n_b}$ with length "a" when $\Omega = 0$.

By changing $\Omega$, the magnitude of $q_{eq}$ varies. As shown in Fig. 2.12, there exists a critical value of $\Omega$ for which the undamped natural frequency of the system is zero. When $\Omega$ is close to the critical value, $\Omega_c$, the magnitude of $q_{eq}$ takes a very large value, and the system becomes unstable at $\Omega = \Omega_c$. Figure 2.11 indicates that as $\Omega$ increases, the undamped natural frequency decreases. $\omega_0$ is the natural frequency associated with $\Omega = 0$. The critical rotor speed $\Omega = \Omega_c$, $\omega_{nq} = 0$. For other values of $a$, $\omega_{nq} = 0$ and $\Omega = 0$, respectively, correspond to the critical values of the rotor speed and the natural frequency of the system. Based on Fig. 2.11 the critical speed for the case when $a = 8.5$ is close to 4.2 rad/s. This is very close to the operating speed of the Sandia 17-m turbine. The rotor may undergo a severe condition if it operates with a speed close to the critical rotor speed. Therefore, the operating speed of the rotor, $\Omega_{operate}$, should not be close to the critical rotational speed of rotor. To this end, the goal is to increase the natural frequency of the system such that $\Omega_{operate} << \omega_n$. As shown in the Fig. 2.11, increasing the natural frequency brings an increase in the critical rotor speed and provides a wide safe range of speed of rotation.

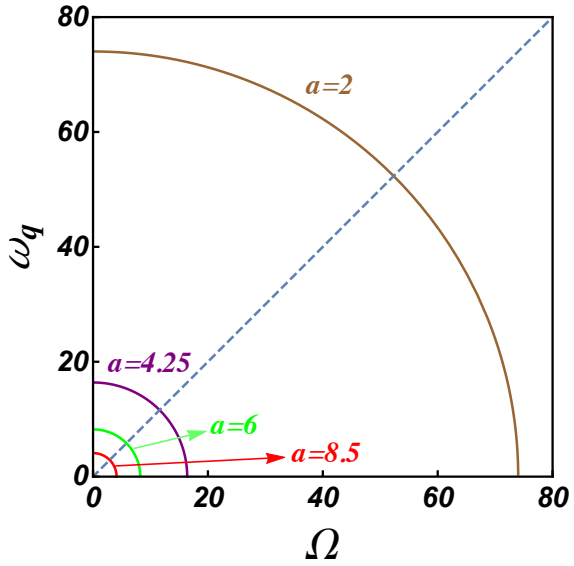


Figure 2.11: Natural frequency with Ω for different length of the blade.

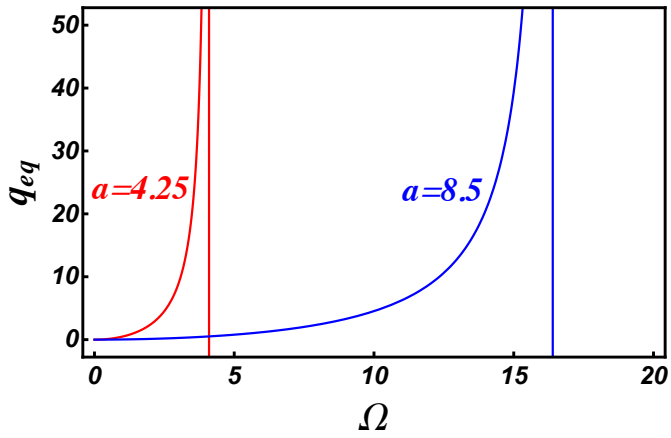


Figure 2.12: $q_{eq}$ with Ω for $a = 8.5$ and $a = 4.25$.

#### 2.4.2.2 Effect of Blade Length

In order to increase the natural frequency of the system, we stiffen our Giromill by adding a strut at the middle of the blade, with a pin joint. This shorten the length of the blade from $2a$ to $a$ and divide the blade into two similar parts. For the case that the length of the blade is $a$, variation of the natural frequency and $q_{eq}$ with Ω are shown in Figs. 2.11 and 2.12.

Fig. 2.11 illustrates how the natural frequency of the system varies with the rotor speed

for different values of $a$. For example, when $a = 2$ m, the natural frequency of the non rotating system, $\omega_0$, as well as the critical rotational speed of the rotor, $\Omega_c$, increase to a value near 16 rad/s. It denotes that for $\Omega < 10$ the magnitude of $q_{eq}$ does not diverge and system stays stable in this range.

For a single degree of freedom reduced order model of a straight blade, the spin induces centrifugal softening and elastic stiffening. Centrifugal softening is a result of the linear behavior where $q_{eq} \sim \Omega^2$ and the elastic stiffening comes from the nonlinearity in the system, where $q_{eq}^2 \sim \Omega^4$ and also the nonlinear centrifugal softening.

To explain this, consider replacing the straight vertical blade with a mass on a tight vertical string (and omit the effect of gravity) at a radius $R$ from the center of rotation, as a single-mode approximation. For small deflections $x$ from the undeformed position, the tension increases with the square of the deflection, such that the stiffness is $k(x) \approx k_0 + \beta x^2$, with $\beta$ accommodating the leading nonlinear stiffening effect. The equation of motion is $m\ddot{x} + (k_0 + \beta x^2 - m\Omega^2)x = mR\Omega^2$. To leading order, the equilibrium scales with $\Omega^2$ as in Eqn. (2.44), such that $x_{eq} \approx \alpha\Omega^2$. Letting $y = x - x_{eq}$ and linearizing leads to the equation $m\ddot{y} + (k_0 - m\Omega^2 + 3\beta\alpha^2\Omega^4)y \approx 0$. Thus the system is softening with $\Omega^2$, which is a linear effect leading to behavior similar to Eqn. (2.43) and stiffening with $\beta\Omega^4$, which is a nonlinear effect associated larger deflections.

#### 2.4.2.3 Time Varying Parameters and Response

The equation of motion for the only transverse bending, with an aerodynamic force, is

$$\ddot{q} + c(t)\dot{q} + k(t)q = f(t), \tag{2.45}$$

where, $f(t) = a_0 + f_0(t)$, $k(t) = \omega_q^2 + a_1(t)$ and $c(t) = c_0 + a_2(t)$. The time varying coefficients include an average value and a fluctuating part. Figures 2.13 ,2.14, 2.15 show the relative contribution of the constant and cyclic root mean squared (RMS) components of the direct excitation term, $f(t)$, and the damping and stiffness terms for $a = 8.5$m. Figures

interpret the importance of the parametric effects through each terms of the equation. Figures 2.16, 2.17 and 2.18 demonstrate the time traces of constant-plus-periodic direct excitation, damping coefficient and the stiffness, for the specific rotor speed of $\Omega$ = 3.875 rad/s and illustrate the periodic behavior of each of the components in modal coordinate system.

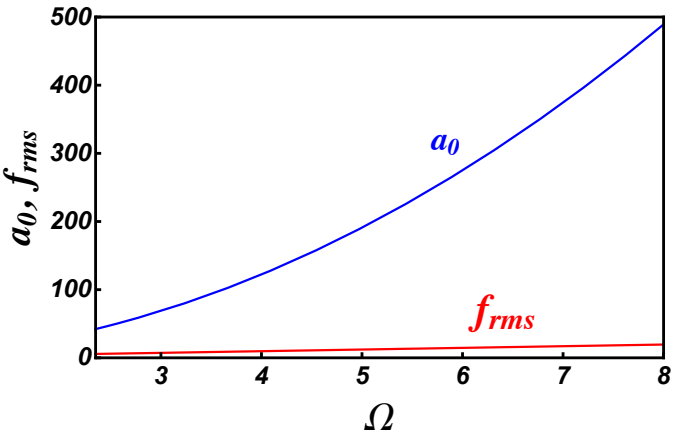


Figure 2.13: Variation of two parts forcing function with Ω.

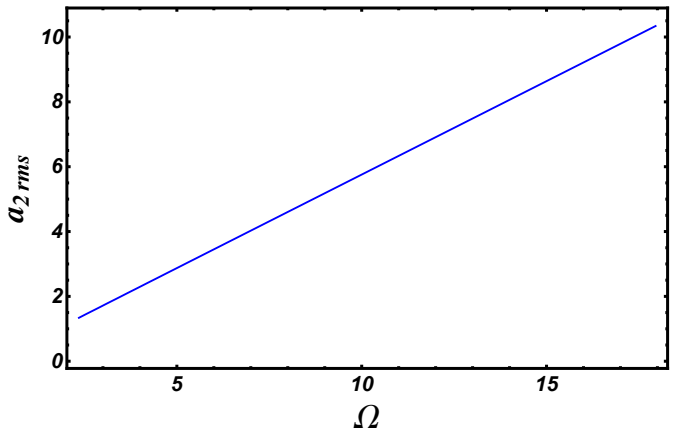


Figure 2.14: Variation of damping coefficient Ω.

The $Q_q$ term is substituted into the right hand side of the Eqn. (2.41) and the general form of the equation due to bending takes the form

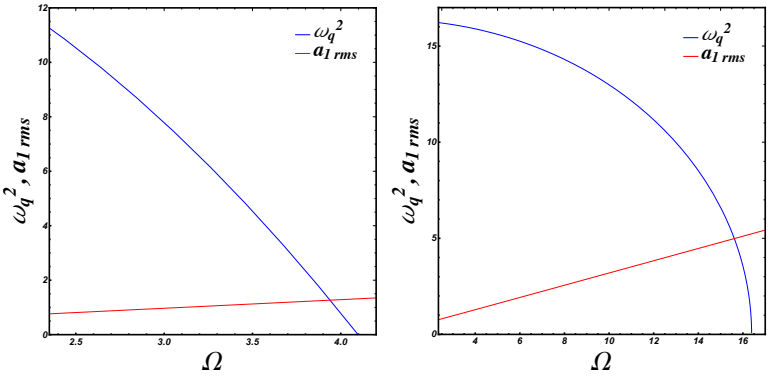


(a) $a = 8.5$ m (b) $a = 4.25$ m

Figure 2.15: Stiffness components vs Ω.

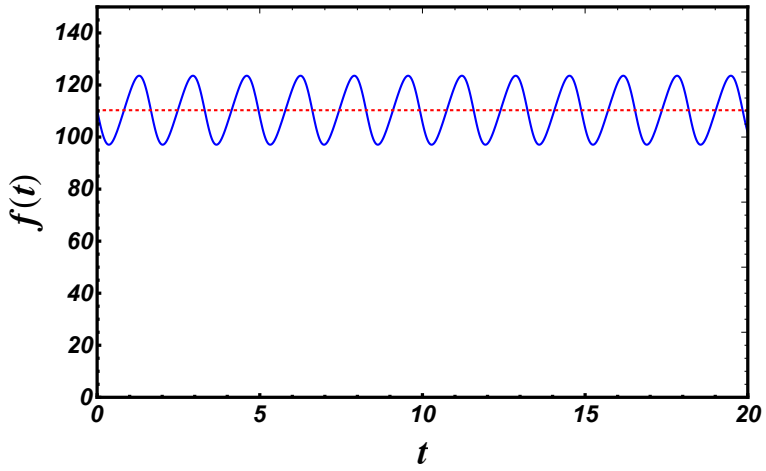


Figure 2.16: Periodic behavior $f(t)$ for $u = 4.7m/s$ and $\Omega = 3.8rad/sec$.

$$\ddot{q}\int_{-a}^{a} m\xi^2 dx - q\int_{-a}^{a} m\Omega^2\xi^2 dx - \int_{-a}^{a} m\Omega^2\xi R dx \qquad (2.46)$$
$$+ \quad q\int_{-a}^{a} EI_z\xi''^2 dx = \int_{-a}^{a} m\Omega^2\xi R dx - \int_{-a}^{a} \hat{f}_{q_{000}}\xi(x) dx$$

The time history of $q(t)$ for two values of $a$, $a = 8.5$ m and $a = 4.25$ m, $\Omega = 3.875$ rad/s, $u = 4.7$ m/s are shown in Fig. 2.19. Equation. (2.46) includes constant plus cyclic direct forcing, as well as parametric excitation, the degree to which depends on the parameters. The response has the form $q_t(t) = q_h(t)+q_p(t)$, the sum of the homogeneous and particular

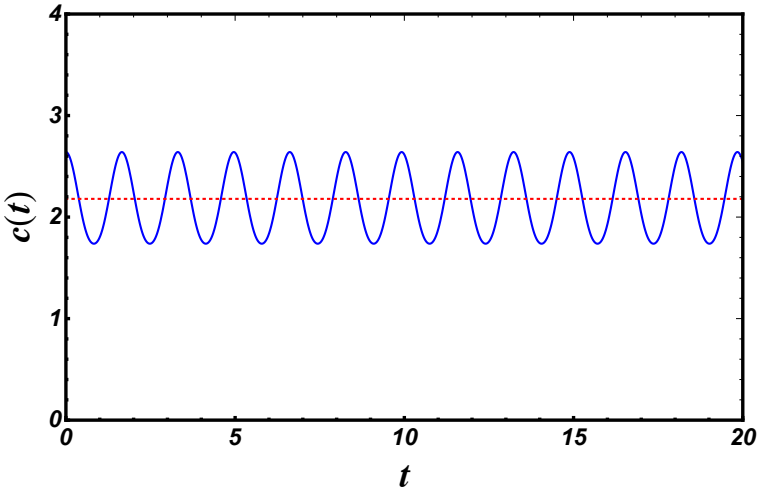


Figure 2.17: Periodic behavior of $c(t)$ for $u = 4.7m/s$ and $\Omega = 3.8rad/sec$.

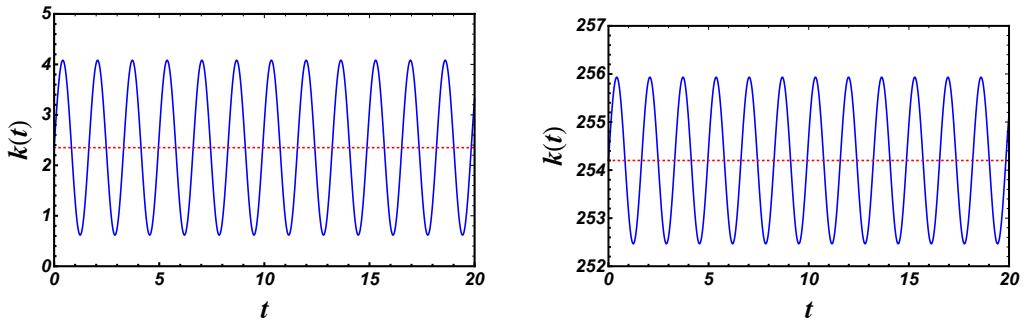


(a) $a = 8.5$ m (b) $a = 4.25$ m

Figure 2.18: Periodic stiffness when $u = 4.7m/s$, $\Omega = 3.8rad/s$.

solutions. The particular solution $q_p(t) = q_{eq} + \tilde{q}(t)$ includes the equilibrium solution and a cyclic components of direct excitation. Figures 2.20a and 2.20b show the RMS values of the cyclic solution terms, $\tilde{q}$, as a function of rotor speed, for the case of $a = 8.5$ m and $a = 4.25$ m, respectively, and $u = 4.7$ m/s. As it is shown, there is a resonance in both cases, which may happen when $\omega_{nq} = \Omega$ which indicates a primary resonance (Fig. 2.11). Beyond resonance, the response continue to grow with increasing rotor speed because of the growing strength of the excitation itself.

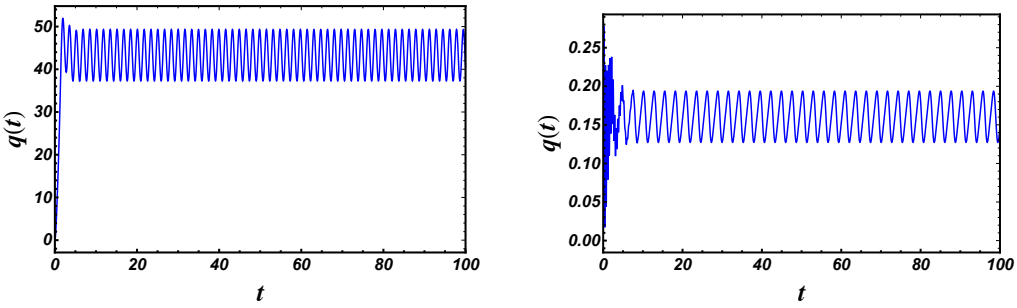


(a) $a$ = 8.5 m (b) $a$ = 4.25 m

Figure 2.19: Periodic response in modal coordinate $q(t)$ when $u = 4.7m/s$, $\Omega = 3.8rad/s$.

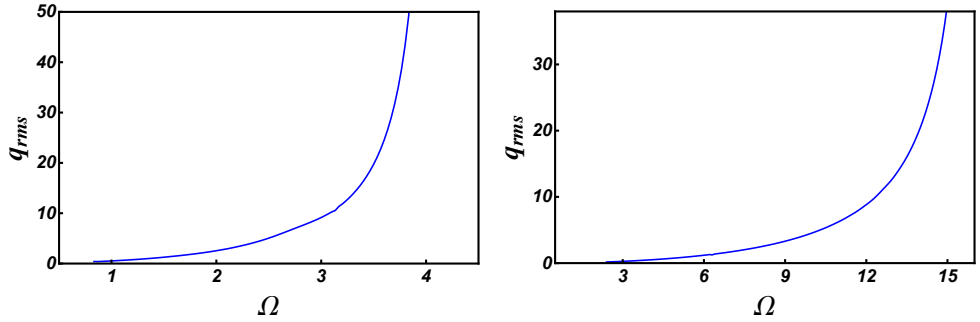


(a) $a$ = 8.5 m (b) $a$ = 4.25 m

Figure 2.20: Frequency response amplitude when $u = 4.7m/s$, $\Omega = 3.8rad/s$.

## 2.5 Conclusion

A blade vibration model for an H-rotor/Giromill type VAWT with bend and twist deflections was formulated. Energy method was used to obtain the energy equations for an Eulerian beam under transverse bend and twist deflections was obtained. The system was discretized using reduced order modeling on first assumed modes. Lagrange'ss equation was applied to the assumed modal coordinates, to obtain two equations of motion where generalized force terms were due aeroelastic forces on blades. Next, an aeroelastic model was derived based on quasi steady airfoil theory. Lift and drag forces and moments were formulated for an airfoil with varying angle of attack, where stall effects were neglected. The formulas were simplified to cubic order using Taylor series expansion. The resulting system had parametric and direct excitation due to varying flow magnitude and direction

relative to blade.

In order to conduct a simple numerical analysis, the system was linearized assuming small deflections for bend and twist. Linearized equations of motion were derived for a specific blade. Referring to Sandia 17m VAWT, a hypothetical Giromill blade was defined for numerical analysis where natural frequencies of the blade for a non rotating system were found.

The initial simulations showed that the Giromill undergoes large static deflections if the blade length $2a$ is too large (in the range of the egg-beater style Sandia 17-m reference turbine) when operating at nominal speeds for the Sandia 17-m system. As such we conducted a study of direct and parametric loads and static deflection components for a variety of blade lengths. Sample cyclic responses were also included. Indeed, the natural frequency is dependent on the rotor speed. Given the parameters, in the linearized model, there is a critical rotor speed at which the natural frequency is reduced to zero, accompanied by instability and unbounded static deflection. While this is a linearized behavior, it clearly shows a range of unacceptable parameters, and designs should be made such that structural behavior is sound when operating at typical rotor speeds. The Giromill turbine must have a blade length, or a stiffening system, to keep the natural frequency sufficiently high during rotation. Given a sufficiently stiff design, the next phase of study will be to look in more detail at the vibration responses, and understand the circumstances for which parametric excitation may be significant.

# CHAPTER 3

## A FLOQUET-BASED ANALYSIS OF PARAMETRIC EXCITATION THROUGH THE DAMPING COEFFICIENT

Parametric excitation occurs when a system has time varying coefficients that drive the oscillation. Dynamical systems that are exposed to parametric excitation experience notable behavior[26, 43, 62, 122]. Parametric excitation happens in various types of systems. E.g. in electrical systems, an LC circuit with periodic time varying capacitance represents Hill's equation [53]. In ecological systems, the population dynamics in periodic environments causes periodic variability in systems [52]. In mechanical systems, a pendulum with periodic vertical base excitation [58, 96], gear whine with cyclic contact points [81], and horizontal-axis wind-turbine blades with cyclic gravitational forces [3], all have parametric stiffness.

Our previous study on vertical-axis wind-turbine blades (VAWTs) suggested the existence of periodic damping in the equations of motion due to the aeroelastic forces involving a cyclic angle of attack [5]. A simplified mechanism for this can be seen in the context of an airfoil of chord length $c$. The lift force per unit length, $F$, is proportional to the speed $v$ squared through a coefficient which is assumed to be linear in the angle of attack $\alpha$, such that $F = \frac{1}{2}C_d(\alpha)\rho c v^2 = c_d \alpha v^2$. In a VAWT under ideal steady wind conditions with wind speed $u$, the angle of attack varies with the cyclic angle $\alpha_0(t) \cong a_0 + a_1 \cos\omega t$ of ambient wind, and also with the velocity $\dot{x}$ of the blade deflection (Fig. 3.1). If $\alpha \cong \alpha_0(t) - \dot{x}/u$ and $v \cong u - b\dot{x}$, then the force takes the form $F \cong c_d a_0 u^2 + c_d u^2 a_1 \cos\omega t - c_0 \dot{x} - c_1 \cos\omega t \dot{x}$.

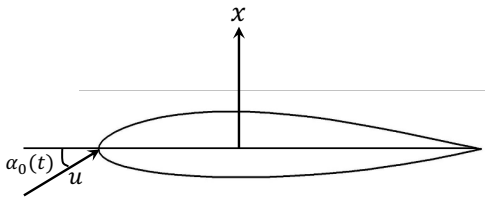


Figure 3.1: The angle of attack of the relative velocity of wind $u$ on an airfoil depends on the cyclic angle of the wind and on the coordinate velocity $\dot{x}$.

The first terms are direct excitation and the latter terms involve cyclic damping. (In an ideal VAWT, the magnitude of relative flow velocity also varies with the VAWT rotation. Other aeroelastic effects might also affect the mean damping.)

Systems with parametric excitation have been studied broadly with various methods. Cantero et. al [20] looked into the parametric excitation of mooring lines. They used the method of harmonic balance to obtain an analytical expression of the unstable layout. Lilien and Pinto da Costa [59] studied the vibration amplitudes caused by parametric excitation of nonlinear cable-stayed structures. They defined the non-dimensional parameters for the cable-stayed bridge and then used the harmonic balance method to find the limit-cycle amplitude. Lenci et. al [57] applied a perturbation method to a parametrically driven pendulum to determine the stability of the harmonic solution. Hsu [44] examined parametric excitation of a dynamic system with multiple degrees of freedom. He combined the method of variation of parameters and the series expansion of the perturbation method to derive the instability criteria for the instability regions.

Besides all the declared methods, Floquet theory applies to the linear differential equations with parametric coefficients and it is a very useful tool for studying the stability of dynamic systems[22, 88]. However, Hsu explains that in Floquet theory, approximation is often required to discover the stability characteristics. Furthermore, most of the approximate methods are only valid when the magnitude of the excitation is small[42, 43].

The Mathieu equation is one of the most well known differential equations with parametric excitation. There have been extensive studies on the damped and undamped Mathieu equation using harmonic balance [88] and perturbation methods [18, 46, 72, 73, 85, 87, 91, 105, 107, 108, 120]. Ward [112] determined the region of stability of the Mathieu equation by assuming the solution to be consist of only a periodic part. Acar and Feeny [3] studied the Floquet-based analysis of the Mathieu equation's responses and assumed a Floquet solution including both exponential and periodic parts. They combined

Floquet theory with the harmonic balance method and investigated the time response and the stability of the equations of motion.

In some parametric systems a phenomenon called *coexistence* happens. Coexistence occurs when the boundaries of an unstable region overlap and the instability wedge disappears. Recktenwald and Rand [89] studied coexistence and obtained the conditions for coexistence to occur in a generalized Ince's equation.

In this work we study the response characteristics of a linear oscillator with parametric damping. We first use Floquet theory to draw conclusions about the effects of cyclic damping on the Floquet multipliers. We then use the original Floquet solution with a non-zero exponential part and a periodic part which is approximated as a truncated Fourier series. As in reference [3], the harmonic balance method is applied to obtain the Floquet exponents and Fourier coefficients. This analysis provides not only the stability information but also the general response of the system in each stability situation. We uncover the coexistence phenomenon and study its characteristics, then observe the effects of a specific perturbation in the damping.

## 3.1 Floquet Theory

In this section we follow a standard development of Floquet theory [88], and make adaptions for our system. Floquet theory is applicable to a linear differential system of the form

$$\dot{\mathbf{x}} = \mathbf{A}(t)\mathbf{x}, \tag{3.1}$$

where $\mathbf{A}(t) = \mathbf{A}(t+T)$ is an $n \times n$ periodic matrix of period $T$ and $\mathbf{x} \in R^n$ is an $n \times 1$ column vector [88]. Suppose

$$\begin{aligned}
&\mathbf{x}^{(1)}(t): \quad \text{is the solution vector with I.C.s} \quad \mathbf{x}_0^{(1)} = [1\ 0 \ldots 0]^T, \\
&\quad \vdots \\
&\mathbf{x}^{(n)}(t): \quad \text{is the solution vector with I.C.s} \quad \mathbf{x}_0^{(n)} = [0\ 0 \ldots 1]^T
\end{aligned}$$

(I.C. refers to initial condition). For a general initial condition, $\mathbf{x}_0 = [c_1 \ c_2 \dots c_n]^T$, the solution becomes

$$\mathbf{x}(t) = \left[\mathbf{x}^{(1)}(t) \ \ \mathbf{x}^{(2)}(t) \ \ \dots \ \ \mathbf{x}^{(n)}(t)\right] \begin{pmatrix} c_1 \\ c_2 \\ \vdots \\ c_n \end{pmatrix} = \mathbf{X}(t)\mathbf{x}_0. \tag{3.2}$$

$\mathbf{X}(t)$ is called the fundamental solution matrix (FSM). The FSM is the solution vectors of Eqn. (3.1) when initial conditions are unity, such that $\mathbf{X}(0) = \mathbf{I}$. Any other solution matrix $\mathbf{Z}(t)$ may be written in the form

$$\mathbf{Z}(t) = \mathbf{X}(t)\mathbf{C}, \tag{3.3}$$

where $\mathbf{C}$ is a nonsingular $n \times n$ matrix. In that case, each of the columns of $\mathbf{Z}(t)$ may be written as a linear combination of the columns of $\mathbf{X}(t)$. Note that $\mathbf{Z}(0) = \mathbf{X}(0)\mathbf{C} = \mathbf{I}\mathbf{C} = \mathbf{C}$. Let $\mathbf{Z}(t) = \mathbf{X}(t+T)$. Then $\mathbf{Z}(0) = \mathbf{C} = \mathbf{X}(T) \neq \mathbf{I}$, and from Eqn. (3.3) we have

$$\mathbf{X}(t+T) = \mathbf{X}(t)\mathbf{C}. \tag{3.4}$$

This implies that $\mathbf{X}(t)$ and $\mathbf{X}(t+T)$ are related by the constant matrix $\mathbf{C} = \mathbf{X}(T)$. By successively iterating we get

$$\mathbf{X}(t+mT) = \mathbf{X}(t)\mathbf{C}^m. \tag{3.5}$$

Equation (3.4) is a difference equation. If $\lambda_i$, the eigenvalues of $\mathbf{C}$, are distinct, then Eqn. (3.4) can be diagonalized via the transformation $\mathbf{X} = \mathbf{Y}P^{-1}$, where the columns of matrix $\mathbf{P}$ are eigenvectors of $\mathbf{C}$, and $\mathbf{J} = \mathbf{P}^{-1}\mathbf{C}P$ is a diagonal matrix of eigenvalues. The diagonalized difference equation becomes

$$y_i(t+T) = \lambda_i y_i(t), \qquad i = 1, ..., n. \tag{3.6}$$

In this setting, $y_i$ are diagonal elements of $\mathbf{Y}$.

**Analysis Based on Floquet Theory** A second-order linear differential equation with time varying coefficients can be expressed in a general form as

$$\ddot{x} + g(t)\dot{x} + h(t)x = f(t), \tag{3.7}$$

where $g(t)$ and $h(t)$ are periodic functions. If $g(t) = 0$ and $f(t) = 0$, the equation reduces to the Hill's equation [61], $\ddot{x} + h(t)x = 0$. If $h(t) = \delta + \epsilon \cos \omega t$, where $\omega$ is the frequency ratio (dimensionless frequency), and $\delta$ and $\epsilon$ are constants, Hill's equation takes the form of Mathieu's equation as

$$\ddot{x} + (\delta + \epsilon \cos \omega t)x = 0. \tag{3.8}$$

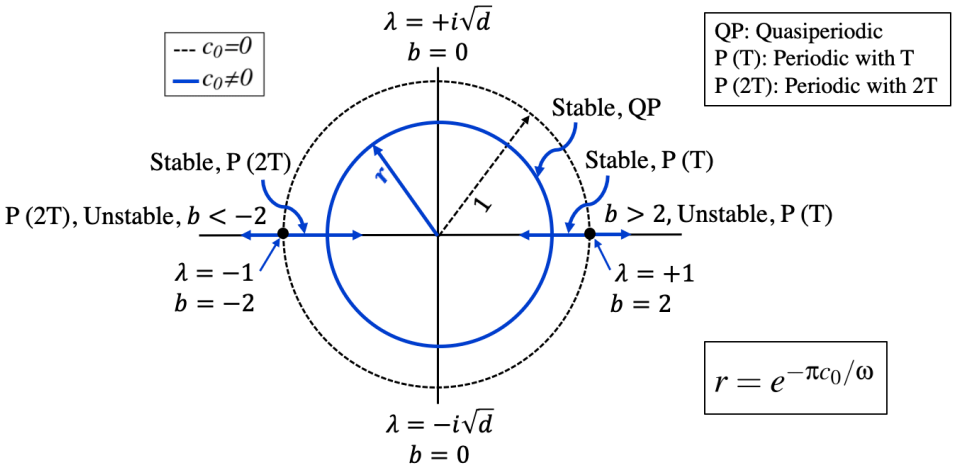


Figure 3.2: Locus of Floquet exponents for an equation with both parametric damping and stiffness coefficients when $c_0 \geq 0$.

Here, we study the application of Floquet theory to the generalized homogeneous differential equation with parametric damping and stiffness, i.e. Eqn. (3.7) when $f(t) = 0$. In the state-space form, the equation with cyclic damping and cyclic stiffness appears as

$$\dot{\mathbf{x}} = \begin{pmatrix} \dot{x} \\ \ddot{x} \end{pmatrix} = \begin{bmatrix} 0 & 1 \\ -h(t) & -g(t) \end{bmatrix} \begin{pmatrix} x \\ \dot{x} \end{pmatrix} = \mathbf{A}(t)\mathbf{x}, \tag{3.9}$$

where $\mathbf{A}(t)$ is a periodic matrix with period $T = \frac{2\pi}{\omega}$. The fundamental matrix solution in Eqn. (3.2) takes the form

$$\mathbf{X}(t) = \begin{bmatrix} x_1^{(1)}(t) & x_1^{(2)}(t) \\ \\ x_2{}^{(1)}(t) & x_2{}^{(2)}(t) \end{bmatrix}, \tag{3.10}$$

where $x_1 = x$ and $x_2 = \dot{x}$. $W(t) = \det \mathbf{X}(t) = x_1^{(1)}(t)x_2^{(2)}(t) - x_1^{(2)}(t)x_2^{(1)}(t)$ is defined as the Wronskian. Taking the time derivative of $W$ and using Eqn. (5.7), $\dot{W}(t)$ in terms of $x_1(t)$ and $x_2(t)$ is, (for simplicity we drop (t))

(3.11)

$$\begin{aligned} \dot{W} &= \dot{x}_1^{(1)}x_2^{(2)} + x_1^{(1)}\dot{x}_2^{(2)} - \dot{x}_1^{(2)}x_2^{(1)} - x_1^{(2)}\dot{x}_2^{(1)} \\ &= -x_2^{(1)}x_2^{(2)} + x_1^{(1)}(-hx_1^{(2)} - gx_2^{(2)}) \\ &\quad + x_2^{(2)}x_2^{(1)} - x_1^{(2)}(-hx_1^{(1)} - gx_2^{(1)}) \\ &= -h(x_1^{(1)}x_1^{(2)} - x_1^{(2)}x_1^{(1)}) - g(x_1^{(1)}x_2^{(2)} - x_1^{(2)}x_2^{(1)}). \end{aligned}$$

Unlike with Hill's equation [88, 112], the above equation reduces to

$$\dot{W}(t) = -g(t)W(t). \tag{3.12}$$

By decomposing $g(t)$ into a mean and a time-varying part as $g(t) = c_0 + \tilde{g}(t)$ and then solving Eqn. (3.12), we obtain $W(t) = e^{-c_0 t - G(t) + k}$, where $G(t) = \int \tilde{g}(t)dt$ and $k$ is an integration constant. At $t = 0$, $W(0) = e^{-G(0)+k} = \det \mathbf{X}(0) = \det \mathbf{I} = 1$. Therefore, $k = G(0)$. By periodicity $G(T) = G(0)$ and therefore

$$W(T) = e^{-2\pi c_0/\omega}. \tag{3.13}$$

We have observed that $\mathbf{X}(T) = \mathbf{X}(0)\mathbf{C} = \mathbf{C}$. $\lambda_i$, the eigenvalues of $\mathbf{C}$, are the Floquet multipliers and they satisfy $|\mathbf{C} - \lambda\mathbf{I}| = 0$, i.e. the characteristic equation

$$\lambda^2 - b\lambda + d = 0, \tag{3.14}$$

where $b = \text{trace}(\mathbf{C})$ and $d = \det(\mathbf{C}) = W(T)$. Different values of $b$ and $d$ lead to real and complex eigenvalues. For the case that $\lambda$ is real

$$\lambda = \frac{b \pm \sqrt{b^2 - 4d}}{2}, \tag{3.15}$$

and for the case that $\lambda$ is complex,

$$\begin{aligned} \lambda &= \frac{b \pm i\sqrt{4d - b^2}}{2}, \\ |\lambda| &= \frac{1}{2}(b^2 + 4d - b^2)^{\frac{1}{2}} = \sqrt{d}. \end{aligned} \tag{3.16}$$

Using Eqn. (3.13),

$$|\lambda| = \sqrt{W(T)} = \sqrt{e^{-2\pi c_0/\omega}} = e^{-\pi c_0/\omega}. \tag{3.17}$$

Thus for complex $\lambda$, Eqn. (3.16) describes a circle of radius $r = |\lambda| = e^{-\pi c_0/\omega}$ (Fig. 3.2). This holds for any system of the form of Eqn. (3.7), including the damped Mathieu equation, where the mean damping is $c_0$. If $c_0 \geq 0$ the system stability depends on $\lambda$ as follows

- $|\lambda_i| \leq 1$ stable
- $|\lambda_1| \leq 1, \lambda_2 = \pm 1$ stability transition
- $|\lambda_1| < 1, |\lambda_2| > 1$ unstable

When $\lambda = 1$, the system has an underlying periodicity of period $T$, since

$$y^{(i)}(t + T) = \lambda_i y^{(i)}(t) = y^{(i)}(t), \tag{3.18}$$

for one of the $y^{(i)}$. In such case Eqn. (3.14) implies $b = 1 + d$ and from Eqns. (3.16) and (3.17)

$$b = 1 + e^{-2\pi c_0/\omega}. \tag{3.19}$$

When $\lambda = -1$, the underlying periodic solution is associated with period $2T$, since one of the $y^{(i)}$ obeys

$$y^{(i)}(t + T) = -y^{(i)}(t). \tag{3.20}$$

Also $b = -(1 + e^{-2\pi c_0/\omega})$. When $b = 0$, $\lambda = \pm id$.

Note that the transition between stable and unstable solutions of the differential equation (Eqn. (3.7)) involves a solution with underlying periodicity $T$ ($\lambda = 1$) or $2T$ ($\lambda = -1$).

Equation (3.6) is a first order linear difference equation and if $\lambda_i$ are distinct, we seek a solution of the form

$$y^{(i)}(t) = y_0^{(i)} \lambda_i^{st}, \tag{3.21}$$

where $s$ is an unknown constant. Substituting Eqn. (3.21) into Eqn. (3.6)

$$y^{(i)}(t+T) = y_0^{(i)} \lambda_i^{s(t+T)} = y_0^{(i)} \lambda_i^{st} \lambda_i^{sT} = \lambda_i y^{(i)}(t). \tag{3.22}$$

Equation (3.22) is satisfied if $s = \frac{1}{T}$ [88]. Then,

$$y^{(i)}(t) = y_0^{(i)} \lambda_i^{\frac{t}{T}} = y_0^{(i)} e^{\mu_i t}, \tag{3.23}$$

where $\mu_i = \frac{\ln \lambda_i}{T}$. The $\lambda_i$ were defined earlier as the Floquet multipliers, and $\mu_i$ are the associated Floquet exponents. When all $|\lambda_i| \leq 1$, then all $Re(\mu_i) \leq 0$, and as discussed above, the system is stable. $W(T) = \det \mathbf{C}$ indicates the growth of the state-space volume associated with iterations of the Poincare map [13]. When $c_0 = 0$, $W(T) = 1$, and the map is area preserving. When $c_0 > 0$, the map is contracting and dissipative. When $c_0 < 0$ and both multipliers are complex with $|\lambda_i| > 1$, the system is unstable. Furthermore, when $c_0 < 0$, and the multipliers are real, at least one multiplier will be such that $|\lambda_i| > 1$ and the system is unstable. Thus, parametric excitation cannot stabilize a system with negative mean damping.

**Special Case when $c_0 = 0$** When $c_0 = 0$, the circle has radius 1. So when $\lambda = \pm 1$, the eigenvalues are repeated and the Jordan form is not diagonal. However, the conclusions about stability transitions hold. Based on Eqn. (3.13), when $c_0 = 0$, $W(T) = 1$, and accordingly the characteristic equation for the differential equation with parametric damping found by Floquet theory is $\lambda^2 - \text{trace}(\mathbf{C})\lambda + 1 = 0$. In such circumstances, the

Floquet circle of periodic damping appears to have the same form as that of Hill's equation when stiffness is periodic, namely:

$$\lambda = \frac{a \pm \sqrt{a^2 - 4}}{2}, \qquad a = \text{trace}(\mathbf{C}), \tag{3.24}$$

although $a = \text{trace}(\mathbf{C})$ is not the same as in Hill's equation.

## 3.2 Oscillator with Parametric Damping

The concern of this study is to inquire into a linear differential equation for which, unlike Mathieu's equation, stiffness is constant but damping is parametric, such that

$$x'' + (d_0 + d_1 \cos \hat{\omega}\tau)x' + \omega_n^2 x = 0, \tag{3.25}$$

where $d_0$ and $d_1$ are constants and $()' = \frac{d()}{d\tau}$. By performing a change of variables, $t = \omega_n \tau$, the alternative equation is

$$\ddot{x} + (c_0 + c_1 \cos \omega t)\dot{x} + x = 0, \tag{3.26}$$

where $\omega = \frac{\hat{\omega}}{\omega_n}$ is a dimensionless frequency ratio, $\dot{()} = \frac{d()}{dt}$, and $c_0$ and $c_1$ are constants. Defining a state vector $\mathbf{x} = [x \;\; \dot{x}]^T$, Eqn. (3.26) can be expressed in state-space form as $\dot{\mathbf{x}} = \mathbf{A}(t)\mathbf{x}$. Therefore, the Floquet theory can be applied to the intended differential equation [73, 88].

Hartono and Burgh [38] studied the equation with a time varying damping coefficient with zero mean damping and investigated the stability. They transformed variables and reduced the equation to a standard Hill's equation $\ddot{y} + [\Lambda + Q(t)]y = 0$, where $Q(t)$ is a periodic function with period $\pi$. They approximated $\Lambda$s for which the stability transitions occur. Later, we will discuss Hartono and Burgh's results and compare with our observed results.

### 3.2.1 Approximate Solution

Floquet theory is combined with harmonic balance to find an approximate solution to Eqn. (3.26). Following the Floquet theory the solution consists of an exponential term and

periodic term, $x(t) = e^{\mu t}p(t)$, where $p(t)$ is periodic with period $T$. A truncated series solution is assumed such that

$$x(t) = e^{\mu t}\sum_{j=-n}^{+n} a_j e^{ij\omega t}, \tag{3.27}$$

in which $\mu$ is the Floquet exponent and $a_j$s are Fourier coefficients. The assumed solution is plugged into Eqn. (3.26) and harmonic balance is applied to find the coefficients of $e^{ij\omega t}$. The harmonic balance leads to an equation of the form $\mathbf{D}(\mu)\mathbf{a} = 0$, where $\mathbf{D}(\mu)$ is a $(2n+1)\times(2n+1)$ coefficient matrix and $\mathbf{a}$ is a $(2n+1)\times(1)$ vector of the Fourier coefficients ($a_j$'s) for the assumed solution. In order to have nontrivial and nonzero $a_j$'s, the determinant of the coefficient matrix, $\mathbf{D}(\mu)$, is required to be zero. Setting the determinant to zero gives the characteristic equation with unknown $\mu$.

The characteristic equation of $|\mathbf{D}(\mu)| = 0$ is a $(4n+2)$ degree polynomial in terms of $\mu$ which yields $(4n+2)$ roots for $\mu$. From Floquet theory the number of $\mu$'s should be equal to the dimension of the state space, $N = 2$, so it turns out that some of the $\mu$'s of the characteristic equation are spurious. Thus $N = 2$ of the roots are independent, and are called *the principle roots*. According to the Floquet theory [112] the characteristic multipliers satisfy

$$\lambda_1\lambda_2...\lambda_N = exp(\int_0^T Tr(\mathbf{A}(s))ds), \tag{3.28}$$

where $\lambda_k = e^{\mu_k T}$. For this problem two distinct Floquet exponents ($\mu$'s) satisfy Eqn. (3.28) such that

$$e^{(\mu_1+\mu_2)T} = exp(\int_0^T Tr(\mathbf{A}(s))ds). \tag{3.29}$$

In Eqn. (5.7), $Tr(\mathbf{A}) = -g(t) = -(c_0 + c_1\cos\omega t)$ and so $\int_0^T Tr(\mathbf{A}(s))ds = -c_0T$. Therefore, we can write $e^{(\mu_1+\mu_2)T} = e^{(-c_0T\pm 2\pi ik)}$, since any multiple of $2\pi i$ can be added to an exponential argument. Using $T = \frac{2\pi}{\omega}$, this implies

$$\mu_1 + \mu_2 = -c_0 \pm k\omega i. \tag{3.30}$$

Equation (3.30) specifies the relationship between the two principle Floquet exponents, $\mu_1$ and $\mu_2$, with the mean damping term $c_0$, the time period, $T = \frac{2\pi}{\omega}$, and an integer $k$. The solution to $|\mathbf{D}(\mu)| = 0$ results in $4n + 2$ roots for $\mu$ and the two individual principal roots for any pair of $c_0$ and $\omega$ are selected to satisfy Eqn. (3.30).

In the assumed solution (Eqn. (3.27)), the imaginary part of the Floquet exponent, $Im(\mu)$, combines with the frequencies of the harmonics of the periodic term to define the frequencies of the response. The general response is a linear combination of principal responses such that

$$x(t) = A_1 e^{\mu_1 t} \sum_{j=-n}^{+n} a_j e^{ij\omega t} + A_2 e^{\mu_2 t} \sum_{j=-n}^{+n} a_j e^{ij\omega t}, \tag{3.31}$$

where $A_1$ and $A_2$ are determined by initial conditions. In the next section, the truncated solution of Eqn. (3.26) is explained.

### 3.2.2 Truncated Series Solution

The truncated series solution of the parametric excited motion can be used to quantify the stability domain and approximate the response to the initial conditions and response frequencies. We consider the truncated solution in Eqn. (3.27) for $n = 2$ as

$$x(t) = e^{\mu t} \sum_{j=-2}^{+2} a_j e^{ij\omega t}. \tag{3.32}$$

Previously, Acar and Feeny [3] showed that for $n = 2$, the truncated solution of the Mathieu equation converges well except when $\omega$ was small.

Substituting the approximate truncated solution into the governing equation (Eqn. (3.26)) and balancing coefficients of $e^{ij\omega t}$ lead to the following equation:

$$\begin{bmatrix} B_{-2} & \frac{c_1}{2} & 0 & 0 & 0 \\ \frac{c_1}{2} & B_{-1} & \frac{c_1}{2} & 0 & 0 \\ 0 & \frac{c_1}{2} & B_0 & \frac{c_1}{2} & 0 \\ 0 & 0 & \frac{c_1}{2} & B_1 & \frac{c_1}{2} \\ 0 & 0 & 0 & \frac{c_1}{2} & B_2 \end{bmatrix} \begin{pmatrix} a_{-2} \\ a_{-1} \\ a_0 \\ a_1 \\ a_2 \end{pmatrix} = \begin{pmatrix} 0 \\ 0 \\ 0 \\ 0 \\ 0 \end{pmatrix}, \tag{3.33}$$

where

$$
\begin{aligned}
B_{-2} &= ic_0\mu - 2ic_0\omega - \mu^2 + 4\mu\omega - 4\omega^2 + 1, \\
B_{-1} &= ic_0\mu - ic_0\omega - \mu^2 + 2\mu\omega - \omega^2 + 1, \\
B_0 &= \frac{1}{2}\left(2ic_0\mu - 2\mu^2 + 2\right), \\
B_1 &= ic_0\mu + ic_0\omega - \mu^2 - 2\mu\omega - \omega^2 + 1, \\
B_2 &= ic_0\mu + 2ic_0\omega - \mu^2 - 4\mu\omega - 4\omega^2 + 1.
\end{aligned} \tag{3.34}
$$

Equation (5.9) specifies an eigenvalue problem. The characteristic equation is obtained by setting the determinant of the coefficient matrix to be zero. For a set of parameters, when $n = 2$, there will be ten $\mu$'s, yet there exist only two principle roots. The four $\mu$'s with the smallest real parts are identified among all of the $\mu$'s. We choose one of these as $\mu_1$, and then apply Eqn. (3.30) with $k = 0$ to select the second principle $\mu$, such that $\mu_2 = -c_0 - \mu_1$. Letting $\mu = \alpha + i\beta$,

$$
\begin{aligned}
x_1(t) &= e^{(\alpha_1 + i\beta_1)t} \sum_{j=-2}^{+2} a_j e^{ij\omega t} = e^{\alpha_1 t} \sum_{j=-2}^{+2} a_j e^{i(j\omega + \beta_1)t}, \\
x_2(t) &= e^{(\alpha_2 + i\beta_2)t} \sum_{j=-2}^{+2} a_j e^{ij\omega t} = e^{\alpha_2 t} \sum_{j=-2}^{+2} a_j e^{i(j\omega + \beta_2)t}.
\end{aligned} \tag{3.35}
$$

Then the total response is $x(t) = A_1 x_1(t) + A_2 x_2(t)$. Real parts of $\mu$'s govern the exponential growth or decay of the solution. If any $Re(\mu) > 0$, the solution grows exponentially (unstable). The truncated response has terms of frequencies $j\omega + \beta_1$ and $j\omega + \beta_2$, $j = -n, \ldots, n$. If $\beta_1$ and $\beta_2$ are accurate, the full set of response frequencies will cover $j = -\infty, \ldots, \infty$. Equation (3.30) with $k = 0$ implies $\beta_2 = -\beta_1$ for our chosen principal roots.

## 3.3 Results

Analysis of the parametric excitation with periodic damping without and with the mean damping term (when $c_0 = 0$ and $c_0 \neq 0$, respectively) are presented in this section.

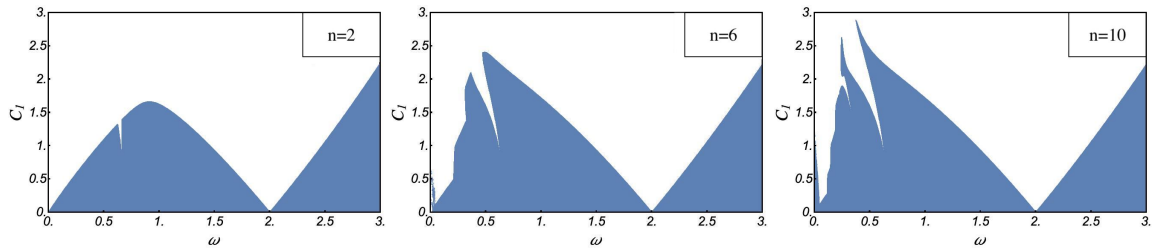


Figure 3.3: Stability boundaries when $c_0 = 0$ with the effect of the truncation order, $n$. (Blue is stable and white is unstable zone).

### 3.3.1 Zero Mean Damping, $c_0 = 0$

#### 3.3.1.1 Stability Boundaries

As explained in the previous section, when the real parts of $\mu_1$ and $\mu_2$ are negative or zero the solution is stable, whereas for any $\mu$ with a positive real part, the solution grows exponentially. Figure 3.3 demonstrates the stable and unstable regions for three different truncation orders, $n = 2$, $n = 6$ and $n = 10$ in the $(\omega, c_1)$ plane, where $\omega$ and $c_1$ are the frequency and amplitude of the harmonic damping. In this range, increasing the number of terms in the Fourier expansion provides a more precise solution. Increasing $n = 2$ to $n = 10$ in the truncated solution enhances the transition curves. Inside the tongues of instability (white zone) the response is unstable with underlying periodicity of period $2T$, whereas outside of the tongues (blue zone) the response is quasi-periodic (to be discussed in more detail below).

In Fig. 3.3 the truncated solution captures the subharmonic instability at $\omega = 2$ and superharmonic instability wedges based at $\omega = \frac{2}{3}$ and $\omega = \frac{2}{5}$. The existence of the wedge based at $\omega = \frac{2}{3}$ in Fig. 3.3 persists with increasing $n$. The wedge is not observed to reach the $\omega$ axis because of limited resolution of the plot, which was generated by plotting pixels. Other superharmonic tongues are not detected, and a wedge based at $\omega \approx 0$ and its connection to the subharmonic wedge, is erroneous. An improved description for low $\omega$ and large $c_1$ would require higher values of $n$. As shown in Fig. 3.3 when $n = 10$ the

higher truncation order reveals more and finer wedges of superharmonic instability.

Hortano and Burgh [38] studied a cyclically damped system (with $c_0 = 0$) based on a cyclic damping equation of the form $x'' + \epsilon \cos 2tx' + \Lambda x = 0$. They plotted transition curves as $\epsilon$ versus $\Lambda$, the square of the non-dimensionalized natural frequency, when the excitation frequency was fixed at 2. The relationships between the parameters in [38] and those in our model are $\epsilon = \frac{2c_1}{\omega}$ and $\Lambda = \frac{4}{\omega^2}$. The results in [38] for cyclic damping show instability wedges based at $\Lambda = 1$ and 9 (and generally values of $m^2$ for odd values of $m$). The wedges based at $\Lambda = 4, 16, \ldots$ (generally $m^2$ for even values of $m$), which are known to occur in the Mathieu equation, are collapsed, such that the boundaries overlap into a single curve and instability does not occur (associated with coexistence, discussed later). All of these wedge base points correspond to $\omega = 2, 1, \frac{2}{3}$, and $\frac{1}{2}$ in Fig. 3.3, for which wedges based at 2 and $\frac{2}{3}$ are not coexistent and are observed in convergent plots of Fig. 3.3. Thus the two studies are consistent.

#### 3.3.1.2 Response Frequency Analysis

The classical Floquet-based analysis describes the properties of Eqn. (3.1) such as stability boundaries [54], while the truncated solution method provides the characteristics of the response in addition to the tongues of instability. The approximate solution contains an exponential and a periodic part. A combination of Floquet exponents and excitation harmonics comprises the frequency of the response. The response frequencies in the truncated solution are $Im(\mu) + j\omega$, where $j = \pm 1, \pm 2, ..., \pm n$ and $n$ is the number of assumed harmonics. Figure 3.4 shows the response frequencies of the truncated solution as functions of $\omega$ for $c_0 = 0$, $c_1 = 1$, and the truncation orders $n = 2$ and $n = 4$. At the instability wedges based at $\omega = \frac{2}{m}$, $m = 1, 3, 5, ...$, the Fourier expansion of the periodic part of the response has harmonics of $\frac{m\omega}{2}$, $m = 1, 3, 5, ....$ In instability wedges based at $\omega = \frac{2}{m}$, $m = 2, 4, 6, ...$, the Fourier expansion of the periodic part of the response has harmonics of $\frac{m\omega}{2}$, $m = 2, 4, 6, ....$ For example near $\omega = 2$ the response frequencies are

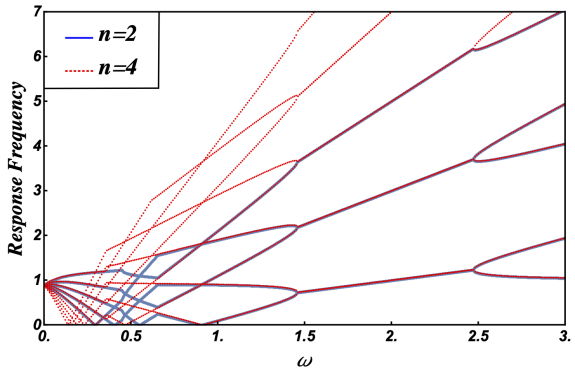


Figure 3.4: Frequencies of the response when $c_0 = 0$ and $c_1 = 1$.

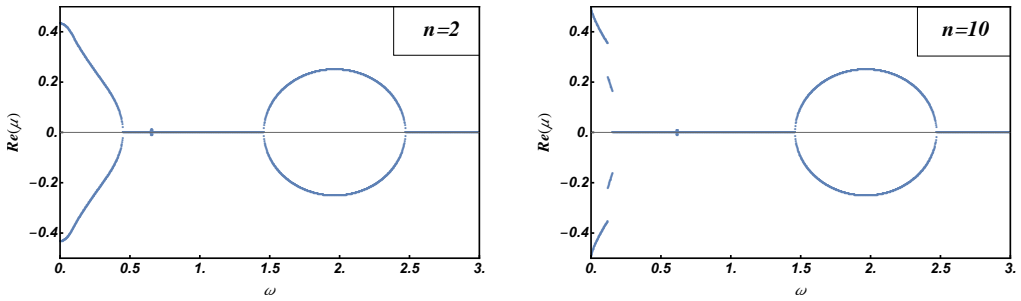


(a) $n = 2$ (b) $n = 10$

Figure 3.5: Growth and decay factors as quantified by $Re(\mu)$ when $c_0 = 0$ and $c_1 = 1$. $(a)$ and $(b)$ show the effect of the truncation order, $n$.

$\frac{\omega}{2}$, $\frac{3\omega}{2}$ and $\frac{5\omega}{2}$ and at the crossing near $\omega = 1$ the response frequencies are $\omega, 2\omega$ and $3\omega$.

With varying $\omega$, pairs of branches may merge into single branches or cross one another at isolated points. Intervals where two frequency branches have merged into one branch are associated with instability zones in the stability diagram and with the stability transition points in the Floquet circle (Fig. 3.2, case of $c_0 = 0$). In the intervals of instability $Re(\mu_{1,2}) = \pm\alpha$ and $Im(\mu_{1,2}) = \pm\beta$. Merging of two branches into one branch indicates a stability transition and the interval of merging represents the instability tongues. Branches crossing at one point indicate that there is no frequency-merging interval, such that would-be wedge boundaries overlap and the periodic responses on the boundaries coexist and therefore coexistence phenomena is happening.

#### 3.3.1.3 Growth/Decay Factor

In the approximate solution the real part of the Floquet exponent specifies the exponential growth. Figure 3.5 shows $Re(\mu)$ as a function of $\omega$ when $c_0 = 0$. The graph shows two intervals where the Floquet exponents have two different values for the real parts, forming "bubbles" in the graph (a tiny bubble near $\omega \approx 0.61$, and a large bubble centered at $\omega = 2$). $Re(\mu) > 0$ denotes growth in the truncated solution, and therefore yields instability. In the case of stability, the least negative value governs the decay rate. Therefore, the diagram indicates the growth and decay factors of the response. While Fig. 3.5a demonstrates an instability near $\omega = 2$, $\omega = 0.61$ and $\omega < 0.38$ for $c_0 = 0$, numerical studies suggest that the latter case is a truncation error, and there are indeed mostly stable solutions for $\omega < 0.38$. For low values of $\omega$ the lower truncation is not sufficient to describe the vibration solution or stability. This erroneous range of $\omega$ is reduced with increasing truncation order $n$. In Fig. 3.5, two different orders of truncation illustrate the benefit of higher values of $n$ in approximating the solution for lower frequencies.

#### 3.3.1.4 Coexistence when $c_0 = 0$

Coexistence phenomenon occurs when stability transitions overlap and the tongues of instability disappear (black lines in Fig. 3.6a). Figure 3.6a shows that stability tongues collapse into lines based at $\omega \approx 0.91$ and $\omega \approx 0.46$. The thin instability tongue based at $\omega \approx 0.61$ is associated with the small bubble in the growth/decay factor diagram (Fig. 3.6a) and the small frequency-merging interval in the response frequency plot (Fig. 3.6b). Figure 3.6a shows the properties of the stable and unstable responses, transition boundaries and coexistence curves, and whether the response is periodic or quasi-periodic. "Unstable Periodic" means unstable exponential growth modulates an oscillation that is otherwise periodic (not quasi-periodic). In the wedges, based at $\omega = \frac{2}{m}$, $m = 1, 3, 5, \ldots$, this periodic part has period $2T$. At coexistence the response is periodic with period $T$.

In the growth/decay factor diagram of Fig. 3.6a the bubbles, normally associated

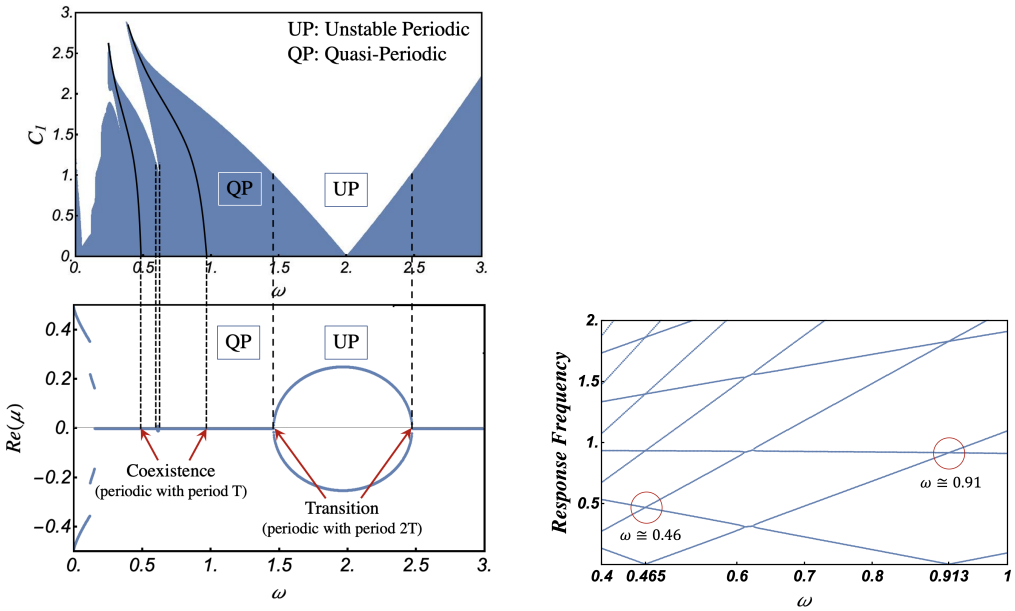


(a) (b)

Figure 3.6: $(a)$ Coexistence in the stability diagrams with $c_0 = 0$, and a plot of growth/decay factors with $c_0 = 0$ and $c_1 = 1$. $(b)$ Zoomed-in response frequency diagram with $c_0 = 0$ and $c_1 = 1$.

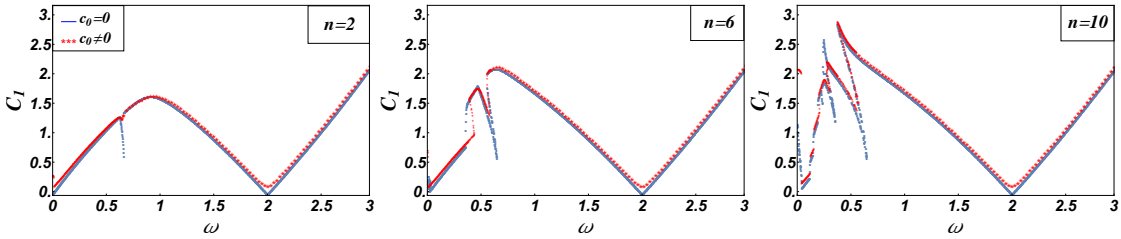


Figure 3.7: Stability boundaries when $c_1 = 1$ for $c_0 = 0$ and $c_0 = 0.05$, using three different truncation orders.

with the instability zones, collapse and thus no bubble appears at coexistence points. In Fig. 3.6b, one can see that coexistence corresponds to the crossing points in the response frequency plot, where periodic solutions cross one another at $\omega \approx 0.91$ and $\omega \approx 0.46$.

### 3.3.2 Non-zero Mean Damping $c_0 \neq 0$

For $c_0 \neq 0$ the stability boundaries and each of the response features are affected by mean damping. In order to determine the effect of damping the previous analysis is repeated for the case $c_0 \neq 0$.

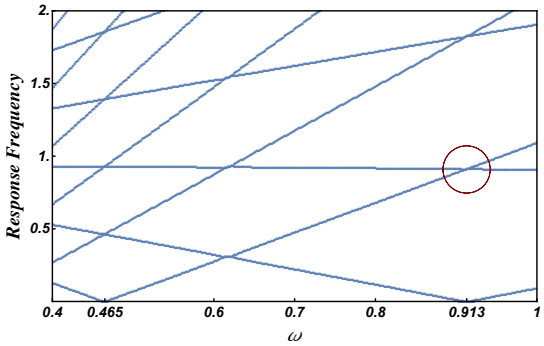


Figure 3.8: Response frequencies when $c_0 = 0.05$ and $c_1 = 1$. Note the small interval of merged frequencies, as highlighted by the circle.

#### 3.3.2.1 Stability Boundaries

Figure 3.7 shows the stability diagrams when $c_0 = 0.05$ (red) for three different truncation orders and compares with the stability boundaries when $c_0 = 0$ (blue). As noted before, a higher truncation number produces more accurate stability curves within lower frequency ranges. It can be perceived how the stability boundaries are affected by damping. A small addition of mean damping smoothens the wedge tips and shrinks the instability zones.

#### 3.3.2.2 Response Frequency Analysis

Figure 3.8 zooms into the response frequency plot when $c_0 = 0.05$. In Fig. 3.6b a frequency crossing at $\omega \approx 0.91$ indicated the coexistence phenomenon for $c_0 = 0$. However, for $c_0 \neq 0$ the crossing turns into an interval and the coexistence line disappears. For the lower frequency, $\omega \approx 0.46$, at which we had coexistence with $c_0 = 0$, the truncation order and resolution are not sufficient to clearly distinguish whether $c_0 \neq 0$ produces an interval.

#### 3.3.2.3 Growth/Decay Factor

Figure 3.9 illustrates that the added mean damping shifts the growth/decay diagram downward and the shift is $\frac{c_0}{2}$, which is consistent with Eqn. (3.30). In Fig. 3.9 at $\omega \approx 0.91$ a small bubble pops up at the location where coexistence happens (no bubble for $c_0 = 0$). One might expect the coexistence line in Fig. 3.6a to separate and form an instability wedge when the merging interval of $Im(\mu)$ appears. But since the bubble occurs with values of

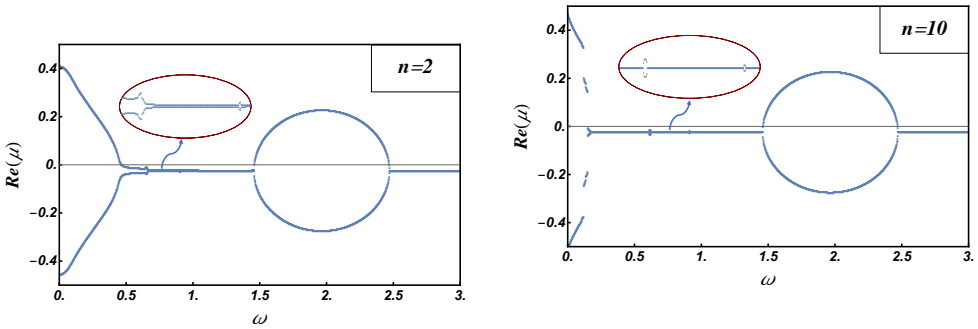


Figure 3.9: Growth and decay factors when $c_0 = 0.05$ and $c_1 = 1$. On the left, $n = 2$. On the right, $n = 10$.

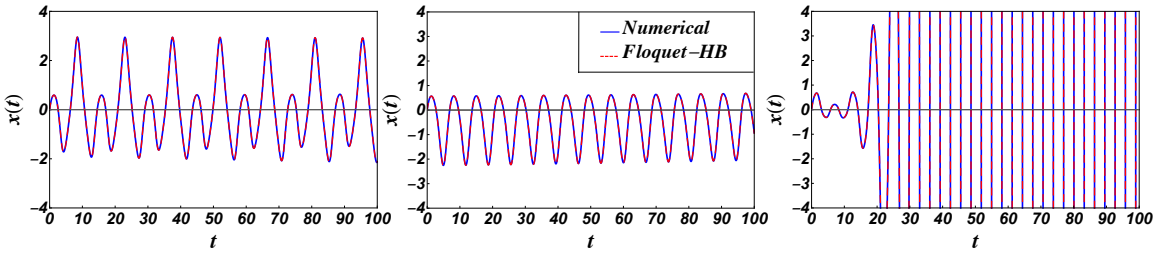


(a) $\omega = 1.3$ (stable) (b) $\omega = 0.91$ (near coexistence) (c) $\omega = 2$ (unstable)

Figure 3.10: Time responses when $c_0 = 0$, $c_1 = 1$ and $n = 3$.

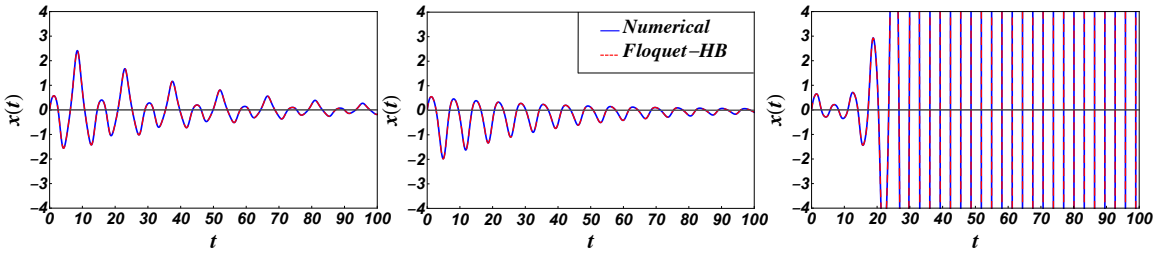


(a) $\omega = 1.3$ (stable) (b) $\omega = 0.91$ (near coexistence) (c) $\omega = 2$ (unstable)

Figure 3.11: Time responses when $c_0 = 0.05$, $c_1 = 1$ and $n = 3$.

$Re(\mu_1) < Re(\mu_2) < 0$ the response stays stable. Thus, no instability tongues appear near $\omega \approx 0.91$ in Fig. 3.7, although the crossing point has turned into an interval in Fig. 3.8. By increasing the amplitude of the parametric damping ($c_1$) the bubble in $Re(\mu)$ values in Fig. 3.9 grows but does not cross zero and the system stays stable. As $\omega$ increases and the small bubble is reached in Fig. 3.9, two complex multipliers $\lambda$ (recall $\lambda = e^{\mu T}$) on the circle

in Fig. 3.2 collide on the positive real axis. As $\omega$ continues to increase, $\lambda_1$ and $\lambda_2$ split on the real axis, and then come back together and collide again in Fig. 3.2, as the far end of the bubble is reached in Fig. 3.9. When $\omega$ increases beyond the bubble, $\lambda_1$ and $\lambda_2$ are on the circle and are complex. For values of $\omega$ in the bubble, $\lambda_1$ and $\lambda_2$ are real with $|\lambda_1| < 1$ and $|\lambda_2| < 1$ ($\mathrm{Re}(\mu_1) < 0$ and $\mathrm{Re}(\mu_2) < 0$)) and the system is stable (in this example). The response has exponential decay that modulates an oscillation that is otherwise of period $T$.

#### 3.3.2.4 No Coexistence when $c_0 \neq 0$

The previous discussion indicates that by adding a mean damping to the system the coexistence is disrupted. The frequency-branch crossings are perturbed into frequency-branch mergers over small intervals. With the frequency branch interval a bubble forms in the graph of the $Re(\mu)$, which was not a characteristic of coexistence. However, the $Re(\mu)$ is pushed to be negative (in the example shown) and so the bubble may not generate an instability although it is conceivable that instability could happen if $c_1$ is increased enough. The overlapping instability transition boundaries, which are seen in coexistence, separate with the emergence of the frequency-branch interval, but are no longer serving as stability boundaries since the $Re(\mu)$ has been reduced by $\frac{c_0}{2}$.

While coexistence is disrupted by the addition of slight damping (or probably other perturbations), it is important as a limiting case, since it points to a near description of behavior for the case of very small mean damping.

The importance of studying coexistence comes into sight when the system parameters are positioned on the coexistence line. It is possible that arbitrary perturbations may open up the coexistence line and generate instabilities and the response may fall into unstable zone. The shaded area in the stability diagrams, where the system parameters are located in the “safe" stability zone indicates the best possible parameters for design. As such, parameter values near the coexistence line may be avoided if instability is undesirable.

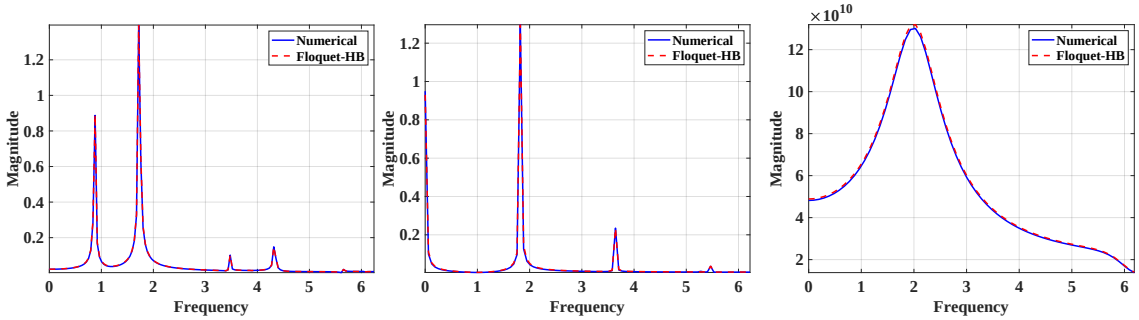


(a) $\omega = 1.3$ (stable) (b) $\omega = 0.91$ (near coexistence) (c) $\omega = 2$ (unstable)

Figure 3.12: FFTs for $c_0 = 0$, $c_1 = 1$, $n = 3$, where the axes are nondimensional.

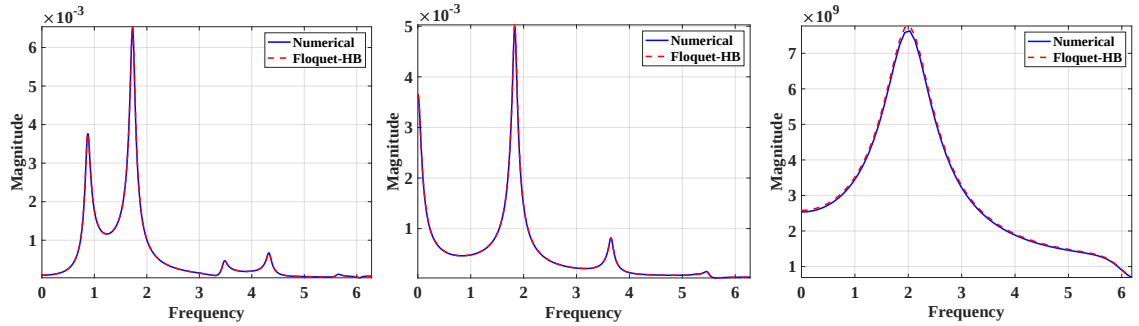


(a) $\omega = 1.3$ (stable) (b) $\omega = 0.91$ (near coexistence) (c) $\omega = 2$ (unstable)

Figure 3.13: FFTs for $c_0 = 0.05$, $c_1 = 1$, $n = 3$, where the axes are nondimensional.

### 3.3.3 Response of Undamped and Damped Systems

Depending on the parameters, the system may be stable, neutrally stable or unstable. Three sets of parameters, associated with three types of stability, are chosen from the stability diagram to obtain the truncated solution of Eqn. (3.26). Figures 3.10 and 3.11 illustrate both the numerical and the truncated solutions for the sets of parameters when $c_0 = 0$ and $c_0 = 0.05$, respectively. The truncated solution with $n = 3$ truncation order agrees with the numerical analysis for the chosen sets of parameters.

Figure 3.10a represents a quasi-periodic bounded response. In this case the quasi-periodic drift occurs on a long time scale and is only slightly detectable in the plot. Figure 3.10b, for which $\omega = \omega_1 = 0.91$ is very close to coexistence, and therefore looks periodic with period $T_1 = \frac{2\pi}{\omega_1} \approx 6.904$. Figure 3.10c shows a subharmonic unstable solution at a periodicity of

$2T_2 = \frac{4\pi}{\omega_2} \approx 6.28$ for which $\omega = \omega_2 = 2$ ($T_2$ is the period of excitation).

Figures 3.11a and 3.11b show exponentially stable solutions with frequency characteristics similar to those in Fig. 3.10a and 3.10b and additional mean damping. Figure 3.11c is unstable despite the mean damping. A very slight decrease in the growth rate compared to Fig. 3.10c can be detected on careful inspection. Putting the mean damping into effect for the same system parameters ($c_0 \neq 0$) dampens the response with little effect on frequency content.

The fast Fourier transforms (FFTs) of the truncated solutions are compared with those of the numerical solutions in Figs. 3.12 and 3.13. The analytical truncation order is $n = 3$. The frequency content of analytical and numerical solutions for the chosen excitation frequencies are consistent. However, for small values of $\omega$ the truncated and numerical solutions do not agree. Increasing the truncation order improves the accuracy of the results compared with the numerical solution.

## 3.4 Conclusion

We studied the dynamics of an oscillator with cyclic damping, which was motivated by vertical-axis wind-turbine blade dynamics. Specifically, we sought approximate analytical solution to a linear second-order differential equation with a periodic damping coefficient and observed the characteristics of the response.

We sought a general Floquet solution in which the periodic part was approximated with a truncated Fourier series. Applying harmonic balance led to a relationship between the Floquet exponents, Fourier coefficients, and the parameters.

The exponents were then used to formulate the response to the initial conditions, the response frequency content, and the stability characteristics. The theoretical responses of the system and their FFTs were compared with the numerical solutions, and the consistency of the responses for different sets of parameters was shown. The analysis is good if $\omega$ is not too small and can be improved by increasing the analytical truncation order, $n$. Limits

on the truncation order were not investigated.

For the case when there was zero mean damping we captured a phenomenon called "coexistence". Coexistence has been recognized to occur when stability boundaries overlap such that the instability wedges disappear. This is accompanied by a crossing of response frequencies as the frequency of excitation changes, and an absence of a "bubble" in the real part of the Floquet exponents (meaning the real part of the Floquet exponents is repeated). We found that the addition of mean damping disrupted the features of coexistence such that the response frequencies merged over a parameter interval, in which the real parts of the Floquet exponents became distinct (forming a bubble in the plot of $Re(\mu)$ versus $\omega$). In such case an unstable wedge may not appear in the parameter range at hand since the mean damping can stabilize the responses in very slender wedges.

The results of this study may have relevance to VAWTs. The presence of cyclic damping in VAWTs, especially if aeroelastic effects reduce the effective mean damping, suggests the potential for instabilities of the same pattern as is familiar with cyclic stiffness, namely at excitation frequencies near $\frac{2\omega_n}{k}$, $k = 1, 2, \ldots$. In the case of cyclic damping, the even values of $k$ represent coexistence in the ideal model and the system does not actually destabilize. However, perturbations of the model could destabilize the coexistence events and thus designs should avoid these frequencies.

# CHAPTER 4

## RESPONSE CHARACTERISTICS OF SYSTEMS WITH COMBINED PARAMETRIC EXCITATION

Parametric excitation occurs in many mechanical, damped or undamped, systems of interest. In some applications and structures, for example horizontal axis wind turbine (HAWTs) blades, periodic stiffness induces parametric excitation to the system [3]. While in vertical axis wind turbine (VAWTs) blades the structure experiences parametric damping [6, 9]. Sevin observe an auto-parametric excitation in a pendulum-type vibration absorber on the basis of approximate nonlinear equations of motion. [97]. The investigation on a thin cantilever beam under harmonic excitation by Dugundji and Mukhopadhyay concluded in Mathieu equations coupled by symmetric, off-diagonal parametric excitation terms. The equation shows combination resonance with primary instability and the steady limit cycles developed at the instability region. The experimental results are also given for an actual beam showing the existence of the primary instability regions and the associated nonlinear limit cycles with good agreement[26]. Several methods have been used to study parametrically excited systems. Floquet theory and perturbation methods have been applied to the Mathieu equation to study the stability criteria and the solution for undamped and damped, forced and unforced systems [3, 6, 45, 61, 72, 75, 86–89, 95, 112, 120]. Taylor and Narendra studied the stability boundaries of the damped Mathieu equation by using a perturbation method [105]. Yu and Mote Jr studied the parametric excitation, natural frequencies and modes of transverse vibration in asymmetric circular plates having small imperfections applying perturbation method[121]. Rand et al. approximated the stability regions of systems with quasiperiodic stiffness using four different methods: numerical integration, Lyapunov exponents, regular perturbation and harmonic balance[86]. In [61, 75, 86, 88] Rand and his colleagues discussed the phenomena called “coexistence" in Ince’s equation, and Recktenwald and Rand studied the generalization of results obtained previously when applied to the generalized Ince’s equation[89]. Sofroniou and Bishop

investigated the dynamics of parametrically excited systems with two forcing terms[99].

The majority of the research on parametric excitation in frequency domain analysis have been limited to a single harmonic approximation. It is conceivable that tower shadowing in HAWTs or other aerodynamic effects in VAWTs may induce cyclic fluctuations with multiple harmonics. These systems have a homogeneous plus particular solution. The particular solution appears in the forced systems when an external force or a displacement excitation is exerted to the system and it displays the steady-state response of the system. While the homogeneous system is the "unforced" parametrically excited system ($g(t) = 0$) and the solution represents the transient dynamics[30]. In this work we focus on the transient dynamics of the parametrically excited systems. A linear differential equation having periodic coefficients with multiple harmonics is called Hill's equation,

$$(1 + A(t))d^2x + B(t)dx + (c + D(t))x = 0. \tag{4.1}$$

Hill's equation is a generalized form of original Ince's equation,

$$(1 + a\cos 2t)d^2x + b\sin t dx + (c + d\cos 2t)x = 0, \tag{4.2}$$

which occurs in a variety of mechanical systems[70, 88]. When $a = b = 0$, Hill's equation reduces to $\ddot{x} + f(t)x = 0$, describes undamped system with cyclic stiffness [88]. Acar and Feeny applied Floquet theory on Hill's equation for the special case where $A(t) = B(t) = 0$ and $c = 1$. This is the generalization of the Mathieu's equation with harmonic stiffness term. Reduced-order models of the vibration of horizontal-axis wind turbines have often made use of a forced Mathieu-Hill equation, which may include damping, such that the equation has the form $\ddot{x} + 2\zeta\dot{x} + f(t)x = g(t)$ where $f(t)$ and $g(t)$ are periodic[3, 11, 46, 83]. Basic models of vertical-axis wind turbines with aeroelastic force can be represented by oscillators with cyclic damping in nondimensional form [9]:

$$\ddot{x} + 2\zeta f(t)\dot{x} + x = g(t) \tag{4.3}$$

Suppose the parametric excitation term is expressed with $f(t) = c_0 + c_1 \cos \omega t + c_2 \cos(2\omega t + \phi)$, where $c_j$s are the strength of harmonics, then the equations of interest are,

- Parametrically damped system:

$$\ddot{x} + (c_0 + c_1 \cos \omega t + c_2 \cos(2\omega t + \phi))\dot{x} + x = g(t), \tag{4.4}$$

- Mathieu's equation (when $c_0 = 1$):

$$\ddot{x} + (1 + c_1 \cos \omega t + c_2 \cos(2\omega t + \phi))x = 0. \tag{4.5}$$

and all the possible combinations of of Eqns (4.4) and (4.5).

Generally the Floquet theory can be applied to systems with the state-variable form

$$\dot{\mathbf{x}} = \mathbf{A}(t)\mathbf{x} \tag{4.6}$$

In which $\mathbf{x}$ is an $N \times 1$ state vector and $\mathbf{A}(t)$ is $N \times N$ and periodic with period $T = \frac{2\pi}{\omega}$.

Floquet properties imply that the characteristic exponents are not unique, since if $\rho_j = e^{\mu_j T}$, then $\rho_j = e^{(\mu_j + \frac{2\pi i}{T})T}$. If $\rho_k = e^{\mu_k t}$, based on the Floquet properties the charachteristics multipliers (eigenvalues) of $A(t)$ in Eqn. (5.4), when $A(0) = I$ satisfy:

$$\rho_1 \rho_2 ... \rho_n = exp(\int_0^T tr(A(s))ds), \tag{4.7}$$

In this work, for the purpose of increasing our understanding of the parametric excitation with multiple harmonics, we study the parameterically damped system (Eqn. 4.4) and also the unforced, undamped Mathieu equation (Eqn. 4.5), using an analysis based on Floquet theory, both with two-harmonic parametric excitation and direct excitation $g(t) = 0$.

## 4.1 Analysis

The Floquet analysis combined with harmonic balance will be applied on both Eqns (4.4) and (4.5). However, in this section we will show details of the analysis of the damped

and undamped Mathieu's equation with two-harmonic parametric excitation of the form of Eqn. (4.5) and skip the details about Eqn. (4.4)

We sought an approximate solution based on Floquet theory following the approach in [3, 6]. The equation in state-space form is

$$\begin{aligned}\dot{\mathbf{x}} &= \begin{pmatrix} \dot{x} \\ \ddot{x} \end{pmatrix} = \begin{bmatrix} 0 & 1 \\ -(1 + c_1 \cos\omega t + c_2 \cos(2\omega t + \phi)) & 0 \end{bmatrix} \begin{pmatrix} x \\ \dot{x} \end{pmatrix} \\ &= \mathbf{A}(t)\mathbf{x}, \end{aligned} \tag{4.8}$$

where $\mathbf{A}(t)$ is a periodic matrix with period $T = \frac{2\pi}{\omega}$. We seek a solution of the form $x = e^{\mu t} p(t)$. Using a truncated series approximation, we write

$$x(t) \cong e^{\mu t} \sum_{j=-n}^{+n} a_j e^{ij\omega t}. \tag{4.9}$$

"$\mu$" is the Floquet exponent and "$a_j$"'s are Fourier coefficients. A truncated approximated series solution is extracted from the infinite series solution. The imaginary part of the Floquet exponent unites with the excitation frequency to form the response frequency. The approximated solution is substitute into Eqn. (4.5), and then harmonic balance is applied on the coefficients of the $e^{ij\omega t}$. The harmonic balance results in an equation of the form $\mathbf{K}(\mu)\mathbf{a} = 0$, which has the detailed form,

$$\begin{bmatrix} B_{-n} & & & & & & & \\ & \ddots & & \vdots & \vdots & & & \\ & \dots & B_{-2} & \frac{c_1}{2} & \frac{c_2}{2} & 0 & 0 & \dots \\ & & \frac{c_1}{2} & B_{-1} & \frac{c_1}{2} & \frac{c_2}{2} & 0 & \\ & & \frac{c_2}{2} & \frac{c_1}{2} & B_0 & \frac{c_1}{2} & \frac{c_2}{2} & \\ & & 0 & \frac{c_2}{2} & \frac{c_1}{2} & B_1 & \frac{c_1}{2} & \\ & & 0 & 0 & \frac{c_2}{2} & \frac{c_1}{2} & B_2 & \\ & & & & \vdots & \vdots & & \ddots \\ & & & & & & & B_n \end{bmatrix} \begin{pmatrix} a_{-n} \\ \vdots \\ a_{-1} \\ a_0 \\ a_1 \\ \vdots \\ a_n \end{pmatrix} = \begin{pmatrix} 0 \\ \vdots \\ 0 \\ 0 \\ 0 \\ \vdots \\ 0 \end{pmatrix}, \tag{4.10}$$

where $B_j = 1 - (\mu + j\omega)^2$ for $j = -n, ..., n$.

## 4.2 Application to Two-harmonic Mathieu

### 4.2.1 Analysis of the Truncated Solution

When $n = 2$, Eqn. (4.10) takes the form

$$\begin{bmatrix} B_{-2} & \frac{c_1}{2} & \frac{c_2}{2} & 0 & 0 \\ \frac{c_1}{2} & B_{-1} & \frac{c_1}{2} & \frac{c_2}{2} & 0 \\ \frac{c_2}{2} & \frac{c_1}{2} & B_0 & \frac{c_1}{2} & \frac{c_2}{2} \\ 0 & \frac{c_2}{2} & \frac{c_1}{2} & B_1 & \frac{c_1}{2} \\ 0 & 0 & \frac{c_2}{2} & \frac{c_1}{2} & B_2 \end{bmatrix} \begin{pmatrix} a_{-2} \\ a_{-1} \\ a_0 \\ a_1 \\ a_2 \end{pmatrix} = \begin{pmatrix} 0 \\ 0 \\ 0 \\ 0 \\ 0 \end{pmatrix}. \tag{4.11}$$

This is essentially an eigenvalue problem (EVP). Obtaining a nonzero solution for Fourier coefficients, $a_j$s, requires that $|\mathbf{K}(\mu)| = 0$, which express the characteristic equation for $\mu$. The characteristic equation is a $(2n + 1)$th degree polynomial in $\mu^2$, which provides with $(4n + 2)$ solutions for $\mu$. However, since in this work the state space has two dimensions, as stated by Floquet theory there exist two distinct roots, referred as principal roots. Based on this theory [112],

$$e^{(\mu_1+\mu_2)T} = exp(\int_0^T tr(\mathbf{A}(s))ds. \tag{4.12}$$

When the system is undamped the trace of the coefficient matrix in Eqn. (5.4) is zero. Therefore, Eqn. (5.11) reduces to $(\mu_1 + \mu_2)T = \pm 2\pi ik$, where $k$ is integer. $T = \frac{2\pi}{\omega}$ leads to the criterion

$$\mu_1 + \mu_2 = \pm k\omega i \tag{4.13}$$

Equation (4.13) expresses the relation between the proper principal roots. In this study the strength of the second excitation harmonic is consider to be a scaling of the strength of the first harmonic ($c_2 = \gamma c_1$).

## 4.3 Results

The generated polynomial for $\mu$ is a function of the set of parameters, $c_0, c_1, \gamma, \omega$ and $\mu$.

$$f(c_0, c_1, \gamma, \omega, \mu) = 0 \tag{4.14}$$

Set $c_0, c_1$ and $\gamma$ constant and solve Eqn. (4.14) for varying $\omega$, Fig. 4.1 represents the locus of $(4n + 2)$ roots (principal and redundant) for varying $\omega$ when the truncation number is two ($n = 2$). Note that here the real axis is the ordinate and the $Im$ axis is the abscissa. The smaller blue dots follow the locus of the roots for smaller values of $\omega$ while the larger red dots indicate the $4n + 2$ roots obtained when $\delta = 0.8$ and $\omega = 2.2$. The roots of our interest (principal roots) are two of the inner-most roots which satisfy the Floquet criterion (4.13).

### 4.3.1 Growth and Decay Factor

Figure 4.2 illustrates the real parts of $\mu$ versus $\omega$. One positive real part results an unstable solution. If $Re(\mu) = 0$ then the solution is bounded and quasi-periodic, while a non-zero real part ends in an unbounded response, since $k = 0$ in Eqn. (4.13) yields to $\mu_1 = -\mu_2$. Accordingly, the transition from zero to non-zero real part of the $\mu$s defines the stability curves (section 5.3.2).

### 4.3.2 Stability Analysis

Most studies focus on stability regions by looking for transitional periodic responses. In this work we use transitions in the generally computed Floquet exponents. Stability diagrams describe the regions of stability for pairs of $\delta$ and $\omega$, and the boundaries express the transition from Floquet exponents with zero real parts to those with a positive real part. Figure 4.3a demonstrates the regions of stability for $\gamma = 0.5$ and $\phi = 0$ when $n = 2$ in the truncated solutions. Blue (dark) and white zones in Fig. 5.5 stand for stable and unstable regions, respectively. The values of $(\delta, \omega)$ pairs in the instability wedges are affirmed by the positive real parts in Fig. 4.2, when $\delta = 0.8$. For positive values of $Re(\mu)$ the response is unbounded.

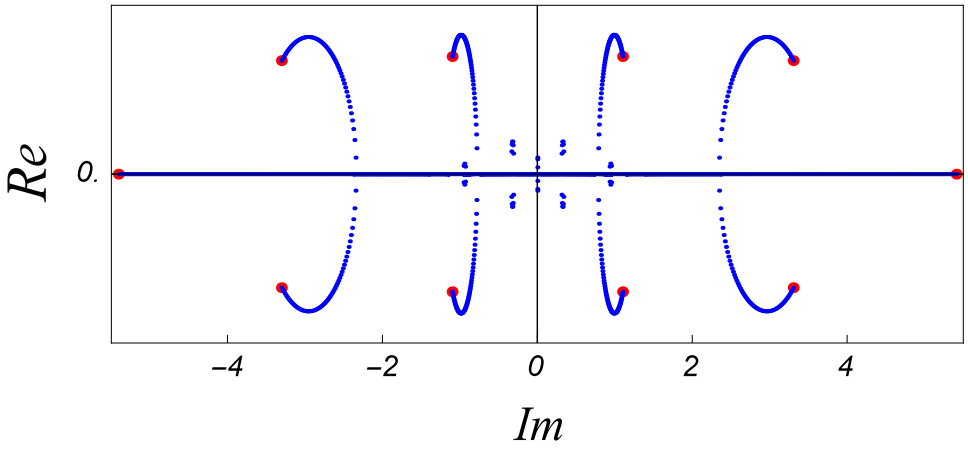


Figure 4.1: The locus of the roots for $\delta = 0.8$ and $\gamma = 0.5$. $\omega$ is varying from 0 to 2.2.

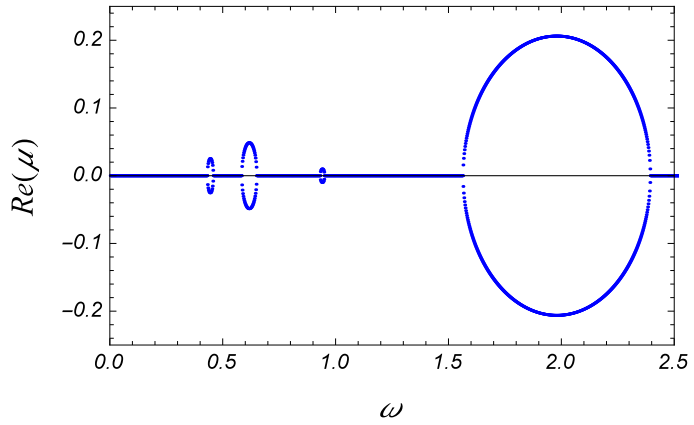


Figure 4.2: Growth factor for $\delta = 0.8$ and $\gamma = 0.5$.

In comparison with regular Mathieu equation (not shown), the subharmonic wedge (near $\omega = 2$) is visibly unchanged, but the primary ($\omega = 1$) wedge has been clearly distorted. Similar distortion was observed in [99]. The superharmonic and primary instability wedges actually come down to the $\omega$ axis, but become so thin that they are lost in the resolution of the plots.

Numerical studies show that there is a truncation error for lower values of frequencies. This error reduces with increasing truncation order $n$ (Fig. 4.3b). Tiny tongues of stability

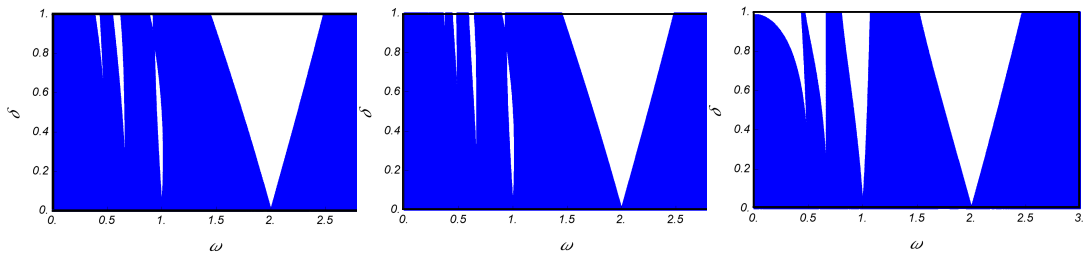


(a) $n = 2$ (b) $n = 6$ (c) $n = 2$ AND $\phi = \frac{\pi}{2}$

Figure 4.3: Stability boundaries for $\gamma = 0.5$.

are captured in higher order analysis for lower values of frequencies. Generally the solution deteriorates for small $\omega$ and large $\delta$, and increasing $n$ increases the range of accuracy of the approximated solution. However, there may be limits on $n$, as the EVP involves the roots of a polynomial of degree $2n + 1$.

The relative parametric excitation phase $\phi$ can effect stability. A a phase shift of $\phi = \frac{\pi}{2}$ turns the second harmonic from $\cos 2\omega t$ to $\sin 2\omega t$ and further investigations for the stability criteria indicate that the region of subharmonic instability (based at $\omega = 2$) does not change noticeably, whereas the primary (near $\omega = 1$) and superharmonic unstable zones get wider in Fig. 4.3c compared to Figs. 4.3a and 4.3b, and also compared to the regular Mathieu equation [3, 88]. The examples we have run (others not shown) show that $\phi$ can have a stabilizing or destabilizing affect relative to the single-harmonic undamped Mathieu system.

### 4.3.3 Response Analysis

#### 4.3.3.1 Time Response

The general solution to differential equations is

$$x(t) = C_1 x_1(t) + C_2 x_2(t) \tag{4.15}$$

where $x_k(t)$ is expressed in Egn. (4.9) as

$$x_k(t) = e^{\mu_k t}[e^{-ni\omega t}, ..., e^{-i\omega t}, 1, e^{i\omega t}, ..., e^{ni\omega t}]^T \mathbf{a}_k \tag{4.16}$$

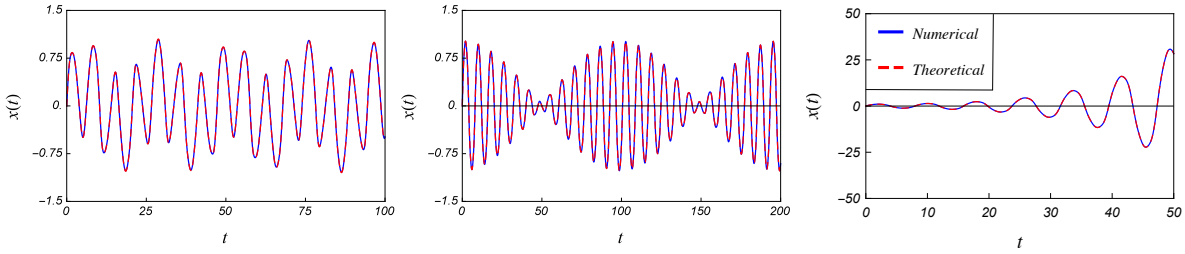


(a) $\omega = 1.2$ (b) $\omega = 1.56$ (c) $\omega = 1.6$

Figure 4.4: Time responses for $n = 3$, $\gamma = 0.5$ and $\delta = 0.8$. (Three different frequencies, $\omega = 1.2$,$\omega = 1.56$ and $\omega = 1.6$).

for $k = 1, 2$, where $\mathbf{a}_k$s are determined in Eqn. (4.11). $C_1$ and $C_2$ are determined by the initial conditions. Using Eqns. (4.9) and (5.13) the system has a general solution of the form

$$x(t) = C_1 e^{\mu_1 t}\left(a_{-n}e^{-nit\omega}\ldots + a_{-1}e^{-it\omega} + a_0 + a_1 e^{it\omega}\ldots + a_n e^{nit\omega}\right) + C_2 e^{\mu_2 t}\left(a_n e^{-nit\omega}\ldots + a_1 e^{-it\omega} + a_0 + a_{-1}e^{it\omega}\ldots + a_{-n}e^{nit\omega}\right) \tag{4.17}$$

For $x(0) = 0$ and $\dot{x}(0) = 1$, coefficients $C_1$ and $C_2$ were determined. Inserting $\mu_1$ and $\mu_2$, extracted from the EVP, into Eqn. (5.14) leads to the time response, which we have plotted for three sets of parameters corresponding to stable, nearly periodic transitional and unstable responses, respectively. The responses were very well matched with the numerical responses when we increased the truncation number to $n = 3$. In Fig. 5.1, $\omega = 1.2$ sits in a stable region and shows a quasi-periodic motion with multiple harmonics, while $\omega = 1.56$ is in the vicinity of the boundary of stability (see Fig. 5.3, near the frequency merger point, where two branches meet as in the next section). Zooming on the response frequensies plots detects that the frequencies of harmonics are slightly different such that the “beating phenomenon" occurs. For $\omega = 1.6$ the reponse is unstable and unbounded.

#### 4.3.3.2 Response Frequencies

Seeing that the approximated general response is a combination of an exponential part and a periodic part, the frequencies of the response are a formation of the $\pm j\omega$ combined with

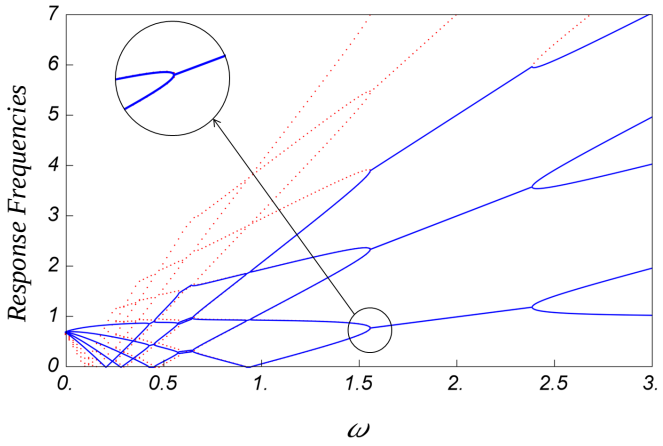


Figure 4.5: Response frequencies for $\delta = 0.8$ and $\gamma = 0.5$. Blue is for $n = 2$ and red dotted line is for $n = 3$.

the imaginary part of the exponents, i.e., $\omega_j = Im(\mu) \pm j\omega$, where $j = 0, 1, 2, ..., n$.

In Fig. 5.3 the frequencies of the response for $\gamma = 0.5$ and $\delta = 0.8$ are shown. Solid lines indicate the frequency branches when $n = 2$ and the dotted lines are for $n = 4$. We can increase the accuracy and choose any number of branches by increasing the truncation order (Fig. 5.3). Agreement between the dotted and solid curves shows that, for $n = 2$, convergence has ocurred for $\omega \geq 0.6$, but the trend is consistent for lower values of $\omega$. In regions of stability the truncated expansion represents $2n + 1$ of the response frequencies. In the transition from the stable to unstable region, repeated frequencies occur when two branches merge into one with repeated values of $\omega/2, 3\omega/2, ..., (2n + 1)\omega/2$ response frequencies. In comparison to Fig. 4.3a and 4.3b, the primary instability wedge is very thin for $\delta = 0.8$. Likewise the frequency merger interval in Fig. 5.3 near $\omega = 1$ is imperceptible.

## 4.4 A System with Two-harmonic Parametric Damping

A truncated expansion has been applied to a system with one-harmonic parametric damping and the response has been studied[6]. As an extension, the Floquet expansion is

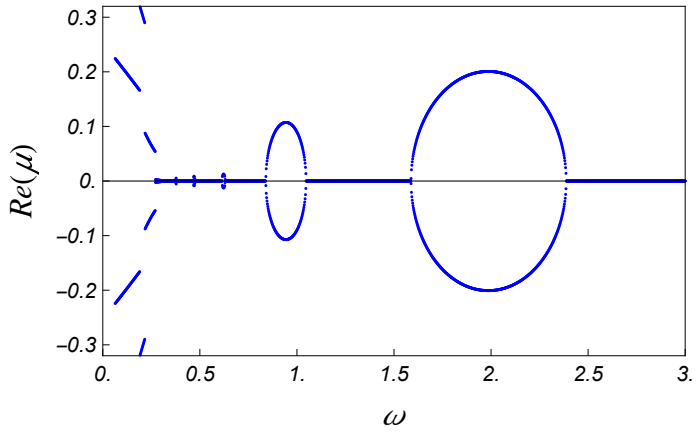


Figure 4.6: Growth factor for $c_0 = 0, c_1 = 0.8$ and $\gamma = 0.5$ when $n = 6$.

applied to the following system with two-harmonic periodic damping:

$$\ddot{x} + (c_0 + c_1 \cos \omega t + \gamma c_1 \cos(2\omega t + \phi))\dot{x} + x = 0. \tag{4.18}$$

We perform the same steps as before for Eqn. (4.18), when $\phi = 0$, $c_0 = 0$ and $c_1 = 0.8$. Considering a similar truncated approximate solution as Eqn. (4.9) leads to matrix $\mathbf{D}(\mu)\mathbf{a}$, which $\mathbf{D}(\mu)$ is obviously different than $\mathbf{K}(\mu)$. We then find eigenvalues ($\mu$), as well as eigenvectors ($\mathbf{a}$), and the principal roots as described before. Figure 4.6 indicates how the real part of the principal root varies with $\omega$ and Fig. 4.7 shows the frequencies of the response for $n = 6$. In Fig. 4.8 the boundaries of stability for $\gamma = 0.5$ and $n = 6$ are plotted. This figure loses fidelity for $\omega < 0.5$. The single-harmonic damping system is known to demonstrate coexistence, for which the sides of a stability wedge overlap, closing the wedge. This was captured previously near $\omega = 1$ and $\omega = \frac{1}{2}$ [6, 39]. Two-harmonic damping "opens up" the coexistence into finite instability wedges, most notably with the prominent wedge at $\omega = 1$ (see Fig. 4.7).

## 4.5 Conclusion

Parametric excitation has been of much interest in mechanical systems. In this work we focused on the parametrically excited systems with two-harmonic parametric excitations. The purpose of the work was to determine not only the stability regions but also the

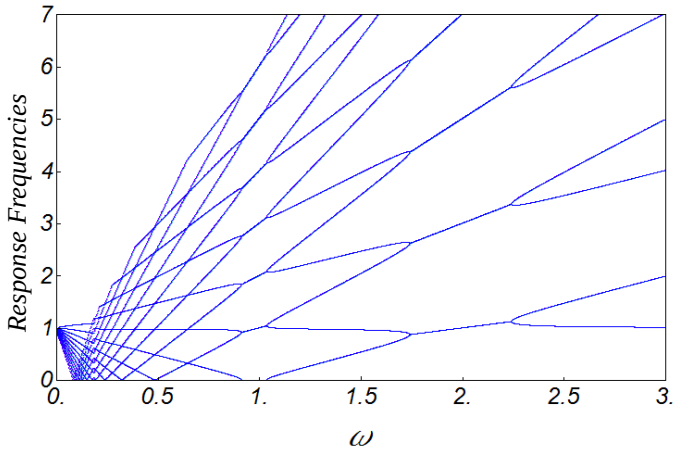


Figure 4.7: Response frequency for $c_0 = 0, c_1 = 0.8$ and $\gamma = 0.5$ when $n = 6$.

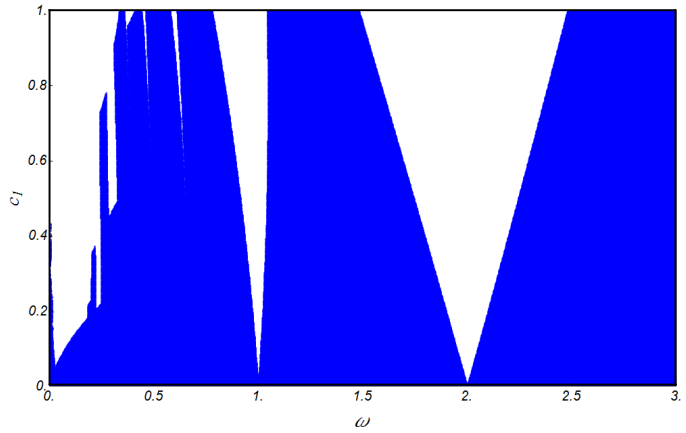


Figure 4.8: Stability boundaries for $c_0 = 0$ and $\gamma = 0.5$ when $n = 6$.

characteristics of the responses.

We used the Floquet theory combined with harmonic balance to analyze our system. The approximated solution is composed of an exponential part and a truncated Fourier series. The Floquet exponents and the Fourier coefficients are unknown and determined by solving an EVP derived from the second-order differential equation.

By extracting the Floquet exponents we obtained information about the stability criteria and the relationship between the excitation frequency and the frequencies of the response.

Moreover, putting Fourier coefficients into the approximated solution for certain initial conditions demonstrated the time response of the system, and theoretical results for initial condition responses were evaluated favorably with the numerical analysis.

Comparing analysis of two-harmonic Mathieu with standard Mathieu showed that the boundaries of the subharmonic instability do not change visibly. However, the primary and superharmonic wedges can have a remarkable change, either shrinking or enlarging, depending on the phase of the second harmonic of excitation. By increasing the truncation order we captured more stability tongues for lower values of frequency. Stability diagrams as well as the response frequencies for two different truncation numbers indicated the influence of the order of truncation. The range of accuracy increases as the truncation $n$ increases. There may be a computational limit on $n$, however.

We applied the truncated Floquet series expansion to a system with two-harmonic parametric damping and observed that the coexistence in single-harmonic parametric damping turns into a tongue of instability when a second harmonic is added, for the parameters studied.

Ongoing work includes more study of the effect of relative amplitude and phase of the second harmonic, and more details on the effect of multiple harmonics in systems with parametric damping. Studying a third harmonic ($3\omega$) of excitation in place of the $2\omega$ term may also make sense for physical applications.

# CHAPTER 5

## RESPONSE CHARACTERISTICS OF SYSTEMS WITH PARAMETRIC EXCITATION THROUGH DAMPING AND STIFFNESS

Reduced-order models of the vibration of horizontal-axis wind turbines (HAWTs) [11, 46, 83] have often made use of a forced Mathieu-Hill equation, which may include damping, such that the equation has the form

$$\ddot{x} + 2\zeta\dot{x} + f(t)x = g(t), \tag{5.1}$$

where $f(t)$ and $g(t)$ are periodic. Basic models of vertical-axis wind turbines (VAWTs) with aeroelastic force can be represented by oscillators with stiffness and cyclic damping [9], such as

$$\ddot{x} + 2\zeta h(t)\dot{x} + x = g(t) \tag{5.2}$$

in a nondimensional form. Ince's equation describes systems with cyclic inertia, damping and stiffness[88]:

$$(1 + a\cos\omega t)\ddot{x} + b\sin\omega t\dot{x} + (c + d\cos\omega t)x = 0. \tag{5.3}$$

Tower shadowing in HAWTs or the aerodynamics in spinning VAWTs may induce cyclic fluctuations in both damping and stiffness terms. Several methods have been used to study parametrically excited systems. The damped and undamped Mathieu's equation is the most thoroughly studied parametrically excited system.

Taylor and Narendra studied the stability boundaries of the damped Mathieu equation by using a perturbation method [105]. Rand et al. [86] approximated the stability regions of systems with quasiperiodic stiffness using four different methods: numerical integration, Lyapunov exponents, regular perturbation and harmonic balance. In [61, 75, 86, 88] Rand and his colleagues discussed the phenomena called "coexistence" in Ince's equation, and Recktenwald and Rand [89] studied the generalization of results obtained previously when

applied to the generalized Ince's equation. Sofroniou and Bishop[99] investigated the dynamics of parametrically excited systems with two forcing terms.

Superposition is not applicable in studying systems with parametric excitation. Therefore various combinations of the cyclic excitation cannot be obtained from individual studies of cyclic stiffness and cyclic damping, and must be analyzed specifically. In this work, we focus on the Eq. (5.3), when $a = 0$. In such case it becomes a system with a combination of parametric damping and stiffness. We study this system using an analysis based on Floquet theory. We aim to uncover how the cyclic stiffness and damping combine and together affect the initial conditions responses and stability.

## 5.1 Analysis

Generally the Floquet theory can be applied on systems which have the state-variable form

$$\dot{\mathbf{x}} = \mathbf{A}(t)\mathbf{x}, \tag{5.4}$$

in which $\mathbf{x}$ is an $N \times 1$ state vector and $\mathbf{A}(t)$ is $N \times N$ and is periodic with period $T$. According to Floquet theory [112], solutions of Eq. (5.4) have the form $\mathbf{x}_i(t) = e^{\mu_i t}\mathbf{p}_i(t)$, $i = 1, ..., N$, where $\mathbf{p}_i(t)$ has period $T$ and the Floquet exponents, $\mu_i$, satisfy

$$e^{\mu_1 T} e^{\mu_2 T} \cdots e^{\mu_N T} = exp(\int_0^T tr(\mathbf{A}(s))ds). \tag{5.5}$$

Floquet properties imply that the characteristic exponents are not unique since, if $\rho_j = e^{\mu_j T}$, then $\rho_j = e^{(\mu_j + \frac{2\pi i}{T})T}$. Floquet theory states that there exist $N$ number of unique Floquet exponents, called principal roots, which $N$ is the number of the state space. Floquet analysis also provides a relation between the principal roots.

We will show the details of the analysis for the case of Eq. (5.3) To this end, we consider an equation with combined parametric excitation of the form

$$\ddot{x} + (c_0 + c_1 \cos(\omega t + \phi))\dot{x} + (k_0 + k_1 \cos \omega t)x = 0, \tag{5.6}$$

when the system experiences parametric excitation through both damping and stiffness terms. We sought an approximate solution based on Floquet theory following the approach in [3, 6]. The equation in state-space form is

$$\begin{aligned}\dot{\mathbf{x}} &= \begin{pmatrix} \dot{x} \\ \ddot{x} \end{pmatrix} = \begin{bmatrix} 0 & 1 \\ -(k_0 + k_1 \cos\omega t) & -(c_0 + c_1 \cos(\omega t + \phi)) \end{bmatrix} \begin{pmatrix} x \\ \dot{x} \end{pmatrix} \\ &= \mathbf{A}(t)\mathbf{x}, \end{aligned} \tag{5.7}$$

where $\mathbf{A}(t)$ is a periodic matrix with period $\frac{2\pi}{\omega}$. We seek a solution of the form $x = e^{\mu t} p(t)$. Using a truncated series approximation, the approximate response is

$$x(t) \cong e^{\mu t} \sum_{j=-n}^{+n} a_j e^{ij\omega t}, \tag{5.8}$$

where $\mu$ is the Floquet exponent and $a_j$'s are Fourier coefficients. $Im(\mu)$ is combined with the excitation frequency to build the response frequency. Substituting the approximated solution into Eq. (5.6), and then applying harmonic balance on the coefficients of the $e^{ij\omega t}$, generates an equation of the form

$$\mathbf{K}(\mu)\mathbf{a} = 0, \tag{5.9}$$

where $\mathbf{K}$ is the matrix of the coefficients.

## 5.2 Application to System with Combined Parametric Excitation

### 5.2.1 Analysis of the Truncated Solution

When $n = 2$, Eq. (5.9) takes the form

$$\begin{bmatrix} B_{-2} & D_{-1} & 0 & 0 & 0 \\ E_{-2} & B_{-1} & D_0 & 0 & 0 \\ 0 & E_{-1} & B_0 & D_1 & 0 \\ 0 & 0 & E_0 & B_1 & D_2 \\ 0 & 0 & 0 & E_1 & B_2 \end{bmatrix} \begin{pmatrix} a_{-2} \\ a_{-1} \\ a_0 \\ a_1 \\ a_2 \end{pmatrix} = \begin{pmatrix} 0 \\ 0 \\ 0 \\ 0 \\ 0 \end{pmatrix}, \tag{5.10}$$

where $B_i$, $D_i$, and $E_i$ are functions of the Floquet multiplier, damping and stiffness parameters and frequency (Appendix A). Equation (5.10) is essentially an eigenvalue

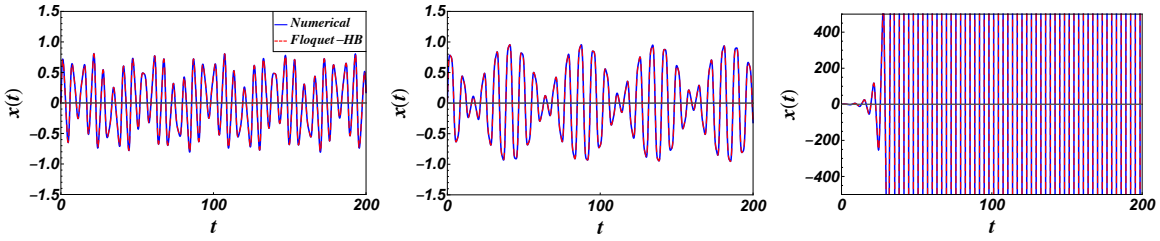


(a) $\omega = 1.1$ (b) $\omega = 1.48$ (c) $\omega = 2$

Figure 5.1: Time response when $k_0 = 1$, $k_1 = 1$, $c_0 = 0$, $c_1 = 0.1$, $\phi = 0$ and $n = 4$. (Three different frequencies, $\omega = 1.1$,$\omega = 1.48$ and $\omega = 2$).

problem (EVP). Obtaining a nonzero solution for Fourier coefficients, $a_j$s, requires that $|\mathbf{K}(\mu)| = 0$. Setting the determinant equals zero yields to the characteristic equation for $\mu$, a $(2n + 1)$th degree polynomial in $\mu^2$ which provides $(4n + 2)$ solutions for $\mu$. Based on Floquet theory there exist only two distinct roots referred as principal roots. Following this theory [112],

$$e^{(\mu_1+\mu_2)T} = exp(\int_0^T tr(\mathbf{A}(s))ds). \tag{5.11}$$

From Eq. (5.7), $Tr(\mathbf{A}) = -(c_0 + c_1 \cos \omega t)$. Therefore, Eq. (5.5) reduces to $(\mu_1 + \mu_2)T = -c_0 T \pm 2\pi i k$, where $k$ is integer. $T = \frac{2\pi}{\omega}$ leads to the criterion

$$\mu_1 + \mu_2 = -c_0 \pm k\omega i. \tag{5.12}$$

This formula is applied to obtain the principal roots. Fourier coefficients, $a_j^i$, are associated with the roots, $\mu_i$ $(i = 1, 2)$, and are determined by Eq. (5.10).

## 5.3 Results

### 5.3.1 Response Analysis

#### 5.3.1.1 Time Response.

$\mu = \mu_i$ and $a_j = a_j^{(i)}$, $i = 1, 2$ are inserted into Eq. (5.8), which produces two principal independent solutions, $x_i(t)$. The general solution to the second order differential equations is

$$x(t) = C_1 x_1(t) + C_2 x_2(t). \tag{5.13}$$

Plugging Eq. (5.8) into Eq. (5.13), the system has a solution of the form

$$
\begin{aligned}
& x(t) = \\
& C_1 e^{\mu_1 t}\left(a_{-n}e^{-nit\omega}... + a_{-1}e^{-it\omega} + a_0 + a_1 e^{it\omega}... + a_n e^{nit\omega}\right) \\
& +C_2 e^{\mu_2 t}\left(a_n e^{-nit\omega}... + a_1 e^{-it\omega} + a_0 + a_{-1}e^{it\omega}... + a_{-n}e^{nit\omega}\right)
\end{aligned}
\tag{5.14}
$$

$C_1$ and $C_2$ are determined by the initial conditions. In this example $x(0) = 0$ and $\dot{x}(0) = 1$. $\mu_1$ and $\mu_2$ in Eq. (5.14) are the Floquet multipliers found by solving the EVP (Eq. 5.10). We then are able to find the time response of the system by setting the parameters. For different sets of parameters the response of the system is either stable with quasi-periodic behavior, or unstable and unbounded. The system could also sit in the vicinity of the stability boundaries where the response is floating between the stable and unstable zone. Figure 5.1 shows the results of the system for different sets of parameters when Floquet method combined with harmonic balance (Floquet-HB) is applied and the responses are compared with the numerical time responses. For four number of truncation the responses obtained by Floquet-HB are in agreement with the numerical results. Figure 5.1a shows that the system is stable and has a quasi-periodic response for $\omega = 1.1$, while in Fig. 5.1b, $\omega = 1.48$ and response of the system is near a boundary of stability. In next section it can be seen and explained that the frequencies of harmonics are slightly different such that the "beating phenomenon" occurs. Figure 5.1c shows that the system is unstable where $\omega = 2$. Later we will see the stability boundaries and the zones of stability for varying frequencies of excitation.

#### 5.3.1.2 Response Frequencies.

Equation (5.14) provides significant information about the response of the system. The equation indicates that the frequency of the response is a combination of the imaginary part of the Floquet exponent (Fig. 5.2) and the oscillating part, $\omega_j = Im(\mu) \pm j\omega$, where

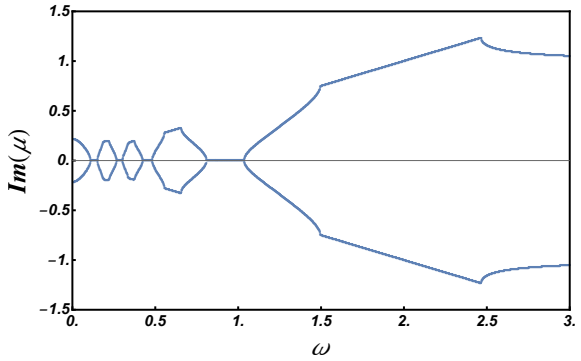


Figure 5.2: Imaginary of growth/decay factor when $k_0 = 1$, $k_1 = 1$, $c_0 = 0$, $c_1 = 0.1$ and $n = 4$.

$j = 0, 1, 2, ..., n$. In Fig. 5.3 the frequencies of the response for $k_0 = 1$, $k_1 = 1$, $c_0 = 0$ and $c_1 = 0.1$ are shown when the truncation order is $n = 4$. Increasing the number of truncation increases the accuracy and the number of branches in the frequency response analysis.

#### 5.3.1.3 Growth/Decay Factor.

As noted before equation (5.14) tells important feature of the response of the system. Referring to Eq. (5.14), the response of the system is governed by the real part of the Floquet exponent ($Re(\mu_i)$). It is easily perceived that for $Re(\mu_i) < 0$ response stays stable and for any $Re(\mu_i) > 0$ response goes unstable. Figure 5.4 demonstrates the growth or decay factor of the response when $k_0 = 1$, $k_1 = 1$, $c_0 = 0$ and $c_1 = 0.1$. The unstable zone is identified with the bubbles when the associated Floquet multipliers have at least one positive $Re(\mu)$.

### 5.3.2 Stability Analysis

As noted, stability diagrams describe the regions of stability where the system stays stable with periodic or quasi-periodic response for pairs of parameters. Here the parameters are $c_1$, the damping amplitude, versus $\omega$, the excitation frequency (Fig. 5.5). Figure 5.5 represents the zones of stability for $n = 4$, where the blue and white zones are associated with the stable and unstable response, respectively. Comparing with the system with

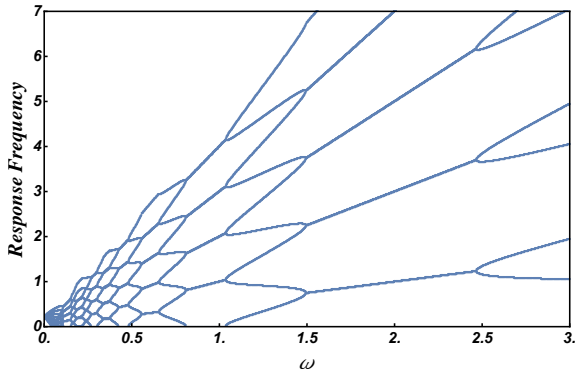


Figure 5.3: Response frequencies when $k_0 = 1$, $k_1 = 1$, $c_0 = 0$, $c_1 = 0.1$ and $n = 4$.

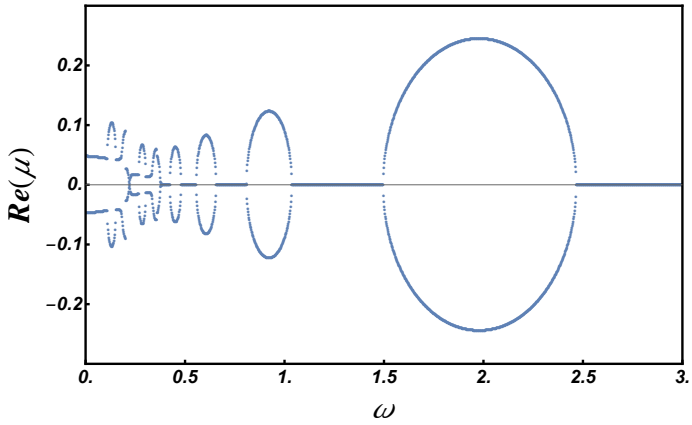


Figure 5.4: Real of growth/decay factor when $k_0 = 1$, $k_1 = 1$, $c_0 = 0$, $c_1 = 0.1$ and $n = 4$.

parametric stiffness (Mathieu's equation) (Fig. 5.5a) the subharmonic wedge (near $\omega = 2$) and the primary ($\omega = 1$) wedge has been clearly distorted. Figure 5.5b shows the stability wedges and demonstrates how adding the parametric stiffness to the system affects the subharmonic, superharmonic and primary instability wedges when the wedges open and the boundaries of stability become smaller. Referring to Fig. 5.3, in regions of stability the truncated expansion represents $2n + 1$ of the response frequencies. In the transition from the stable to unstable region, repeated frequencies occur which in the response frequency analysis comes into sight when two branches merge into one with repeated values of $\omega/2, 3\omega/2, ..., (2n+1)\omega/2$ response frequencies. The relative parametric excitation phase $\phi$ can affect stability. A phase shift of $\phi = \frac{\pi}{2}$ in the damping turns the $\cos \omega t$ to $\sin \omega t$. In

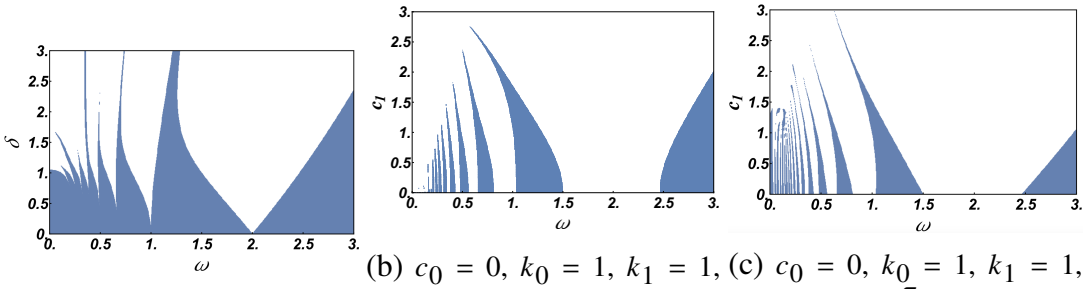


(a) Mathieu's equation ($n = 4$) $n = 8$ and $\phi = 0$

(b) $c_0 = 0$, $k_0 = 1$, $k_1 = 1$, $n = 8$ and $\phi = \frac{\pi}{2}$

Figure 5.5: Stability boundaries.

this case the Eq. (5.6) turns into

$$\ddot{x} + (c_0 + c_1 \sin \omega t)\dot{x} + (k_0 + k_1 \cos \omega t)x = 0 \tag{5.15}$$

when $c_0 = 0$, it represents a special case of the Ince's equation (Eq. (5.3) for $a = 0$). Comparing Fig. 5.5b and Fig. 5.5c demonstrates the effect of the phase shift on the stability diagrams and it can be shown that the boundaries of stability becomes narrower.

When $c_0 = 0$, $k_0 = 1$, $c_1 = k_1 = \delta$, Eq. (5.6) becomes

$$\ddot{x} + (\delta \sin \omega t)\dot{x} + (1 + \delta \cos \omega t)x = 0 \tag{5.16}$$

Figure 5.6a shows the stability wedges when system involves equivalent parametric stiffness

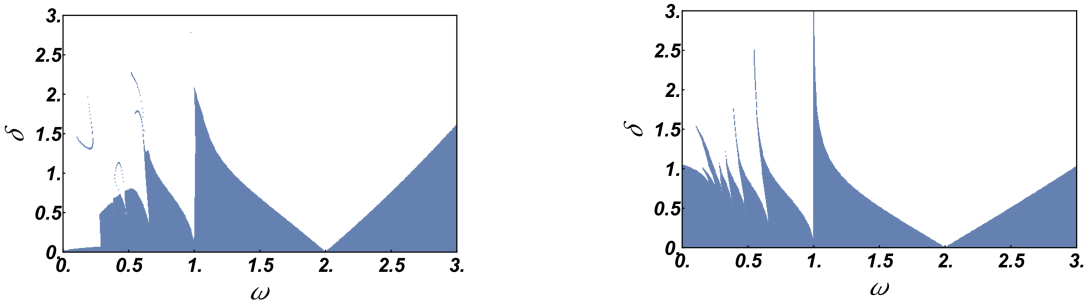


(a) $c_0 = 0$, $k_0 = 1$, $k_1 = 1$ AND $\phi = 0$

(b) $c_0 = 0$, $k_0 = 1$, $k_1 = 1$ AND $\phi = \frac{\pi}{2}$

Figure 5.6: Stability boundaries for $c_0 = 0$, $k_0 = 1$, $c_1 = k_1 = \delta$, and $n = 4$.

and damping effect and there is not a phase shift ($\phi = 0$). Adding a 90 degrees phase shift to the parametric damping effects the stability boundaries as shown in Fig. 5.6b.

## 5.4 Conclusion

Parametric excitation has been of much interest in mechanical systems. In this work we focused on the parametrically excited systems with a combination of the parametric damping and parametric stiffness. The purpose of the work was to study the interaction of the parametric terms in the dynamical system. We aimed to determine the characteristics of the responses and their stability.

We use the Floquet theory combined with harmonic balance to analyze our system. The approximated solution is composed of an exponential part and a truncated Fourier series. The Floquet exponents and the Fourier coefficients are determined solving an eigenvalue problem derived from the second-order differential equation.

By extracting the Floquet exponents we obtained the stability criteria and the relationship between the excitation frequency and the frequencies of the response. Moreover, putting Fourier coefficients into the approximated solution for certain initial conditions demonstrated the time response of the system. Theoretical results for initial condition responses were evaluated favorably with the numerical analysis.

Comparing analysis of combined parametric excitation with parametric damping excitation showed that the boundaries of the subharmonic, primary and superharmonic wedges experience a notable change, either shrinking or enlarging.

Studying the Ince's equation with parametric damping and constant stiffness introduced a phenomenon called "coexistence". We applied the truncated Floquet series expansion to a system with combined parametric excitation in both damping and stiffness and observed that the coexistence in parametric damping turns into a tongue of instability when parametric stiffness harmonic is added to the equation.

Ongoing work includes more study of the effect of relative amplitude and phase of the parametric terms, and details on the effect of increasing the order of truncation. Studying different combination of the damping and stiffness for example constant mean damping

with varying mean stiffness, may also make sense to be studied for physical applications.

# CHAPTER 6

## RESONANCES OF A FORCED VAN DER POL EQUATION WITH PARAMETRIC DAMPING

In this paper we study the responses of an oscillator with van der Pol terms, parametric damping and direct excitation. A potential application of this system is a vertical-axis wind-turbine blade, which can endure direct excitation and parametric damping [5, 7], as well as aeroelastic self-excitation, the mechanism of which can be loosely modeled with van-der-Pol-type nonlinearity [73, 88]. Here, the general behavior of this system is studied, rather than the specific responses of a specific model of an application system. As both parametric excitation and van-der-Pol nonlinearity can induce instabilities and oscillations, we seek to understand the combined effect of such terms in this system.

The nonlinear damping in the van-der-Pol equation [73, 88], originally introduced to model electrical oscillations [109], is well known to induce limit-cycle oscillations. Holmes and Rand [40] studied the bifurcation of the variational equation of the forced van der Pol oscillator. Barbosa et al. [15] studied the modified version of the classical van der Pol oscillator containing derivatives of fractional order. They applied approximations to fractional-order operators to show the dynamics of the model through numerical simulations [15].

Parametric excitation generally induces significant behavior in dynamical systems. For this reason studying systems with parametric excitation has been of keen interest, typically in the context of parametric stiffness, specifically the Mathieu equation [73, 88, 112].

Parametric damping has been shown to generate instabilities [7, 38], similar to those of the Mathieu equation [73, 88], with period-1 or period-2 oscillation, and to decay with quasiperiodic dynamics when stable [7]. The study [7] used the Floquet solution combined with harmonic balance [2, 8]. Studies on related systems, combining parametric and/or direct excitation with nonlinearity, include parametric stiffness and damping [8], nonlinear Mathieu systems [69, 74, 110] with forcing [36, 46, 85, 90], Mathieu-van-der-Pol [34], and

a forced Mathieu-van-der-Pol-Duffing system [80].

Additionally, Rhoads et al. [92] studied the dynamic response of microelectromechanical (MEM) oscillators. They focused on particular systems with parametric excitation that arises from forces produced by fluctuating voltages applied across comb drives.

Szabelski and Warminski [104] performed an analytical examinations on the system with three sources of vibration, parametric, self-excited and inertial. Warminski [113] studied the nonlinear dynamics of a self, parametric, and externally excited oscillator with time delay analytically applying the method of multiple scales. Warminski also discussed the similarities and differences between the van der Pol and Rayleigh for regular, periodic, quasi-periodic and chaotic oscillations.

Parametric excitation has also been studied in the context of wind turbine blades [1, 12, 46, 85]. Luongo and Zulli [60] studied a self-excited tower under turbulent wind flow. The tower was assumed to be a nonlinear system where the stationary wind imposed the self excitation and the turbulent flow drove both parametric and external excitation. Combining parametric damping with self-excitation of nonlinear damping as in a van der Pol equation, with a particular choice of scaling and excitation frequencies, results in an equation given as

$$\ddot{x} + \epsilon(c_0 + c_1 \cos \omega t + x^2)\dot{x} + {\omega_n}^2 x = f_0 + f_1 \sin(\omega t), \tag{6.1}$$

where $\epsilon \ll 1$. The variables $c_0$ and $c_1$ are the mean damping and amplitude of the parametric damping, respectively, and $f_0$ and $f_1$ are mean and cyclic direct excitation amplitudes. The excitation frequency is $\omega$ and the natural frequency is $\omega_n$. We will refer to this as the parametrically damped van der Pol (PDVDP) equation with external excitation.

In this work, we apply the first-order method of multiple scales [72, 73] to study an unforced and externally forced van der Pol equation with parametric damping at frequency $\omega$. We study the sub-harmonic resonance of order $1/2$ as well as the nonresonant dynamics.

## 6.1 Perturbation Analysis: Method of Multiple-Scales

The core of this study is the approximation of the solution to Eqn. (6.1) based on the method of multiple scale (MMS) [73, 88]. Therefore, we expand the displacement as

$$x(T_0, T_1, \cdots) = x_0(T_0, T_1, \cdots) + \epsilon x_1(T_0, T_1, \cdots) + \epsilon^2 x_2(T_0, T_1, \cdots) + \cdots, \tag{6.2}$$

where the time scales are $T_i = \epsilon^i t$, and $\epsilon \ll 1$. By using the chain rule, we obtain the derivatives for $n \in \mathbb{N}$ as $\frac{d^n}{dt^n}(\cdot) = (D_0 + \epsilon D_1 + \epsilon^2 D_2 + \cdots)^n(\cdot)$ , where $D_i = \frac{\partial}{\partial T_i}$. Here, we carry out the analysis up to the first order by considering the two time scales, $T_0 = t$ and $T_1 = \epsilon t$, and therefore expand the displacement as

$$x(T_0, T_1) \approx x_0(T_0, T_1) + \epsilon x_1(T_0, T_1). \tag{6.3}$$

By substituting the expansion (6.3) in Eqn. (6.1) and using the derivatives, coefficients of similar powers of $\epsilon$ equate as

$$\epsilon^0 : \quad {D_0}^2 x_0 + {w_n}^2 x_0 = f_0 + f_1 \sin(\omega t), \tag{6.4}$$

$$\epsilon^1 : \quad {D_0}^2 x_1 + {w_n}^2 x_1 = -2 D_0 D_1 x_0 - (c_0 + c_1 \cos \omega T_0 + {x_0}^2)(D_0 x_0). \tag{6.5}$$

The relationship between the excitation and the natural frequencies specifies different cases of resonance:

1. Nonresonant: no specific relationship between $\omega$ and $\omega_n$
2. Primary resonance: $\omega \approx \omega_n$
3. Super-harmonic resonance: $\omega \approx \omega_n / m$ $(m \in \mathbb{N})$
4. Sub-harmonic resonance: $\omega \approx m\omega_n$ $(m \in \mathbb{N})$

In the next sections, we elaborate on this perturbation analysis for specific cases with and without external excitation, and apply other tools, to examine the dynamics with emphasis on secondary resonances.

## 6.2 Parametric Excitation without External Excitation

We start with the case where there is no external forcing, i.e. $f_0 = f_1 = 0$. As a survey of the possible dynamics, Fig. 6.1 shows a frequency sweep from $\omega = 0$ to beyond $\omega = 2\omega_n$, when $\omega_n = 1$, $\epsilon = 0.1$, $c_0 = -1$, and $c_1 = 1$ (these parameters are dimensionless). The sweep, as a bifurcation diagram, is a plot of samples of the $x$ variable of the nonwandering set in a Poincaré section [35] for various values of the frequency parameter. A Runge-Kutta method (Matlab ode45) is used to obtain numerical solutions of several periods to achieve steady state. As the responses are typically quasi-periodic, the plots are generated by recording at each excitation frequency, 50 values of $x$ at the downward $\dot{x} = 0$ crossing in the phase space.

The plot shows that significant quasi-periodic dynamics occur for a large range of excitation frequencies, with a periodic window around $\omega \approx 2\omega_n$. The largest responses occur near this subharmonic range, as well as for low frequencies. Super harmonic and primary resonances are not apparent, beyond a possible frequency interval of periodic or nearly periodic dynamics. Figure 6.2 shows example of quasi-periodic responses for three different excitation frequencies.

We appeal to perturbation analysis to explain these responses. The solution to the leading order Eqn. (6.4) is

$$x_0(T_0, T_1) = A(T_1)e^{i\omega_n T_0} + \text{c.c.}, \tag{6.6}$$

where c.c. stands for the corresponding complex conjugate terms. We obtain the solvability conditions by substituting Eqn. (6.6) into the right hand side of Eqn. (6.5) and eliminating the "secular terms". In MMS, the secular terms are defined as the terms that make the solution to grow without bound in time, and thus should be eliminated. By plugging Eqn. (6.6) into Eqn. (6.5), we obtain

$$\begin{aligned} {D_0}^2 x_1 + {w_n}^2 x_1 &= (-2i\omega_n A' - ic_0\omega_n A - i\omega_n A^2 \bar{A})e^{i\omega_n T_0} \\ &\quad -\frac{c_1}{2}\left(i\omega_n \bar{A} e^{i(\omega-\omega_n)T_0}\right) + \text{N.S.T.}, \end{aligned} \tag{6.7}$$

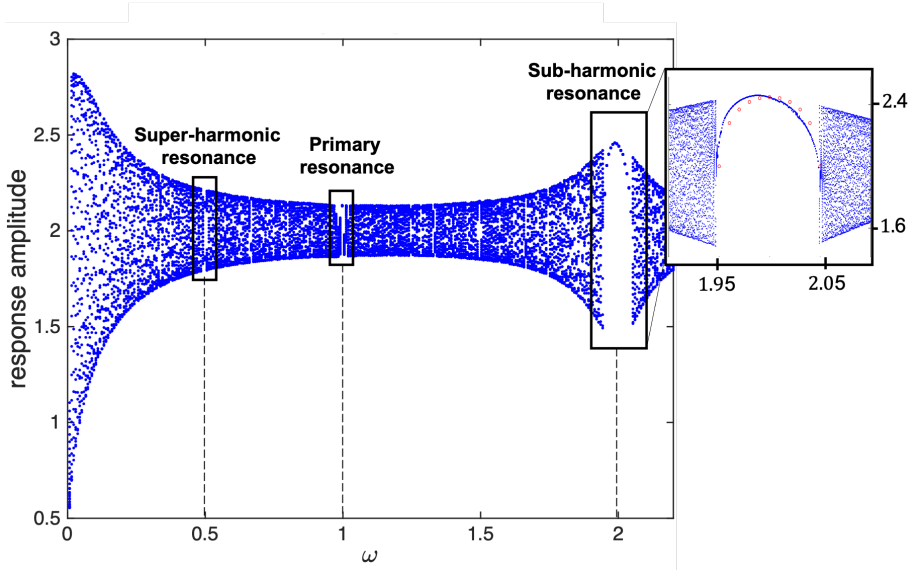


Figure 6.1: PDVDP with parametric excitation only. The response amplitude versus the excitation frequency when $f_0 = f_1 = 0, \omega_n = 1, \epsilon = 0.1, c_0 = -1$ and $c_1 = 1$ . The embedded sub-plot zooms in on the strong sub-harmonic resonance window. The circles are amplitudes predicted by the perturbation analysis.

where N.S.T stands for non-secular terms and $A' = D_1 A$. The homogeneous solution of Eqn. (6.7) is of the form $e^{i\omega_n T_0}$ and therefore any right-hand-side term that is of the same form will become secular and cause $x_1$ to grow without bound. We seek the resonance cases that lead to additional secular terms. The right-hand-side of Eqn. (6.7) merely shows the sub-harmonic resonance case. However, as shown in Fig. 6.1 as well as Eqn. (6.7), the system has significant oscillatory behavior at the nonresonant case, that is when there is no specific relationship between the excitation frequency $\omega$ and the natural frequency $\omega_n$.

• Nonresonant: $$2A' + c_0 A + A^2 \bar{A} = 0$$

• Sub-harmonic Resonance of Order 1/2 ($\omega = 2\omega_n$):

$$2A' + c_0 A + A^2 \bar{A} - \frac{c_1}{2} \bar{A} e^{i\sigma T_1} = 0 \tag{6.8}$$

### 6.2.1 Nonresonant Case

We first consider the nonresonant case, where the solvability condition takes the form $2A' + c_0 A + A^2\bar{A} = 0$. We recall that $A$ is a complex function of $T_1$. Writing it as $A(T_1) = \frac{1}{2}a(T_1)e^{i\beta(T_1)}$, the solvability condition becomes

$$a' + ia\beta' + \frac{1}{2}c_0 a + \frac{1}{8}a^3 = 0. \tag{6.9}$$

By separating the real and imaginary parts, we obtain the following governing equations of amplitude $a$ and phase $\beta$ as

$$a' + \frac{1}{2}c_0 a + \frac{1}{8}a^3 = 0, \quad a\beta' = 0. \tag{6.10}$$

The response amplitude has steady-state values that depend on the parameter $c_0$ and are obtained by setting $a' = 0$. When $c_0 < 0$, there is a stable steady-state amplitude of $a = 2\sqrt{|c_0|}$. This amplitude, and the solvability condition that leads to it, are the same as in the regular van der Pol equation when $c_0 = -1$.

Having eliminated the solvability condition, we keep the remaining terms in Eqn. (6.7), and find the particular solution to be

$$x_1 = Q_1 e^{3i\omega_n T_0} + Q_2 e^{i(\omega+\omega_n)T_0} + Q_3 e^{i(\omega_n-\omega)T_0}, \tag{6.11}$$

where

$$Q_1 = \frac{iA^3}{8\omega_n}, \quad Q_2 = \frac{c_1 i\omega_n A}{2\omega(\omega+2\omega_n)}, \quad Q_3 = \frac{c_1 i\omega_n A}{2\omega(\omega-2\omega_n)}, \tag{6.12}$$

and where $A = \frac{1}{2}ae^{i\beta}$. Eqn. (6.11) is valid if $\omega \neq 2\omega_n$. Then the leading-order nonresonant solution is

$$\begin{aligned} x &= x_0 + \epsilon x_1 \\ &= a\cos(\omega_n T_0 + \beta) + \epsilon(2Q_1\cos(3\omega_n T_0) + 2Q_2\cos(\omega+\omega_n)T_0 + 2Q_3\cos(\omega-\omega_n)T_0). \end{aligned} \tag{6.13}$$

This demonstrates, for the nonresonant case, a uniformly present oscillation term at the amplitude $a$, which comes from the van der Pol element, plus small oscillatory parametric

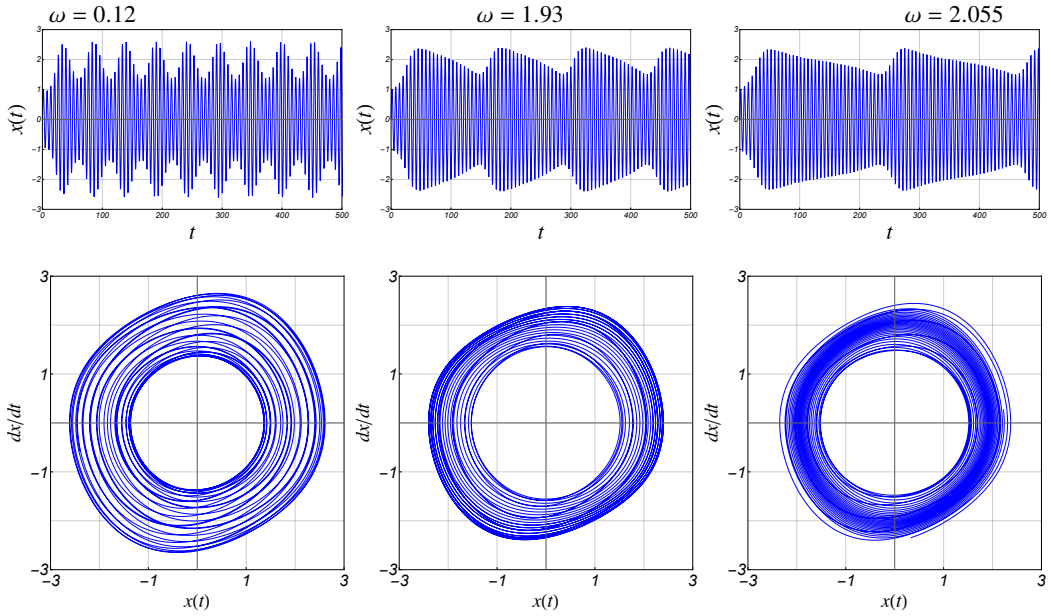


Figure 6.2: PDVDP with parametric excitation only: Time response (top row) and phase portrait (bottom row) at different excitation frequencies where $f_0 = f_1 = 0, \omega_n = 1, \epsilon = 0.1, c_0 = -1$ and $c_1 = 1$.

terms with frequency-dependent amplitudes, and with two independent frequencies, such that in typical cases the result is quasi-periodic.

The numerical solutions in Fig. 6.2 have features described by the nonresonant case. When $\omega = 0.12$, the response looks like classic beating that can arise with the sum of two incommenserate, simple harmonics. This is consistent with the approximate solution in Eqn. (6.13). The cases of $\omega = 1.93$ and $\omega = 2.055$ provide bookends around the subharmonic resonance formulated in the next section. While the two latter cases seem to have features of the nonresonant solution, we will see that the subharmonic resonance analysis describes them more accurately.

### 6.2.2 Sub-harmonic Resonance of Order 1/2.

Here, we focus on the sub-harmonic resonance case, where the excitation frequency is tuned to be close to the double natural frequency, i.e. $\omega = 2\omega_n + \epsilon\sigma$. In this setting, the solvability condition is comprised of more terms and is given as $2A' + c_0 A + A^2\bar{A} - \frac{c_1}{2}\bar{A}e^{i\sigma T_1} = 0$.

By letting $A(T_1) = \frac{1}{2}a(T_1)e^{i\beta(T_1)}$, we obtain

$$a' + ia\beta' + \frac{1}{2}c_0 a + \frac{1}{8}a^3 - \frac{1}{4}c_1 a e^{i(\sigma T_1 - 2\beta)} = 0. \tag{6.14}$$

We separate the real and imaginary parts and then make the system autonomous via the change of variables $\gamma = \sigma T_1 - 2\beta$ to obtain the following governing equations of amplitude $a$ and phase $\gamma$ as

$$\begin{aligned} \text{Re}: \quad & a' + \frac{1}{2}c_0 a + \frac{1}{8}a^3 - \frac{1}{4}c_1 a\cos(\sigma T_1 - 2\beta) = 0, \\ \text{Im}: \quad & a\beta' - \frac{1}{4}c_1 a\sin(\sigma T_1 - 2\beta) = 0. \end{aligned} \tag{6.15}$$

To investigate the dynamics of Eqn. (6.15), we first make the system autonomous via the change of variable $\gamma = \sigma T_1 - 2\beta$ to obtain

$$a' + \frac{1}{2}c_0 a + \frac{1}{8}a^3 - \frac{1}{4}c_1 a\cos\gamma = 0, \quad a\gamma' + \frac{1}{2}c_1 a\sin\gamma - \sigma a = 0. \tag{6.16}$$

The response amplitude has steady-state values that depend on the parameters $c_0$ and $c_1$ and are obtained by setting $a' = \gamma' = 0$. By using the trigonometric identities, we remove $\gamma$ and finally obtain the response amplitude as

$$a = 0, \quad \text{or} \quad a^2 = -4c_0 \pm 4\sqrt{\frac{c_1^2}{4} - \sigma^2}. \tag{6.17}$$

If $\frac{c_1^2}{4} - \sigma^2 > 0$, then Eqn. (6.17) indicates that there are both zero and non-zero real-valued response amplitudes. Otherwise, the only steady-state amplitude is zero. Stability of these solutions is determined from the Jacobian of Eqns. (6.16).

Figure 6.3 shows the steady-state amplitude versus the excitation frequency $\omega = 2\omega_n + \epsilon\sigma$ for different values of $c_0$ and $c_1$ where $\epsilon = 0.1$ and $\omega_n = 1$. By slightly sweeping the detuning parameter $\sigma$, we keep the excitation frequency $\omega$ close to $2\omega_n$. We observe the emergence of a limit cycle at $\omega \approx 1.95$, whose amplitude grows and then disappears at $\omega \approx 2.05$. When $c_0 = -1$, a larger amplitude of parametric damping $c_1$ leads to a

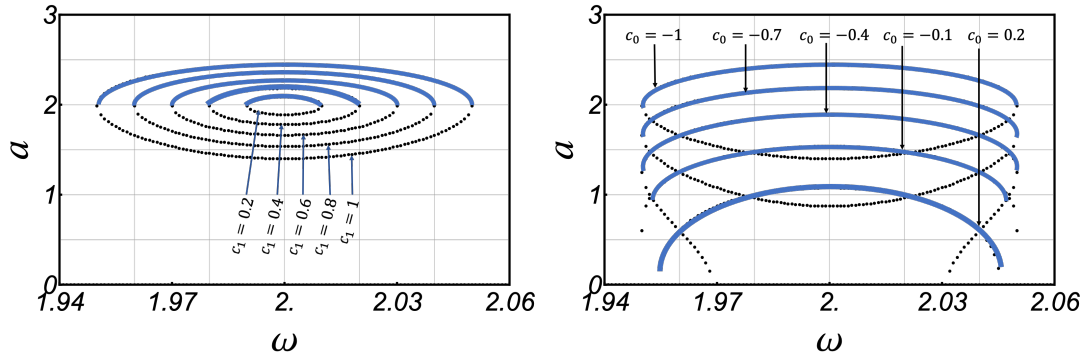


Figure 6.3: PDVDP with parametric excitation only: nonzero steady-State response amplitude versus the excitation frequency in the case of sub-harmonic resonance. Left: $c_0 = -1$ and $c_1 = \{0.2, 0.4, 0.6, 0.8, 1\}$. Right: $c_1 = 1$ and $c_0 = \{-1, -0.7, -0.4, -0.1, 0.2, 0.5, 0.8\}$. Solid and dotted curves are stable and unstable branches.

larger response amplitude; see the left panel in Fig. 6.3 where the inner and outer ellipses are associated with $c_1 = 0.2$ and $c_1 = 1$, respectively. An increase in the mean value of damping $c_0$, however, decreases the response amplitude by moving down the ellipse till the horizontal axis $a = 0$, beyond which the lower branch of ellipse disappears; see the right panel in Fig. 6.3.

#### 6.2.2.1 Stability Analysis.

To investigate the stability of the obtained fixed point, we study the corresponding eigenvalues of the linear system at the fixed points. We obtain the linear system as

$$\begin{bmatrix} a' \\ \gamma' \end{bmatrix} = \begin{bmatrix} -\frac{1}{4}a^2 & \frac{1}{2}a\sigma \\ 0 & -(c_0 + \frac{1}{4}a^2) \end{bmatrix} \begin{bmatrix} a \\ \gamma \end{bmatrix}, \tag{6.18}$$

where $[\mathcal{F}]$ is the Jacobian matrix given as

$$\Big[\mathcal{F}\Big] = \begin{bmatrix} -\frac{1}{4}a^2 & \frac{1}{2}a\sigma \\ 0 & -(c_0 + \frac{1}{4}a^2) \end{bmatrix} \tag{6.19}$$

for which the Jacobian matrix has trace $T = -c_0 - \frac{a^2}{2}$ and determinant $D = \frac{1}{4}a^2(c_0 + \frac{a^2}{4})$. A fixed point (steady-state amplitude $a$) is stable if $D > 0$, i.e. $a^2 + 4c_0 > 0$, and $T < 0$,

i.e. $a^2 + 2c_0 > 0$. Thus, based on Eqn. (6.17), if $\frac{c_1^2}{4} - \sigma^2 > 0$, then the nonzero fixed point exists and the $D > 0$ criterion implied that the positive (upper) branch is stable, while the lower branch is unstable. The $a = 0$ solution is neutrally stable if $c_0 > 0$.

And, if $\frac{c_1^2}{4} - \sigma^2 > 0$, then the fixed point $a^2 = -4c_0 + 4\sqrt{\frac{c_1^2}{4} - \sigma^2}$ is stable.

#### 6.2.2.2 Dynamics of the Amplitude and Phase.

Figure 6.4 shows the stable and unstable branches of steady-state amplitude response (top panel) and the amplitude-phase trajectories (bottom panel) at different frequencies $\omega = \{1.95, 1.98, 2, 2.04, 2.05, 2.055\}$. The parameters are set to be $\epsilon = 0.1$, $\omega_n = 1$, $c_0 = -1$, and $c_1 = 1$. The upper panel shows that between frequencies of $\omega = 1.95$ and $\omega = 2.05$, there exist two steady-state response amplitudes $a$, one on each branch of the oval-shaped curve. For $\omega < 1.95$ and $\omega > 2.05$, there are no nonzero fixed points. However, note that Eqns. (6.16) exist on a cylindrical state space, and for these frequency ranges they admit a periodic "whirling" solution, whose mean is approximated in the figure. Examples are depicted in the the lower panels for $\omega = 1.93$ for which the periodic solution travels from right to left, and for $\omega = 2.055$, for which the periodic solution travels to the right. As such, the amplitude $a$ of the leading order solution has a periodic fluctuation, and the oscillator is quasi-periodic, as labeled in the top panel of Figure 6.4.

As $\omega$ increases, the two fixed points in $(a, \gamma)$ are created in a saddle-node bifurcation at $\omega = 1.95$. Likewise, when the frequency reaches $\omega = 2.05$, the two fixed points in $(a, \gamma)$ collide and disappear in another saddle-node bifurcation. Lower panel 2 shows the two fixed points after the first saddle-node bifurcation. With increasing frequency, the saddle moves to the left, while the stable node moves to the right. In panel 3, at $\omega = 2.0$, the stable node has $\gamma = 0$ while the saddle has $\gamma = \pm\pi/2$, indicated at both slices of the cylindrical phase space. In panel 4, the saddle and node have continued their trek to the left and right, respectively, and they are approaching each other. In panel 5, at $\omega = 2.05$, the second saddle-node bifurcation has been reached, and the two fixed points coalesce. Panel 6 then

shows the trajectories after the second saddle-node bifurcation.

Some information about the periodic whirling orbits can be gleaned from Eqns. (6.16). These equations have a rectangular "trapping region" [35] bounded by $a^2_{min} = -4c_0 - 2c_1$ and $a^2_{max} = -4c_0 + 2c_1$. This is shown as the gray shaded area in the top panel. When $\omega = 1.93$ and $\omega = 2.055$ (before and after the saddle-node bifurcations), there are no fixed points in the trapping region, and therefore the trapping region contains a periodic (whirling) orbit bounded by $a_{min}$ and $a_{max}$. This is consistent with Fig. 6.2 and Fig. 6.4, where the response amplitudes are trapped in the range $[\sqrt{2}, \sqrt{6}]$.

Let us examine the temporal characteristics of the whirling orbit. The second term of Eqns. (6.16) is a differential equation for $\gamma$ which is independent of $a$. Depending on $c_1$ and $\sigma$, there can be a range of $\gamma$ for which its phase flow is fast, and a range that is slow. In the lower part of Fig. 6.4, in panel 1 (negative $\sigma$) the slow interval is $-\pi < \gamma < 0$, while in panel 2 (positive $\sigma$) the slow interval is $0 < \gamma < \pi$. In both cases, the $\gamma$ flow is fast to $a_{max}$ and slow to $a_{min}$, somewhat like a relaxation oscillation. This can be seen in Fig. 6.2, for the cases of $\omega = 1.93$ and $\omega = 2.055$, where the response amplitudes decrease slowly to $a = \sqrt{2}$, and increase quickly to the maximum amplitude near $a = \sqrt{6}$.

The second term of Eqns. (6.16) is independent of $a$ and is separable. It can be integrated to obtain $T_1$ as a function of $\gamma$. For example, when $\sigma > 0$, a cycle is completed from $\gamma = -\pi$ to $\gamma = \pi$. These conditions can be used to determine the integration constants. As a result, and accounting for $T_1 = \epsilon t$, the period of whirling is

$$T_{est} = \frac{2\pi\epsilon}{\sigma\sqrt{1 - (c_1/2\sigma)^2}}, \tag{6.20}$$

which is an estimate, since the slow flow (6.16) was obtained through an asymptotic perturbation expansion. Using this expression, the period of beating of the solutions depicted in Fig. 6.2 is $T_{est} = 128$ s compared to the observed $T = 135$ s for the case of $\omega = 1.93$, and $T_{est} = 225$ s compared to the observed $T = 274$ s for the case of $\omega = 2.055$.

Since $2\beta = \sigma T_1 - \gamma$, the leading-order solution is

$$x_0 = a(T_1)\cos(\omega_n T_0 + \beta(T_1)) = a(T_1)\cos(\frac{1}{2}(\omega T_0 - \gamma(T_1)). \tag{6.21}$$

Thus, at subharmonic resonance, the response has a reference frequency at half the forcing frequency, with amplitude and phase fluctuations. When $1.95 < \omega < 2.05$ and there is a stable fixed point in $(a, \gamma)$, the steady-state solution has a fixed amplitude and phase, and is phase locked. Otherwise the oscillator is in phase drift: when $\omega < 1.95$ the decreasing phase whirl decreases the mean frequency, and when $\omega > 2.05$ the increasing phase whirl increases the mean frequency, by an estimated amount $2\pi/T_{est}$, while the amplitude fluctuates.

### 6.2.3 Comments

We have only detected a subharmonic resonance with the perturbation analysis of the system with no external forcing. The first-order perturbation analysis does not reveal a primary or superharmonic resonance. Similarly, the frequency sweep (Fig. 6.1) does not indicate such resonant activity for the simulated parameters.

## 6.3 Parametric and External Excitation

In this case, the external forcing terms $f_0$ and $f_1$ are nonzero. Similar to the previous case, as a survey of the possible dynamics, Fig. 6.5 shows a frequency sweep from $\omega = 0$ to beyond $\omega = 3\omega_n$, with parameters $\omega_n = 1$, $c_0 = -1$, $c_1 = 1$, $f_0 = 0.2$, and $f_1 = 1$. The sweep is based on numerical simulations and the steady-state response amplitudes are plotted. The plot shows that significant quasi-periodic dynamics occur for a large range of excitation frequencies with periodic windows around $\omega \approx \omega_n$, $\omega \approx 2\omega_n$, and $\omega \approx 3\omega_n$. The largest responses occur near the primary resonance range and then for subharmonic ones. Super harmonic resonances are not apparent.

In this case, the particular solution to the leading order Eqn. (6.4) is

$$x_0(T_0, T_1) = \Gamma + i\Lambda\, e^{i\omega T_0} + A(T_1)e^{i\omega_n T_0} - i\Lambda\, e^{-i\omega T_0} + \bar{A}(T_1)e^{-i\omega_n T_0}, \tag{6.22}$$

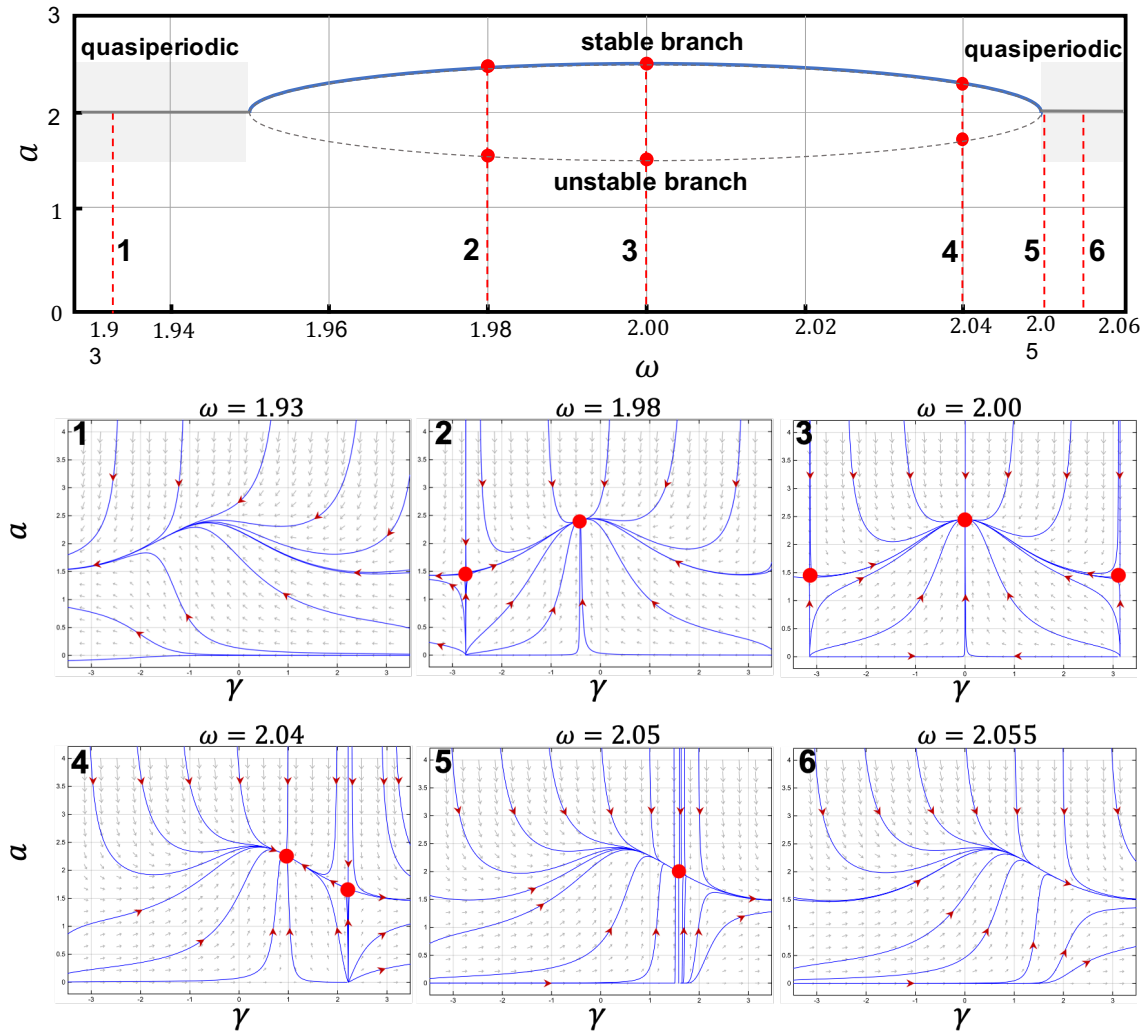


Figure 6.4: PDVDP with parametric excitation only. Top panel: steady-state amplitude response versus excitation frequency close to the sub-harmonic resonance. Bottom panel: amplitude-phase trajectories at different corresponding frequencies $\omega = \{1.93, 1.98, 2, 2.04, 2.05, 2.055\}$. The simulation parameters are $\epsilon = 0.1$, $\omega_n = 1$, $c_0 = -1$, and $c_1 = 1$.

where $\Gamma = \frac{f_0}{\omega_n^2}$ and $\Lambda = \frac{f_1}{2(\omega^2 - \omega_n^2)}$. By plugging Eqn. (6.22) in Eqn. (6.5), we obtain

$$
\begin{aligned}
&D_0{}^2 x_1 + w_n{}^2 x_1 = (-2i\omega_n A' - ic_0\omega_n A - i\omega_n \Gamma^2 A - i\omega_n A^2 \bar{A} - 2i\omega_n \Lambda^2 A) e^{i\omega_n T_0} \\
&+(c_0\omega\Lambda + \omega\Gamma^2\Lambda + \omega\Lambda^3 + 2\omega A\bar{A}\Lambda) e^{i\omega T_0} + (\frac{c_1}{2}\omega\Lambda + 2i\omega\Gamma\Lambda^2) e^{2i\omega T_0} \\
&-\omega\Lambda^3\, e^{3i\omega T_0} + (i\frac{c_1}{2}\omega_n\bar{A} - 2\omega_n\Lambda\Gamma\bar{A} + 2\omega\Lambda\Gamma\bar{A}) e^{i(\omega-\omega_n)T_0} \\
&+i(2\omega - \omega_n)\Lambda^2\, \bar{A} e^{i(2\omega-\omega_n)T_0} + (\omega - 2\omega_n)\Lambda\bar{A}^2 e^{i(\omega-2\omega_n)T_0} + \text{c.c.} + \text{N.S.T.}.
\end{aligned}
\tag{6.23}
$$

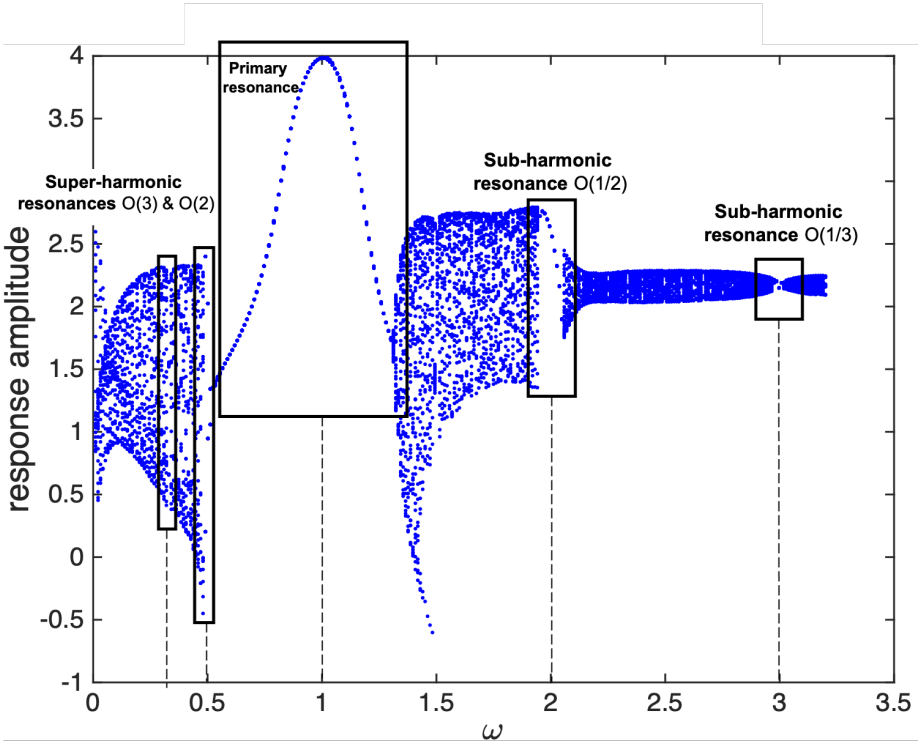


Figure 6.5: PDVDP with parametric and external excitation. The response amplitude versus the excitation frequency $\omega$ where $f_0 = 0.2, f_1 = 1, \omega_n = 1, \epsilon = 0.1, c_0 = -1$ and $c_1 = 1$.

The right-hand-side of Eqn. (6.23) shows different cases of resonance; each can produce different secular terms. The cases are nonresonant, subharmonic resonance of orders 1/2 and 1/3, and superharmonic resonance or order 2. Here we study the first two cases. The third case (superharmonic of order 1/3) does not involve the parametric term, and others turn out to be of minimal significance. For the first two cases, we obtain the following solvability conditions.

• Non-Resonant:

$$-2i\omega_n A' - ic_0\omega_n A - i\omega_n \Lambda^2 A - i\omega_n A^2 \bar{A} - 2i\omega_n \Gamma\bar{\Gamma} A = 0 \tag{6.24}$$

• Primary Resonance ($\omega = \omega_n$):

$$\begin{aligned} &-2i\omega_n A' - ic_0\omega_n A - i\omega_n \Lambda^2 A - i\omega_n A^2 \bar{A} - 2i\omega_n \Gamma\bar{\Gamma} A \\ &-(ic_0\omega\Gamma + i\omega\Lambda^2\Gamma + i\omega\Gamma^2\,\bar{\Gamma} + 2i\omega A\bar{A}\Gamma + i(2\omega - \omega_n)\Gamma^2\,\bar{A})e^{i\sigma T_1} = 0 \end{aligned} \tag{6.25}$$

• Sub-harmonic Resonance of Order 1/2 ($\omega = 2\omega_n$):

$$-2i\omega_n A' - ic_0\omega_n A - i\omega_n\Lambda^2 A - i\omega_n A^2\bar{A} - 2i\omega_n\Gamma\bar{\Gamma}A$$
$$+(i\frac{c_1}{2}\omega_n\bar{A} + 2i\omega_n\Lambda\Gamma\bar{A} - 2i\omega\Lambda\bar{A}\Gamma)e^{i\sigma T_1} = 0 \tag{6.26}$$

• Sub-harmonic Resonance of Order 1/3 ($\omega = 3\omega_n$):

$$-2i\omega_n A' - ic_0\omega_n A - i\omega_n\Lambda^2 A - i\omega_n A^2\bar{A} - 2i\omega_n\Gamma\bar{\Gamma}A$$
$$-i(\omega - 2\omega_n)\Gamma\bar{A}^2 e^{i\sigma T_1} = 0 \tag{6.27}$$

• Super-harmonic Resonance of Order 2 ($\omega = \omega_n/2$):

$$-2i\omega_n A' - ic_0\omega_n A - i\omega_n\Lambda^2 A - i\omega_n A^2\bar{A} - 2i\omega_n\Gamma\bar{\Gamma}A$$
$$-(i\frac{c_1}{2}\omega\Gamma + 2i\omega\Lambda\Gamma^2)e^{i\sigma T_1} = 0 \tag{6.28}$$

• Super-harmonic Resonance of Order 3 ($\omega = \omega_n/3$):

$$-2i\omega_n A' - ic_0\omega_n A - i\omega_n\Lambda^2 A - i\omega_n A^2\bar{A} - 2i\omega_n\Gamma\bar{\Gamma}A - i\omega\Gamma^3 e^{i\sigma T_1} = 0 \tag{6.29}$$

We do not treat primary resonance since, in such case, $\Gamma$ becomes large and contradicts the multiple-scales bookkeeping strategy. Primary resonance is to be analyzed with weak excitation. The nonresonant case, subharmonic of order 1/3, and superharmonic of order 3 do not involve the parametric damping term. Thus, the behavior should be similar to the forced van der Pol system. However, the subharmonic of order 1/2 and the superharmonic of order 2 involve both van der Pol and parametric damping terms together. We first study the nonresonant case and then focus on the case of sub-harmonic resonance of order 1/2.

Although Fig. 6.5 indicates the primary resonance as a prominent case when $\omega \approx \omega_n$, the coefficient $\Lambda$ becomes singular and would contradict the multiple-scales bookkeeping strategy. The analysis of primary resonance case requires weak excitation, as well as a second-order perturbation analysis to capture the parametric term, as in [82]. This will be analyzed in a separate study.

### 6.3.1 Nonresonant Case

The solvability condition in Eqn. (6.24) is not affected by the parametric damping term and hence the behavior is similar to the forced van der Pol equation [73, 88]. In this case, the phase equation becomes $\beta' = 0$, and hence the phase $\beta$ is constant and does not influence the oscillation frequency. The amplitude equation yields the following steady-state solutions

$$a = 0, \qquad a = 2\sqrt{-c_0 - \Gamma^2 - 2\Lambda^2}, \tag{6.30}$$

where the zero solution is unstable and the nonzero solution exists and is stable when $\Gamma^2 + 2\Lambda^2 < -c_0$. Since $\Gamma^2 + 2\Lambda^2 > 0$, a negative value of $c_0$ is necessary (but not sufficient) for nonzero $a$. If the above condition is not satisfied, then the trivial solution $a = 0$ is stable.

Since the leading-order solution has the form

$$x_0 = \Gamma - 2\Lambda \sin \omega T_0 + a \cos(\omega_n T_0 + \beta) \tag{6.31}$$

when the condition $\Gamma^2 + 2\Lambda^2 < -c_0$ is satisfied, $a \neq 0$ and the response becomes quasiperiodic. Otherwise, with sufficient increase in the excitation ($\Lambda$ and $\Gamma$), $a$ is suppressed and the response becomes periodic; known as quenching [73, 88].

The parametric terms affect the first-order correction, $x_1$, in the approximate solution $x(t) = x_0(t_0, T_1) + \epsilon x_1(T_0, T_1)$. In eliminating the secular terms, there are several contributions of different frequency components, including $2\omega, \omega - \omega_n, \omega + \omega_n$, from parametric excitation and van der Pol terms, and $2\omega_n, 3\omega_n, 3\omega, 2\omega - \omega_n, 2\omega + \omega_n, \omega - 2\omega_n$, and $\omega + 2\omega_n$, from the van der Pol terms. Thus the first-order solution can contribute two-frequency quasiperiodic effects, as the content of the total response has a linear combination of two frequencies.

### 6.3.2 Sub-harmonic Resonance of Order 1/2

In this case, the excitation and natural frequency form the relation $\omega = 2\omega_n + \epsilon\sigma$. We see from the solvability condition in Eqn. (6.26) that in addition to the non-resonant

secular terms in Eqn. (6.24), the parametric damping and forcing appear. We substitute $A(T_1) = \frac{1}{2}a(T_1)e^{i\beta(T_1)}$ into the equation and let $\gamma = \sigma T_1 - 2\beta$. Then, the autonomous coupled system of governing equations of the amplitude $a$ and phase $\gamma$ becomes

$$\begin{aligned} a' + \frac{1}{8}a^3 + (\frac{c_0}{2} + \frac{\omega_n\Gamma^2}{2} + \Lambda^2 - \frac{c_1}{4}\cos\gamma + \Gamma\Lambda(1 - \frac{\omega}{\omega_n})\sin\gamma)a = 0, \\ a\gamma' - a\sigma + \frac{c_1}{2}a\sin\gamma + 2a\Gamma\Lambda(1 - \frac{\omega}{\omega_n})\cos\gamma = 0. \end{aligned} \tag{6.32}$$

The fixed points of Eqn. (6.32) are obtained in the steady-state case when $a' = \gamma' = 0$, which admits $a = 0$ and a nontrivial solution. The equations for the nontrivial solution take the form

$$A_1\sin\gamma + B_1\cos\gamma = C_1, \quad A_2\sin\gamma + B_2\cos\gamma = C_2,$$

where the coefficients $A_1$, $A_2$, $B_1$, $B_2$, $C_1$, and $C_2$ are functions of the parameters and the amplitude $a$. By solving for $\sin\gamma$ and $\cos\gamma$, and using the trigonometric identities, we remove the variable $\gamma$ and form a parametric algebraic equation to obtain the steady-state amplitude $a$ as,

$$\begin{aligned} &a^4 + 8a^2(c_0 + 2\Lambda^2 + \Gamma^2) + 4\left(4{c_0}^2 + 16c_0\Lambda^2 - {c_1}^2 + 16\Lambda^4 + 4\sigma^2\right) \\ &+16\Gamma^2\left(2c_0 - 4\Lambda^2\frac{\omega}{\omega_n}(\frac{\omega}{\omega_n} - 2) + \Gamma^2\right) = 0. \end{aligned} \tag{6.33}$$

Solving for $a^2$ yields the steady-state response amplitude,

$$a^2 = -2\left(2\Gamma^2\omega_n + 2c_0\omega_n + 4\Lambda^2\omega_n \pm \Gamma\Lambda\sqrt{\frac{{c_1}^2 - 4\sigma^2}{\Gamma^2\Lambda^2} + \frac{16(\omega - \omega_n)^2}{{\omega_n}^2}}\right) \tag{6.34}$$

which is valid if the square root in the solution is real, and if $a^2 \geq 0$. The first criterion reduces to $4\sigma^2 < c_1^2 + 16\Gamma^2\Lambda^2$, when using $\omega - \omega_n \approx \omega_n$. Thus the frequency range of fixed amplitude solutions increases with $c_1$, $f_0$, and $f_1$.

Based on Eqn. (6.22) and the definition of $\gamma$, the leading order solution takes the form

$$x_0 = \Gamma - 2\Lambda\sin(\omega T_0) + a\cos(\frac{\omega}{2}T_0 - \frac{\gamma}{2}). \tag{6.35}$$

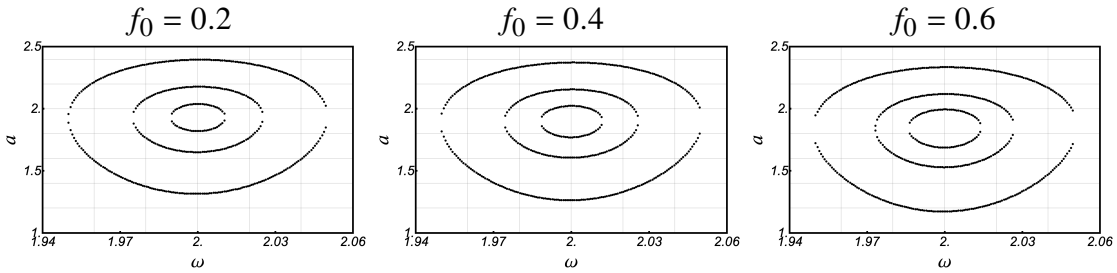


Figure 6.6: PDVDP with parametric and external excitation in the case of sub-harmonic resonance where $c_0 = -1$ and $f_1 = 1$. The three plotted curves correspond to $c_1 = \{0.2, 0.5, 1\}$, and the panels are for $f_0 = \{0.2, 0.4, 0.6\}$. Solid and dotted curves are stable and unstable branches.

For the case when $a$ and $\gamma$ are fixed and stable, there is a periodic (phase locked) response of fundamental frequency $\omega/2$. When a steady-state solution $a$ does not exist, the response is in phase drift, and is quasiperiodic.

Figure 6.6 shows the steady-state response amplitude versus the excitation frequency for small values of detuning parameter, when $\epsilon = 0.1$ and $-\sigma_0 < \sigma < \sigma_0$. Note that these figures show the amplitude $a$ of one term in Eqn. (6.35). The phase $\gamma$ would affect peak-to-peak amplitudes. The mean damping and periodic forcing are set to be constant, $c_0 = -1$ and $f_1 = 1$, while different values of $c_1 = \{0.2, 0.5, 1\}$ produce different ellipses. The larger values of $c_1$ are associated with the larger ellipses. We see that as the constant forcing term $f_0$ is varying between $\{0.2, 0.4, 0.6\}$, the ellipses are expanding and the limit cycle amplitude increases. Note that the upper curves represent the stable response and the lower curves are the unstable response. The numerical solutions in Fig. 6.7 demonstrate that when $\omega = 0.12$, the response is quasi-periodic. This is consistent with the leading order solution presented in Eqn. (6.35). Like the unforced case, $\omega = 1.93$ and $\omega = 2.055$ are the edge points around the subharmonic resonance. These two cases are expected to have the nonresonant solutions.

Figure 8 shows the dynamics of the amplitude and phase for the forced excitation, represented by equations (6.32). The behavior is similar to the unforced case. For $\sigma < \sigma_0$, a periodic whirling solution traveling from right to left, and for $\sigma > \sigma_0$ the whirling

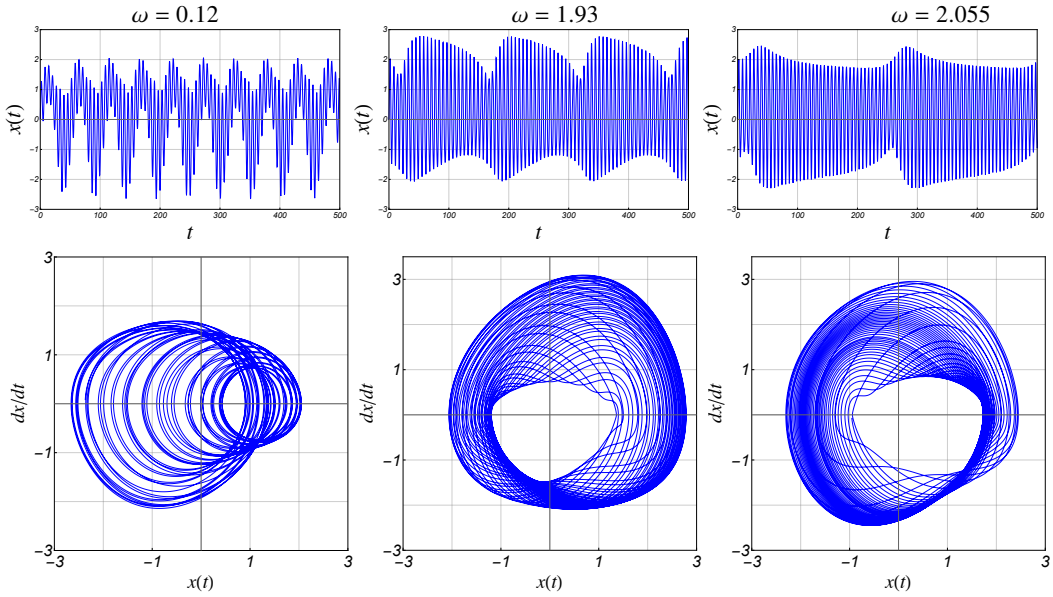


Figure 6.7: PDVDP with parametric and direct excitation: Time response (top row) and phase portrait (bottom row) at different excitation frequencies where $f_0 = 0.2$ and $f_1 = 1, \omega_n = 1, \epsilon = 0.1, c_0 = -1$ and $c_1 = 1$.

solution travels to the right. Therefore, in the leading order solution the amplitude $a$ has a periodic fluctuation, and the oscillator is quasi-periodic. If $4\sigma^2 < c_1^2 + 16\Gamma^2\Lambda^2$ there exists nonzero response amplitude and the amplitude falls into a trapping region $[a_{min}, a_{max}]$, where solving for $a' \leq 0$ from the first term of Eqns.(6.32), $a_{min} = 1.27$ and $a_{max} = 2.38$. These values are consistent with Fig. 6.8 and Fig. 6.7. The second term of Eqns. (6.16) is used to find the time characteristics of the whirling orbit of the system with the external excitation. For a complete cycle, from $\gamma = -\pi$ to $\gamma = \pi$, $T_{est}$ is calculated. Considering $T_1 = \epsilon t$, the estimated period of whirling for the case of panel 6 in Fig. 6.8 is $T_{est} = 286.1$ s compared to the observed $T = 241$ s in Fig. 6.8.

By considering Eqn. (6.32), we can argue that if there are no fixed points in $(a, \gamma)$, we can expect a periodic whirling, where the leading order solution (6.4) includes a time varying amplitude $a$ and phase $\gamma$, and as such the response will be quasiperiodic. In contrast, when there is a stable fixed point in $(a, \gamma)$, the response becomes phase locked and periodic. The subharmonic behavior of the parametric plus direct excitation is thus

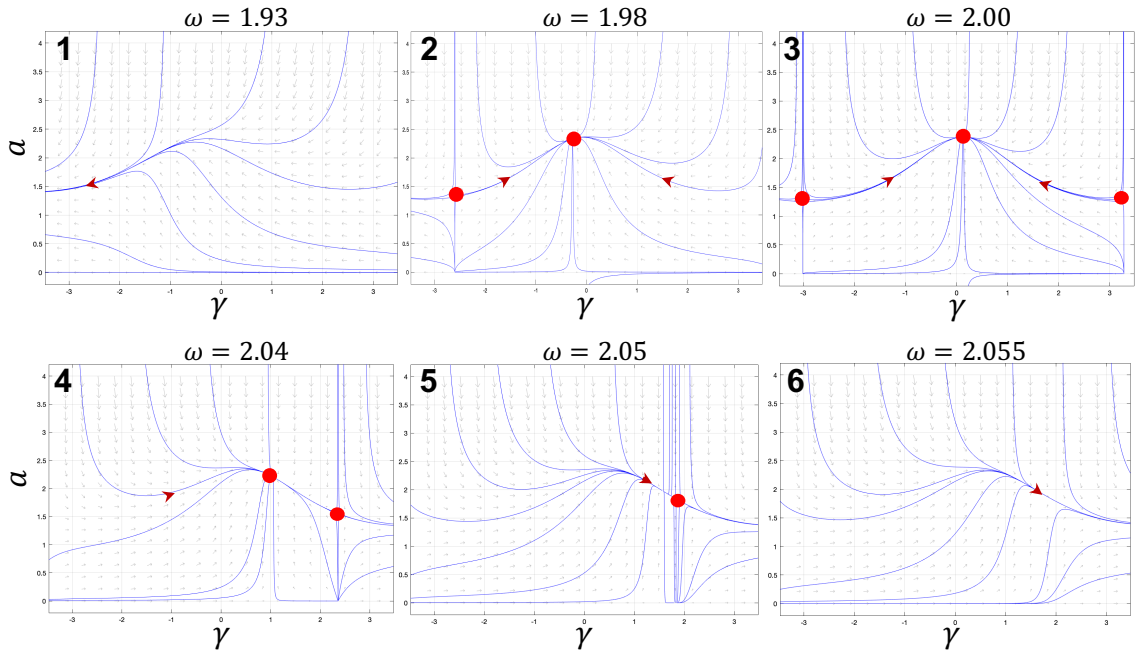


Figure 6.8: PDVDP with parametric and direct excitation. Amplitude-phase trajectories at different corresponding frequencies $\omega = \{1.93, 1.98, 2, 2.04, 2.05, 2.055\}$. The simulation parameters are $\epsilon = 0.1$, $\omega_n = 1$, $c_0 = -1$, and $c_1 = 1$.

similar to that of the parametric excitation only, except that the solutions for the steady amplitudes are complicated and distorted by the direct excitation terms $f_0$ and $f_1$.

### 6.3.3 Super-harmonic Resonance of Order 2

In this case, the excitation and natural frequency form the relation $2\omega \approx \omega_n$. Similar to the sub-harmonic resonance, we see from the solvability condition in Eqn. (6.28) that in addition to the non-resonant secular terms in Eqn. (6.24), the parametric damping and forcing appear again. We substitute $A(T_1) = \frac{1}{2}a(T_1)e^{i\beta(T_1)}$ into the equation and let $\gamma = \sigma T_1 - \beta$. Then, the coupled system of governing equations of the amplitude $a$ and phase $\gamma$ becomes

$$\begin{aligned} -a' - \frac{a^3}{8} - \frac{1}{2}a\Gamma^2 - \frac{ac_0}{2} - a\Lambda^2 + 2\Gamma\Lambda^2\frac{\omega}{\omega_n}\cos(\gamma) + \frac{1}{2}c_1\Lambda\frac{\omega}{\omega_n}\sin(\gamma) = 0, \\ -a\gamma' + a\sigma - 2\Gamma\Lambda^2\frac{\omega}{\omega_n}\sin(\gamma) + \frac{1}{2}c_1\Lambda\frac{\omega}{\omega_n}\cos(\gamma) = 0. \end{aligned} \tag{6.36}$$

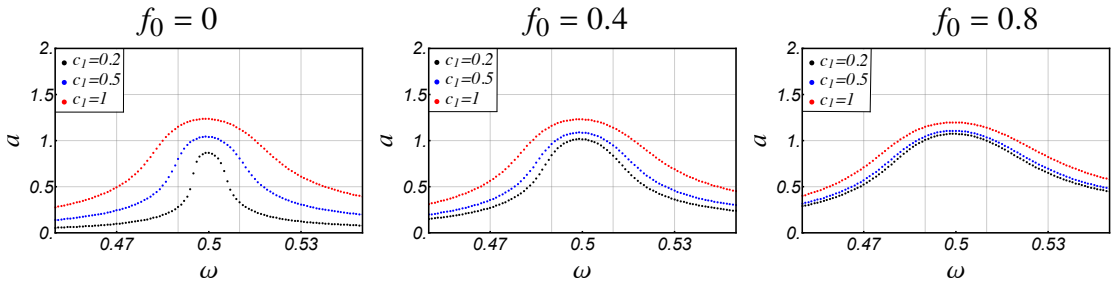


Figure 6.9: PDVDP with parametric and external excitation. Steady-State response amplitude versus the excitation frequency in the case of super-harmonic resonance where $c_0 = -1$ and $f_1 = 1$. The three plotted curves correspond to $c_1 = \{0.2, 0.5, 1\}$, and the panels are for $f_0 = \{0, 0.4, 0.8\}$.

For the super-harmonic case the fixed points are found by setting $a' = \gamma' = 0$ in Eqn. (6.37). By taking the similar approach as in the sub-harmonic case, the parametric algebraic relation can be obtained to solve for steady-state amplitude $a$,

$$\frac{a^2\omega_n{}^2\left(a^2\Gamma\Lambda + 4\Gamma^3\Lambda + 8\Gamma\Lambda^3 + 4\Gamma c_0\Lambda - 2c_1\sigma\right)^2}{\Lambda^2\Omega^2\left(16\Gamma^2\Lambda^2 + c_1{}^2\right)^2} + \frac{a^2\omega_n{}^2\left(a^2c_1 + 4\left(8\Gamma\Lambda\sigma + c_0c_1 + \Gamma^2c_1 + 2c_1\Lambda^2\right)\right)^2}{16\Lambda^2\Omega^2\left(16\Gamma^2\Lambda^2 + c_1{}^2\right)^2} - 1 = 0. \tag{6.37}$$

Figure 6.9 demonstrates the steady-state response amplitude for varying values of excitation frequencies where $c_0 = -1$, $c_1 = \{0.2, 0.5, 1\}$, and $f_0 = \{0, 0.4, 0.8\}$. Marching from the outer curve to the inner curve the value of $c_1$ is descending. Increasing $f_0$ increases the amplitude of the response such that the curves with lower values of $c_1$ are expanded more.

## 6.4 Summary and Conclusion

In this paper we studied the resonance of a forced and unforced van der Pol equation with parametric damping. Applications can include vertical-axis wind turbine blade vibration, which can have parametric damping and van-der-pol type terms in simplified models. The first-order method of multiple scales and numerical solutions were used.

The parametric damping with no external excitation demonstrated nonresonant and subharmonic resonance cases, where the system shows an oscillatory quasi-periodic

behavior in the former case. In the latter resonance case, we found the steady-state amplitude versus the excitation frequency for different damping parameters. When $c_0 = -1$ (negative linear damping as with the van der Pol oscillator), the resonant response amplitude increases with the parametric damping $c_1$. An increase in the mean value of damping $c_0$, however, decreases the response amplitude. The dynamics of the amplitude and phase showed saddle-node bifurcations coinciding with phase locking, in which periodically whirling amplitude and phase (quasiperiodic oscillations) were replaced with a fixed steady-state amplitude and phase (periodic oscillations).

We then studied van der Pol with parametric and direct excitation. In the nonresonant case the parametric damping term does not contribute in the solvability condition and therefore it showed the same behavior as the forced van der Pol. The nonresonant system can exhibit the quenching phenomenon when the excitation through the direct forcing is sufficiently large.

The subharmonic resonance behavior was similar to that of the parametric excitation without direct excitation, except that the direct excitation terms complicate and distort the steady solutions. Increasing the parametric damping parameter, $c_1$, increases the steady-state amplitude, and the direct forcing, $f_0$ and $f_1$ deformed the ellipse.

In addition to the nonresonant and subharmonic resonance van der Pol with parametric and direct excitation experienced superharmonic resonance. It was shown that the amplitude of the response increases with $c_1$, $f_0$, and $f_1$.

Our numerical studies showed the primary resonance as a dominant forced response case. The analysis of this case requires further investigation that will be done as a subsequent study with weak excitation. Based on previous studies on the cases with forcing and cyclic stiffness [82], we expect that a second-order multiple-scales analysis should be considered to correctly pull out the contribution of the parametric damping to the different resonance cases.

# CHAPTER 7

# MODAL ANALYSIS OF CURVED VERTICAL-AXIS DARRIEUS WIND TURBINE BLADE

An assumed modes method is presented to analyse the curved beam with the simplified equations of motion. The governing equations are presented in the line integral format, therefore a numerical solution based on the curvilinear integral along the neutral line of the curvilinear beam are carried out to solve the governing equations. The results for the modal frequencies, normal modes and the deformed configurations of curved beam with different boundary conditions (pin-pin and clamp-clamp) are obtained and compared with the FE analysis performed in Abaqus and also those reported in literature.

## 7.1 Analysis

A Darrieus vertical axis wind turbine blade is modeled as a curved beam of length $2S$ and symmetric cross section. Figure 7.1 [51] shows, on the left, a schematic diagram of a curved beam attached at both ends to the top and bottom of the tower, which is assumed to be rigid. On the right of the figure is the magnified symmetric cross section. A coordinate $s$ is defined along the shear center of the beam, and has values of $s = -S$ at the base of the tower, and $s = S$ at the top of the tower. At the apex of the curved beam, we have $s = 0$. The concentration of this study is the structural modal dynamics of the curved beam with in-plane and out-of-plane vibration, where the blade experiences four coupled deformations: $u(s,t)$ and $v(s,t)$ are flat-wise and edge-wise bending, respectively; $w(s,t)$ is axial extension; and $\phi(s,t)$ is twist about the centroidal axis. Flatwise bending involves deflections $u$ in the $x_3$ direction shown in the right-hand figure, edgewise deflections $v$ are in the $y_3$ direction, and axial deformation $w$ is in the $s$ direction. (Coordinate $s$ coincides with $z_3$ not labeled in the figure.) Eight different coordinate systems are introduced to describe the deformations of the curved beam. Figure 7.1 [51] illustrates some of these coordinate systems attached to the blade before and after deformation. We will explain the

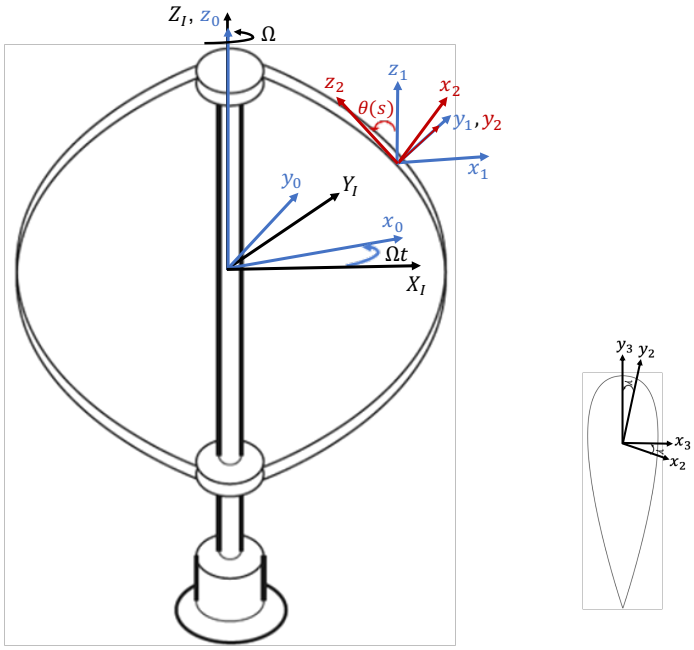


Figure 7.1: Darrieus curved blade configuration and the cross section with the coordinate systems [51].

dynamics of the curved beam extensively.

**Undeformed Blade** Let $\mathbf{x}_I = (X_I, Y_I, Z_I)$ be the inertial coordinates where the origin is at the midpoint of the tower. $Z_I$ is attached to the rotor axis, $X_I$ is radial, and $Y_I$ is orthogonal to $X_I$ and $Z_I$ to form a right-handed system, with the unit vectors $\{\mathbf{e}_I\} = (\mathbf{e}_{X_I}, \mathbf{e}_{Y_I}, \mathbf{e}_{Z_I})$. The coordinate system $\mathbf{x}_0 = (x_0, y_0, z_0)$, with unit vectors $\{\mathbf{e}_0\} = (\mathbf{e}_{x_0}, \mathbf{e}_{y_0}, \mathbf{e}_{z_0})$, is attached to the rotor and rotates with the rotor at the constant rotational speed Ω. For example, the shear center of the midpoint of the undeformed, rotating blade has coordinates $(x_0, y_0, z_0) = (R, 0, 0)$, where $R$ is the distance from the origin to the apex of the blade. Then $\mathbf{x}_0 = T_3(\chi)\mathbf{x}_I$, where $T_3(\chi)$ indicates a rotational transformation about the third axis ($Z_I$ here) through and angle $\chi = \Omega t$. (The subscript "3" refers to the third axis.) Specifically,

$$T_3(\chi) = \begin{bmatrix} \cos\chi & -\sin\chi & 0 \\ \sin\chi & \cos\chi & 0 \\ 0 & 0 & 1 \end{bmatrix} \tag{7.1}$$

Let $\mathbf{x}_1 = (x_1, y_1, z_1)$ be parallel to $\mathbf{x}_0$ but translated (in the rotating frame) to the shear center of the undeformed blade at $s$, by the vector $\mathbf{R}_0(s)$. That is, $\mathbf{R}_0$ is the position of the shear center of the cross section with relative to the rotor. The frame $\mathbf{x}_1$ has rotating unit vectors $\mathbf{e}_{x_1}, \mathbf{e}_{y_1}, \mathbf{e}_{z_1}$. Then we have $\mathbf{x}_0 = \mathbf{x}_1 + \mathbf{R}_0$.

We seek a coordinate system that aligns with the principle axes of the blade cross section. We set $(x_2, y_2, z_2)$ as the blade coordinate system after the $(x_1, y_1, z_1)$ frame has been rotated by an angle $\theta(s)$ (of the undeformed blade arc) around the $-y_1$ axis. Then as in Fig. 7.1, $x_2$ and $y_2$ sit at the blade cross section and $z_2$ is tangent to the blade profile and perpendicular to the blade cross section. The unit vectors are $\{\mathbf{e}_2\} = (\mathbf{e}_{x_2}, \mathbf{e}_{y_2}, \mathbf{e}_{z_2})$. Then $\mathbf{x}_2 = T_2(-\theta(s))\mathbf{x}_1$. $T_2$ also applies to orienting the basis vectors. Following a pre-twist $\gamma$ in the blade (Fig. 7.1),

$\mathbf{x}_3 = (x_3, y_3, z_3)$ is the coordinate system aligned with the principal axis of the blade cross section. Then $\mathbf{x}_3 = T_3(\gamma(s))\mathbf{x}_2$ and the unit vectors are $\{\mathbf{e}_3\} = (\mathbf{e}_{x_3}, \mathbf{e}_{y_3}, \mathbf{e}_{z_3})$. If the pre-twist angle ($\gamma$) is zero, the vector basis set $\{\mathbf{e}_3\}$ is the same as $\{\mathbf{e}_2\}$.

The transformation from $\mathbf{x}_1$ to $\mathbf{x}_3$ is then $\mathbf{x}_3 = T_u\mathbf{x}_1 = T_3(\gamma(s))T_2(-\theta(s))\mathbf{x}_1$. The composite undeformed geometric transformation matrix $T_u$ has direction cosines, $c_{ij}$, and we could write

$$T_u(s) = \begin{bmatrix} c_{11} & c_{12} & c_{13} \\ c_{21} & c_{22} & c_{23} \\ c_{31} & c_{32} & c_{33} \end{bmatrix} = \begin{bmatrix} \cos\gamma & \sin\gamma & 0 \\ -\sin\gamma & \cos\gamma & 0 \\ 0 & 0 & 1 \end{bmatrix} \begin{bmatrix} \cos\theta & 0 & \sin\theta \\ 0 & 1 & 0 \\ -\sin\theta & 0 & \cos\theta \end{bmatrix} \tag{7.2}$$

**Deformed Blade** The configuration of the deformed blade is defined in new sets of coordinate systems. Let $(x_4, y_4, z_4)$, $(x_5, y_5, z_5)$ and $(x_6, y_6, z_6)$ be the coordinate systems

in the deformed blade with a sequence of Euler rotations, which progress with $s$ along the shear-center axis. From frames 3 to 6 we have $\mathbf{x_6} = T_3(\beta_z(s))T_1(\beta_x(s))T_2(\beta_y(s))\mathbf{x}_3 = T_d(s)\mathbf{x}_3$. We can write

$$T_d(s) = \begin{bmatrix} \cos\beta_z & \sin\beta_z & 0 \\ -\sin\beta_z & \cos\beta_z & 0 \\ 0 & 0 & 1 \end{bmatrix} \begin{bmatrix} 1 & 0 & 0 \\ 0 & \cos\beta_x & -\sin\beta_x \\ 0 & \sin\beta_x & \cos\beta_x \end{bmatrix} \begin{bmatrix} \cos\beta_y & 0 & -\sin\beta_y \\ 0 & 1 & 0 \\ \sin\beta_y & 0 & \cos\beta_y \end{bmatrix} \tag{7.3}$$

The net direction cosines of elements of $T_d$ depend on sines and cosines of the deformation angles. The angles $\beta_y$ and $\beta_x$ are the rotation angles, around axes $y_3$ and $x_4$, respectively, due to deformation. The torsion angle $\beta_z = \aleph + \phi$ about $z_5$ is the summation of the "natural" torsion angle ($\aleph$) that occurs with bending, plus the shear-strain torsion angle ($\phi$). (Analogous to the contribution of bending and shear to the deflection angle in a Timoshenko beam [66].) The natural torsion angle occurs when the shear stresses are absent and the deformation coordinates are geometrically related. It can be shown that, for small deflections,

$$\sin\beta_x(s) \approx \frac{\partial v(s,t)}{\partial s}, \qquad \sin\beta_y(s) \approx \frac{\partial u(s,t)}{\partial s} - \frac{\partial\theta(s)}{\partial s}w(s,t) \tag{7.4}$$
$$\cos\beta_x(s) \approx 1 - \frac{1}{2}\left(\frac{\partial v(s,t)}{\partial s}\right)^2, \qquad \cos\beta_y(s) \approx 1 - \frac{1}{2}\left(\frac{\partial u(s,t)}{\partial s} - \frac{\partial\theta(s)}{\partial s}w(s,t)\right)^2$$

These and $\sin(\beta_z(s,t)) \approx \beta_z(s,t) \approx \aleph+\phi$ and $\cos(\beta_z(s,t)) \approx 1-\frac{1}{2}\beta_z(s,t)^2 \approx 1-\frac{1}{2}(\aleph+\phi)^2$ contribute to matrix ( 7.3).

Figure 7.2 illustrates a curved beam with length $2S$ and an airfoil cross section. $P_0$ and $P_1$ locate material points in the cross section before and after deformation. The positions to these points are $\mathbf{r}_0 = \mathbf{R}_0 + x_3\mathbf{e}_{x_3} + y_3\mathbf{e}_{y_3}$ and $\mathbf{r}_1 = \mathbf{R}_1 + x_3\mathbf{e}_{x_6} + y_3\mathbf{e}_{y_6}$. The blade cross section is assumed to be rigid and thus planar deformations are neglected. Therefore, the warping effect will be excluded and $x_3$ and $y_3$ remain constant in the deformed blade cross section. Recall that $\mathbf{R}_0$ is the vector from the origin to the elastic axis (shear center) of the cross section before deformation and is defined as $\mathbf{R}_0 = x_0\mathbf{e}_{X_0} + z_0\mathbf{e}_{Z_0}$. The

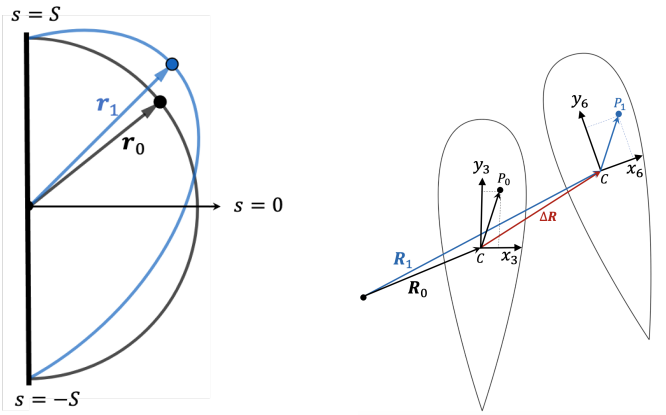


(a) (b)

Figure 7.2: $(a)$ Curved beam model. Black is undeformed and blue is deformed beam. $(b)$ Airfoil cross section. Left is the cross section of the undeformed and right is the cross section of the deformed beam. Note that $\mathbf{r}_0 = \mathbf{R}_0 + \vec{CP}_0$ (not shown in part (b)).

position of the elastic axis of the cross section after deformation is $\mathbf{R}_1 = \mathbf{R}_0 + \Delta\mathbf{R}$, where $\Delta\mathbf{R} = u\mathbf{e}_{x_3} + v\mathbf{e}_{y_3} + w\mathbf{e}_{z_3}$ is the deformation of the elastic axis, and is dependent on the displacement variables. (Fig. 7.2 schematically shows the vectors in the undeformed and deformed configurations of the blade).

Using the relationships between the different coordinate frames and the Euler angles with the displacements (Eqn. (7.4)), we can write $\mathbf{r}_0$ and $\mathbf{r}_1$ terms of a single set of basis vectors. We choose $(\mathbf{e}_{x_3}, \mathbf{e}_{y_3}, \mathbf{e}_{z_3})$. As such, following Kaza and Kvaternik [51], these

vectors have the form,

$$\mathbf{r}_0 = \mathbf{R}_0 + x_3\mathbf{e}_{x_3} + y_3\mathbf{e}_{y_3} \tag{7.5}$$

$$\begin{aligned}
&\mathbf{r}_1 = \mathbf{R}_0 + u\mathbf{e}_{x_3} + v\mathbf{e}_{y_3} + w\mathbf{e}_{z_3} + x_3\mathbf{e}_{x_6} + y_3\mathbf{e}_{y_6} = r_{1_x}\mathbf{e}_{x_3} + r_{1_y}\mathbf{e}_{y_3} + r_{1_z}\mathbf{e}_{z_3} \\
&= \mathbf{R}_0 + \Big(x_3 + +u(s,t) - y_3\big(\phi(s,t) + v(s,t)\theta'(s)\big) + x_3\Big( -\frac{1}{2}\big(\phi(s,t) + v(s,t)\theta'(s)\big)^2 \\
&-\frac{1}{2}\big( - w(s,t)\theta'(s) + u'(s,t)\big)^2\Big) + y_3(w(s,t)\theta'(s) - u'(s,t))v'(s,t)\Big)\mathbf{e}_{x_3} + \Big(v(s,t) \\
&+y_3 + x_3\left(\theta'(s)v(s,t) + \phi(s,t)\right) + y_3\Big( -\frac{1}{2}v'(s,t)^2 - \frac{1}{2}\left(\theta'(s)v(s,t) + \phi(s,t)\right)^2\Big)\Big)\mathbf{e}_{y_3} \\
&+\Big(w(s,t) + x_3\theta'(s)w(s,t) - x_3u'(s,t) - y_3v'(s,t) - x_3v'(s,t)\left(\theta'(s)v(s,t) + \phi(s,t)\right) \\
&+y_3\left(u'(s,t) - \theta'(s)w(s,t)\right)\left(\theta'(s)v(s,t) + \phi(s,t)\right)\Big)\mathbf{e}_{z_3}
\end{aligned} \tag{7.6}$$

Kaza and Kvaternik [51] had derived the equations of motion by transforming all the coordinate systems to the coordinate system 6, $(x_6, y_6, z_6)$, which introduced complicated expressions in their derivations. In this work, however, we express $\mathbf{r}_0$ and $\mathbf{r}_1$ and the subsequent quantities in the coordinate system 3, i.e., $(x_3, y_3, z_3)$, by using the previously defined transformation matrices. We approximated the trigonometric terms in Eqn. (7.3) up to quadratic nonlinearity. Therefore, we obtain relatively non-complicated expressions to describe the position vectors in coordinate system 3 (Eqns. (7.5) and (7.6)). For simplicity we are henceforth dropping the subscript "3" on $x_3, y_3, z_3$ terms and basis vectors in the equations.

**Energy Derivations** We apply an energy method to derive the governing equations of a curved beam under arbitrary deformations. $\mathbf{r}_0$ and $\mathbf{r}_1$ are the positions of an arbitrary point in the airfoil cross section before and after deformation, respectively,

The strain and kinetic energies are defined in terms of deformations and their derivatives with respect to the axis "$s$" along the blade. The strain energy of the blade is described in terms of Lagrangian strain terms. To calculate the Lagrangian strain components, Green's

strain formula [4, 25, 65] is applied using the differentials of $\mathbf{r}_0$ and $\mathbf{r}_1$, with respect to $x$, $y$, and $z$, using equations (7.5) and (7.6), noting that $d\mathbf{R}_0 = \mathbf{0}$, leading to

$$d\mathbf{r}_1 \cdot d\mathbf{r}_1 - d\mathbf{r}_0 \cdot d\mathbf{r}_0 = 2 \begin{bmatrix} dx & dy & dz \end{bmatrix} [\epsilon_{ij}] \begin{Bmatrix} dx \\ dy \\ dz \end{Bmatrix}, \tag{7.7}$$

where $[\epsilon_{ij}]$ is the Lagrangian strain tensor consisting of Green's strains. Using Eqns. (7.5) and (7.6),

$$\begin{aligned} d\mathbf{r}_0 &= \Big(\frac{dr_{0_x}(s)}{ds}\mathbf{e}_x + \frac{dr_{0_y}(s)}{ds}\mathbf{e}_y + \frac{dr_{0_z}(s)}{ds}\mathbf{e}_z\Big)ds + \\ &\Big(r_{0_x}(s)\frac{d\mathbf{e}_x}{ds} + r_{0_y}(s)\frac{d\mathbf{e}_y}{ds} + r_{0_z}(s)\frac{d\mathbf{e}_z}{ds}\Big)ds + dx\mathbf{e}_x + dy\mathbf{e}_y \\ d\mathbf{r}_1 &= \Big(\frac{dr_{1_x}(s)}{dx}\mathbf{e}_x + \frac{dr_{1_y}(s)}{dx}\mathbf{e}_y + \frac{dr_{1_z}(s)}{dx}\mathbf{e}_z\Big)dx + \\ &\Big(\frac{dr_{1_x}(s)}{dy}\mathbf{e}_x + \frac{dr_{1_y}(s)}{dy}\mathbf{e}_y + \frac{dr_{1_z}(s)}{dy}\mathbf{e}_z\Big)dy + \\ &\Big(\frac{dr_{1_x}(s)}{ds}\mathbf{e}_x + \frac{dr_{1_y}(s)}{ds}\mathbf{e}_y + \frac{dr_{1_z}(s)}{ds}\mathbf{e}_z + r_{1_x}(s)\frac{d\mathbf{e}_x}{ds} + r_{1_y}(s)\frac{d\mathbf{e}_y}{ds} + r_{1_z}(s)\frac{d\mathbf{e}_z}{ds} + \mathbf{e}_z\Big)ds. \end{aligned} \tag{7.8}$$

Here $z$ is for $z_3$, and is locally aligned with $s$, such that $dz = ds$. Also, since the cross section is considered to be rigid, we have $dx = dy = 0$. In taking derivatives of the unit vectors with respect to space, we use $\Omega_s = (-\theta_0' \sin\gamma)\mathbf{e}_x + (-\theta_0' \cos\gamma)\mathbf{e}_y + (\gamma')\mathbf{e}_z$, where $()' = d()/ds$. Then

$$\begin{aligned} \frac{d\mathbf{e}_x}{ds} &= \Omega_s \times \mathbf{e}_x = \theta' \cos\gamma e_z + \gamma'\mathbf{e}_y \\ \frac{d\mathbf{e}_y}{ds} &= \Omega_s \times \mathbf{e}_y = -\theta' \sin\gamma\mathbf{e}_z - \gamma'\mathbf{e}_x \\ \frac{d\mathbf{e}_z}{ds} &= \Omega_s \times \mathbf{e}_z = \theta' \sin\gamma\mathbf{e}_y - \theta' \cos\gamma\mathbf{e}_x. \end{aligned} \tag{7.9}$$

We find the Lagrangian strain elements by applying Eqns. (7.8) and (7.9) to Eqn. (7.7). On approximation, for the case that pretwist is zero ($\gamma = 0$ and $\gamma' = 0$), when the torsional shear strain is zero, $\epsilon_{zx} = \epsilon_{zy} = 0$, and $\phi \equiv 0$ (thus $\phi' = 0$) by definition. Then from

Eqn. (7.10) we have $\aleph' = v'\theta'$, which defines the shearless natural torsion angle (implying $\aleph = \aleph_0 + \int v'(s)\theta'(s)ds$). $\aleph$ is thus eliminated, and finally, the Lagrangian strains are

$$\begin{aligned}
\epsilon_{zx} &= -\frac{1}{2}y\phi'(s,t) \\
\epsilon_{zy} &= \frac{1}{2}x\phi'(s,t) \\
\epsilon_{zz} &= (1+x\theta'(s))(u(s,t)\theta'(s) - y\phi(s,t)\theta'(s) - yv(s,t)\theta'(s^2) + xw(s,t)\theta''(s) + \\
&\quad w'(s,t) + x\theta'(s)w'(s,t) - xu''(s,t) - yv''(s,t)).
\end{aligned} \tag{7.10}$$

For a rigid cross section in the $x, y$ plane, a "lower-order" modeling assumption, $\epsilon_{xx} = \epsilon_{yy} = \epsilon_{xy} = 0$. The strain energy is obtained using

$$V_s = \frac{1}{2}\int_{-S}^{S}\int_A \underline{\sigma\epsilon} dA ds, \tag{7.11}$$

where

$$\begin{aligned}
\underline{\sigma} &= \begin{bmatrix} \sigma_{xx} & \sigma_{yy} & \sigma_{zz} & \tau_{xy} & \tau_{xz} & \tau_{yz} \end{bmatrix} \\
\underline{\epsilon}^T &= \begin{bmatrix} \epsilon_{xx} & \epsilon_{yy} & \epsilon_{zz} & \gamma_{xy} & \gamma_{xz} & \gamma_{yz} \end{bmatrix}
\end{aligned}$$

contain stress and strain elements, where $\gamma_{ij} = 2\epsilon_{ij}$. The $\epsilon_{ij}$ are the "Lagrangian strains" and $\gamma_{ij}$ are the "engineering shear strains" [51, 65].

For an isotropic material with linear elasticity, Hooke's law states that $\sigma_{ij} = E\epsilon_{ij}$ and $\tau_{ij} = G\gamma_{ij}$. Then

$$V_s = \frac{1}{2}\int_{-S}^{S}\int_A (E\epsilon_{zz}^2 + 4G(\epsilon_{xz}^2 + \epsilon_{zy}^2))dA ds, \tag{7.12}$$

where $E$ is the Young's modulus and $G$ is the shear modulus. We substituted Eq. (7.10) into Eq. (7.12), and then used thin beam approximations to eliminate the $dA$ integration. For example the integration term $\int_{-S}^{S}\int_A y^2 z_0^2 \theta'(s)^6 dA ds = \int_{-S}^{S} I_x z_0^2 \theta'(s)^6 ds$ since $I_x = \int_A y^2 dA$. This is also part of the low-order modeling approximation.

The kinetic energy is

$$T = \frac{1}{2}\int_{-S}^{S}\int_A \rho \frac{d\mathbf{r}_1}{dt}\cdot\frac{d\mathbf{r}_1}{dt} dA ds, \tag{7.13}$$

where $d\mathbf{r}_1/dt$ is obtained from Eq. (7.6), $\dot{\mathbf{e}}_{j_3} = \underline{\omega}_T \times \mathbf{e}_{j_3}$, for $j = x, y, z$, and $\dot{\mathbf{R}}_0 = \underline{\omega}_T \times \mathbf{R}_0$, where $\mathbf{R}_0 = (x_0 \cos\theta + z_0 \sin\theta)\mathbf{e}_{x_3} + (z_0 \cos\theta - x_0 \sin\theta)\mathbf{e}_{z_3}$ in the $\mathbf{e}_3$ system, and where $\underline{\omega}_T$ is the total angular velocity vector of the rotor due to spin and other dynamic rotations if applicable. For the special case of $\underline{\omega}_T = \Omega\mathbf{e}_{z_0}$, i.e. spin on a fixed platform, we have $\dot{\mathbf{R}}_0 = x_0\Omega\mathbf{e}_{y_0}$.

Again using thin beam ("low-order") approximations eliminated the integration on $dA$. Writing $\mathbf{r}_1$ in terms of the displacement variables and using the beam cross sectional properties leads to kinetic energy integrals in $ds$ in terms of the displacement variables and their derivatives. Thus we have the form $V_s = \int_{-S}^{S} \hat{V}_s ds$ and $T_s = \int_{-S}^{S} \hat{T}_s ds$, where the strain energy density ($\hat{V}_s$) and kinetic energy density ($\hat{T}_s$) for the case of a fixed platform (where $\underline{\omega}_T = \Omega\mathbf{e}_{z_0}$) are expressed in Appendix 8.3 where we have kept expressions only up to quadratic terms.

The distributed nonconservative force vector per unit length is denoted by $\mathbf{f}(s,t)$, and can accommodate damping and aeroelasticity. The nonconservative virtual work density can be written as $\delta\hat{W}(s,t) = \mathbf{f}(s,t) \cdot \delta\mathbf{r}_1$ where $\delta\mathbf{r}_1$ is the generalized virtual displacement of any point in the domain.

**Euler-Lagrange Equation for Continuous Systems, Boundary Value Problem** Hamilton's principle is performed to obtain the governing equations of motion which can be express in the form [67]

$$\int_{t_1}^{t_2} (\delta T + \delta W) dt = 0, \tag{7.14}$$

where $\delta y = 0, -S \leq s \leq S$, at $t = t_1, t_2$ and $t_1$ and $t_2$ are arbitrary times. Introducing the energy densities into Eqn. (7.14) we obtain

$$\int_{t_1}^{t_2} \int_{-S}^{S} (\delta\hat{L} + \delta\hat{W}_{nc}) ds dt = 0. \tag{7.15}$$

If the Lagrangian density has the form $\hat{L} = \hat{T} - \hat{V} = \hat{L}(y, y', y'', \dot{y}, \dot{y}')$, then from Eqn. (7.15), the Lagrange differential equation of motion for continuous systems [67] is obtained as

$$\frac{\partial \hat{L}}{\partial y} - \frac{d}{dt}\left(\frac{\partial \hat{L}}{\partial \dot{y}}\right) - \frac{d}{ds}\left(\frac{\partial \hat{L}}{\partial y'}\right) + \frac{d^2}{ds^2}\left(\frac{\partial \hat{L}}{\partial y''}\right) + \frac{d^2}{ds^2}\left(\frac{\partial \hat{L}}{\partial \dot{y}'}\right) + f = 0, \tag{7.16}$$

where dots denote partial derivatives with respect to time and primes denote partial derivatives with respect to $s$. We use $u, v, w$ and $\phi$ in place of $y$ in Eqn. (7.16) to obtain the four partial differential equations.

In our problem the Lagrangian density is a function of $u, v, w$, and $\phi$, and their temporal and spatial derivatives. As such, using the Euler-Lagrange equations for the partial differential equations the resulting PDEs represent a uniform curved blade for which the centroid and shear center coincide, in the absence of gravity and spin.

**Discretization and Modal Analysis** From this point we can apply the extended Hamilton's principal or the Lagrangian equations for continuous systems [67] to obtain partial differential equations of motion, and the discretize the PDEs using a Galerkin projection on "assumed odes" or chosen basis functions. Alternatively, we apply "assumed modes" to the energy expressions. The continuous displacement variables are approximated as linear combinations of admissible functions, $\psi_j(s)$, as

$$\begin{aligned} u(s,t) &\approx \sum_{i=1}^{N} \psi_{ui}(s) q_{ui}(t), \quad v(s,t) \approx \sum_{i=1}^{N} \psi_{vi}(s) q_{vi}(t), \\ w(s,t) &\approx \sum_{i=1}^{N} \psi_{wi}(s) q_{wi}(t), \quad \phi(s,t) \approx \sum_{i=1}^{N} \psi_{\phi i}(s) q_{\phi i}(t). \end{aligned} \tag{7.17}$$

For the case where we use $N$ basis functions for each variable. In matrix form we have

$$\mathbf{y}(s,t) = \begin{Bmatrix} u(s,t) \\ v(s,t) \\ w(s,t) \\ \phi(s,t) \end{Bmatrix} \cong \begin{Bmatrix} \psi_u^T \mathbf{q}_u(t) \\ \psi_v^T \mathbf{q}_v(t) \\ \psi_w^T \mathbf{q}_w(t) \\ \psi_\phi^T \mathbf{q}_\phi(t) \end{Bmatrix} \cong \begin{bmatrix} \psi_u^T & 0 & 0 & 0 \\ 0 & \psi_v^T & 0 & 0 \\ 0 & 0 & \psi_w^T & 0 \\ 0 & 0 & 0 & \psi_\phi^T \end{bmatrix} \begin{Bmatrix} \mathbf{q}_u(t) \\ \mathbf{q}_v(t) \\ \mathbf{q}_w(t) \\ \mathbf{q}_\phi(t) \end{Bmatrix} = \boldsymbol{\psi}\mathbf{q}(t). \tag{7.18}$$

where $\psi_j$ are $1 \times N$ matrices, and $\boldsymbol{\Psi}(s)$ is an $M \times MN$ matrix, where $M = 4$ is number of continuous variables, and $\mathbf{q}$ is an $MN$-vector of assumed modal coordinates.

Using Eqn. (7.18) in the energy expressions, the kinetic and potential energies have the form $T = \frac{1}{2}\sum_{i=1}^{n}\sum_{j=1}^{n} m_{ij}\dot{q}_i\dot{q}_j$ and $V = \frac{1}{2}\lambda^2\sum_{i=1}^{n}\sum_{j=1}^{n} k_{ij}q_iq_j$. Standard Lagrange's equations are applied on these generalized coordinates. For nonconservative forces, the generalized forces $Q_i$ can be obtained from $\delta q_i$ as $\delta W = \sum_i \delta q_i \int_{-S}^{S} f(s,t)\psi_i(s)ds = \sum_i \delta q_i Q_i$. We apply the Lagrange's equation to find the differential equations of motion in modal coordinates $q_u, q_v, q_w$ and $q_\phi$, which represent $u, v, w$ and $\phi$, as

$$\begin{bmatrix} \mathbf{M}^{uu} & \mathbf{M}^{uv} & \mathbf{M}^{uw} & \mathbf{M}^{u\phi} \\ \mathbf{M}^{vu} & \mathbf{M}^{vv} & \mathbf{M}^{vw} & \mathbf{M}^{v\phi} \\ \mathbf{M}^{wu} & \mathbf{M}^{wv} & \mathbf{M}^{ww} & \mathbf{M}^{w\phi} \\ \mathbf{M}^{\phi u} & \mathbf{M}^{\phi v} & \mathbf{M}^{\phi w} & \mathbf{M}^{\phi\phi} \end{bmatrix} \begin{Bmatrix} \ddot{\mathbf{q}}_u \\ \ddot{\mathbf{q}}_v \\ \ddot{\mathbf{q}}_w \\ \ddot{\mathbf{q}}_\phi \end{Bmatrix} + \begin{bmatrix} \mathbf{K}^{uu} & \mathbf{K}^{uv} & \mathbf{K}^{uw} & \mathbf{K}^{u\phi} \\ \mathbf{K}^{vu} & \mathbf{K}^{vv} & \mathbf{K}^{vw} & \mathbf{K}^{v\phi} \\ \mathbf{K}^{wu} & \mathbf{K}^{wv} & \mathbf{K}^{ww} & \mathbf{K}^{w\phi} \\ \mathbf{K}^{\phi u} & \mathbf{K}^{\phi v} & \mathbf{K}^{\phi w} & \mathbf{K}^{\phi\phi} \end{bmatrix} \begin{Bmatrix} \mathbf{q}_u \\ \mathbf{q}_v \\ \mathbf{q}_w \\ \mathbf{q}_\phi \end{Bmatrix} = \begin{Bmatrix} \mathbf{Q}_u \\ \mathbf{Q}_v \\ \mathbf{Q}_w \\ \mathbf{Q}_\phi \end{Bmatrix} \tag{7.19}$$

or $\mathbf{M}\ddot{\mathbf{q}} + \mathbf{K}q = \mathbf{0}$ for the case of stationary (non rotating) blade and small oscillations. Matrices $\mathbf{M}$ and $\mathbf{K}$ are symmetric and have block-coupling properties. If we include rotation we expect gyroscopic terms $\mathbf{G}\dot{q}$ from the kinetic energy and the addition of centripetal terms in $\mathbf{K}$. Nonlinear and parametric aeroelastic terms would be formulated through the $\mathbf{Q}$ vector. For the case of large-strain nonlinearity, the strain expressions become very complicated.

With these equations, analyses (linear modal, state-variable modal, nonlinear response) can be conducted for the problem of interest (stationary, spinning, wind-excite, etc.).

| Properties | |
|---|---|
| Total mass | $3112\frac{kg}{m}$ |
| G | $26Gpa$ |
| E | $69Gpa$ |
| Cross section area | $1m^2$ |
| L | $100.53m$ |
| R | $32m$ |
| $I_{xx}$ | $\frac{1}{3}m^4$ |
| $I_{yy}$ | $208 \times 10^{-4}m^4$ |
| Blade material | $6063 - T6$ Aluminum alloy |

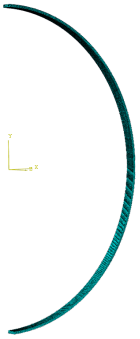

Figure 7.3: Half-circular slender beam with a rectangular cross section.

Table 7.1: Natural frequencies of a uniform half-circular curved beam with the pin-pin boundary conditions ($\frac{rad}{s}$).

| Mode | Assumed modes method† | Yang et al. [a] | Finite Element [b] |
|---|---|---|---|
| 1 | 0.3414 | 0.134 | 0.2344 |
| 2 | 0.6877 | – | 0.6054 |
| 3 | 0.8381 | 0.645 | 0.7157 |
| 4 | 1.6082 | 1.403 | 1.4447 |
| 5 | 2.05353 | – | 1.7795 |
| 6 | 2.5548 | 2.344 | 2.3575 |
| 7 | 3.7489 | 3.5317 | 3.5042 |
| 8 | 4.4338 | – | 3.8138 |
| 9 | 5.1266 | 4.8998 | 4.8295 |
| 10 | 6.7522 | 6.515 | 6.3876 |

†Present Result. [a]Ref. [118]. [b]Abaqus.

## 7.2 Modal Analysis and Behavior

We sketch the modal analysis process. For the fixed rotor, we take $\mathbf{Q} = 0$ and seek harmonic solutions of the form $\mathbf{q}_j = e^{i\omega_j t}\mathbf{p}_j$ which results in an eigenvalue problem (EVP) of the form

$$(\mathbf{K} - \omega^2\mathbf{M})\mathbf{p} = 0, \tag{7.20}$$

where $\mathbf{p}$ is the eigenvector and $\mathbf{P} = \begin{bmatrix}\mathbf{p}_1 & \mathbf{p}_2 \dots \mathbf{p}_{4N}\end{bmatrix}$ is the matrix of the eigenvectors. Letting $\mathbf{q} = \mathbf{P}\mathbf{a}(t)$, then $\mathbf{a}(t)$ is the modal coordinate vector that decouples the discretized

$\mathbf{q}$ system. Substituting $\mathbf{q}$ into Eqn. (7.18), the deformation variables are represented as $\mathbf{y}(s,t) = \mathbf{\Psi}(s)\mathbf{P}\mathbf{a}(t)$ in the new decoupled modal coordinates, $\mathbf{a}$. So, the approximated modal function vectors are the columns of the $\mathbf{W}(s) = \mathbf{\Psi}(s)\mathbf{P}$, which is an $M \times MN$ matrix representing the normal modes of vibration (the approximated mode shapes). Each column of $\mathbf{W}(s)$ is a vector whose elements are functions representing the mode shapes of the associated displacement variables, $u$, $v$, $w$, and $\phi$.

The assumed modes method is applied to a slender beam with a half circular profile and a rectangular cross section. The 3D configuration and properties of the blade are shown in Fig. 7.3. For a limited number of assumed modes the modal functions and modal frequencies are obtained. A finite-element analysis (FEA) is performed using Abaqus. The analyses are conducted for two different boundary conditions, pin-pin and clamp-clamp, and the results are compared with Abaqus and with Yang et al. [118], the latter of which only included in-plane deflections.

### 7.2.1 Modal Analysis of the Curved Beam with Pin-Pin Boundary Condition

The assumed modes method is applied to a uniform slender beam with circular geometry, and both hinged-hinged and clamped-clamped boundary conditions. ("Hinged-hinged" means that the in-plane flatwise flexure is pinned, but the out-of-plane edgewise flexure has a clamped boundary condition, such as a single-axis hinge.) The axial and torsional deformations are not considered "clamped", but rather "pinned", due to the lower order of the associated PDEs. The trial functions are assumed to be a uniform straight beam mode as follows

$$\psi_{ui} = \psi_{wi} = \psi_{\phi i} = \sin(\frac{n\pi}{L})s. \tag{7.21}$$

$$\psi_{vi} = -\cos\left(\frac{\lambda_n}{L}s\right) + \cosh\left(\frac{\lambda_n}{L}s\right) + \frac{(\cosh\lambda_n - \cos\lambda_n)\sin\left(\frac{\lambda_n}{L}s\right)}{\sinh\lambda_n - \sin\lambda_n} - \frac{(\cosh\lambda_n - \cos\lambda_n)\sinh\left(\frac{\lambda_n}{L}s\right)}{\sinh\lambda_n - \sin\lambda_n} \tag{7.22}$$

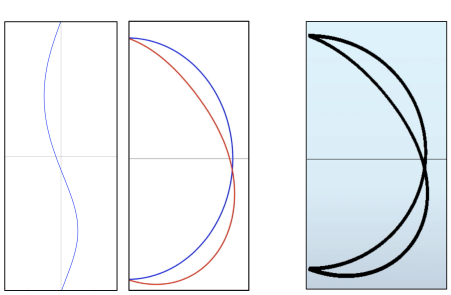

(a) Mode one, flatwise.

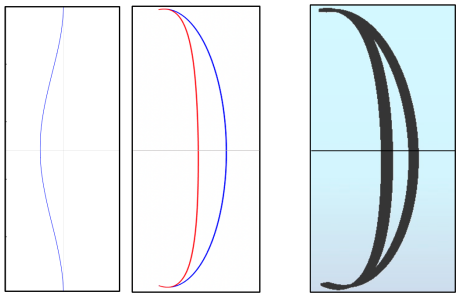

(b) Mode two, edgewise.

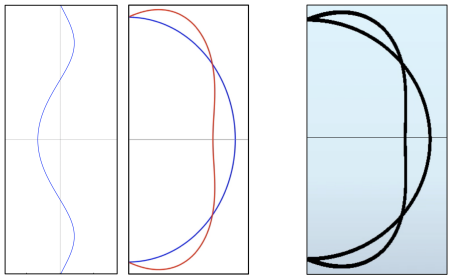

(c) Mode three, flatwise.

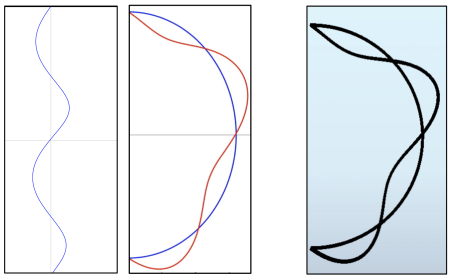

(d) Mode four, flatwise.

Figure 7.4: The first four vibration mode shapes of a uniform circular curved beam with pinned-pinned boundary conditions. Each mode is represented with three plots: the slender-beam mode shape as a function of $s$ on the vertical axis, the slender-beam mode shape shown about the undeformed curved-beam configuration, and the mode-shape about the undeformed beam generated using Abaqus. Mode two is shown with an angled view of the out-of-plane edgewise deflection.

The first 10 natural frequencies were obtained and compared with the FEA numerical results, and results from Yang et al. [118] on the in-plane vibrations of a general curved beam, in which they provided the partial differential equations (PDEs) of motion, and made estimations of modal frequencies Comparing both models shows that although the PDEs in Appendix D have a few extra terms compared to those of Yang et al. [118], the results from models confirm one another. Table 7.1 shows the first 10 modal frequencies from our modeling approach on the pinned-pinned case, results obtained by Ref. [118], and numerical results by FEA. As shown in the table, the first modal frequency has significant deviation among the three methods, and agreement improves as the modal frequencies increase. For higher modes the modal frequencies of both methods converge and they have an error $< 3\%$.

The associated mode shapes for the first four modal frequencies are illustrated in Fig. 7.4. The mode shapes are computed using $\mathbf{W}(s) = \mathbf{\Psi}(s)\mathbf{P}$ as functions of the axial variable $s$, and then are mapped onto the curved beam for visualization. Panels present the modal functions versus the $s$ coordinate on the vertical axis (left plots), the mode shapes mapped onto the curved beam (middle plots), and the FEA (Abaqus) results (right plots) for the validation. The plots demonstrate close agreement between the assumed modes method and the FEA results. Modes $1, 3$, and $4$ involve the flatwise bending and axial extension, and mode 2 involves the edgewise bending and twist.

### 7.2.2 Modal Analysis of the Curved Beam with Clamped-Clamped Boundary Condition

The assumed modes method is applied on a beam with clamped-clamped boundary conditions where the trial function are assumed to be uniform straight beam mode, as follows:

$$\psi_{wi} = \psi_{\phi i} = \sin(\frac{n\pi}{L})s. \tag{7.23}$$

$$\psi_{ui} = \psi_{vi} = -\cos\left(\frac{\lambda_n}{L}s\right) + \cosh\left(\frac{\lambda_n}{L}s\right) + \frac{(\cosh\lambda_n - \cos\lambda_n)\sin\left(\frac{\lambda_n}{L}s\right)}{\sinh\lambda_n - \sin\lambda_n} - \frac{(\cosh\lambda_n - \cos\lambda_n)\sinh\left(\frac{\lambda_n}{L}s\right)}{\sinh\lambda_n - \sin\lambda_n} \tag{7.24}$$

Application of basis functions with hyperbolic functions can be problematic and sensitive to numerical instabilities, especially for higher modes. If such problems are encountered, it is useful to use numerically stable representations of the functions.

Table 7.2 presents the first 10 modal frequencies using assumed modes method applied to the thin-beam model and compares them with the frequencies acquired by results published in Ref. [118] and the numerical results from FEA. Once again the three sets of results are in good agreement. It also restates that for lower modal frequencies the assumed modes method is more accurate.

Table 7.2: Natural frequencies of a uniform half-circular curved beam with the clamp-clamp boundary conditions ($\frac{rad}{s}$).

| Mode | Assumed modes method[†] | Yang et al. [a] | Finite Element [b] |
|---|---|---|---|
| 1 | 0.4615 | 0.3882 | 0.4504 |
| 2 | 0.6877 | – | 0.6167 |
| 3 | 1.0165 | 0.9353 | 0.9911 |
| 4 | 1.8884 | 1.8142 | 1.8114 |
| 5 | 2.0535 | – | 1.8404 |
| 6 | 2.899 | 2.8342 | 2.8235 |
| 7 | 4.1948 | 4.142 | 3.8791 |
| 8 | 4.4338 | – | 4.0817 |
| 9 | 5.6385 | 5.599 | 5.4771 |
| 10 | 7.3671 | 7.3456 | 6.8423 |

[†]Present Result. [a]Ref. [118]. [b]Abaqus.

Figure 7.5 shows the first four mode shapes for the curved beam with clamped-clamped boundary condition. The panels are comparing the original mode shapes, the mode shapes mapped on the curved beam, and the FEA results and representing that the results confirms each other. In modes $1, 3$ and 4 the flatwise bending coupled with the axial extension are dominant and in modes 2 the edgewise bending and twist are substantial.

## 7.3 Summary

In the interest of curved Darrieus wind-turbine blades, the governing equations of the vibration of a curved slender beam were derived using fundamental deformation mechanics under four coupled deformation variables: flatwise and edgewise bending, axial extension, and twist about the shear center. In the curved configuration we described the position of an arbitrary point on the cross section of the blade before and after deformation as $\mathbf{r}_0$ and $\mathbf{r}_1$, respectively. Green's strain formula was applied to the differential of $\mathbf{r}_0$ and $\mathbf{r}_1$ and the Lagrangian strains were found. Thin beam approximations were employed to express the strain and kinetic energies per unit length.

The assumed-modes method was applied to the energies, and the energy terms were

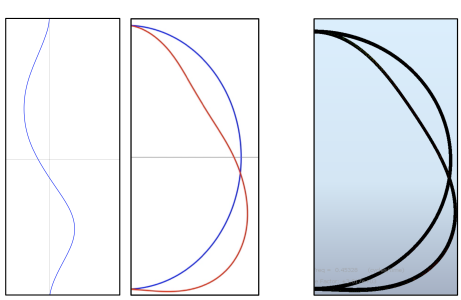

(a) Mode one, flatwise.

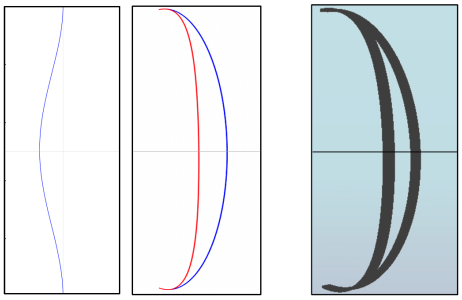

(b) Mode two, edgewise.

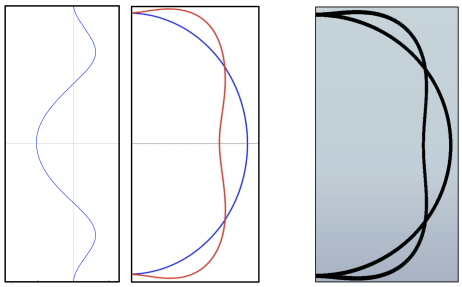

(c) Mode three, flatwise.

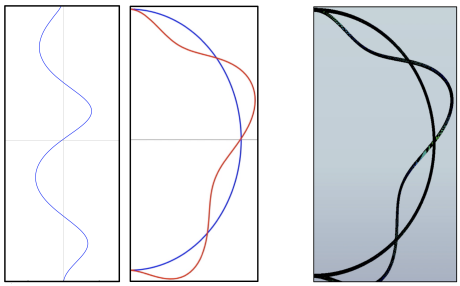

(d) Mode four, flatwise.

Figure 7.5: The first four vibration mode shapes of a uniform circular curved beam with clamped-clamped boundary condition. Each mode is represented with three plots: the slender-beam mode shape as a function of $s$ on the vertical axis, the slender-beam mode shape shown about the undeformed curved-beam configuration, and the mode-shape about the undeformed beam generated using Abaqus. Mode two is shown with an angled view of the out-of-plane edgewise deflection.

expressed in terms of the assumed modal coordinates. The Euler-Lagrange equation was used to discretize the equations of motion. Implementing the modal analysis to these equations, modal frequencies and mode shapes were found. This analysis was conducted for pinned-pinned and clamped-clamped boundary conditions.

In order to uphold the developed thin-beam and assumed-modes method, a finite-element analysis was applied on the beam with the same properties. The results obtained from the assumed modes method were in agreement with those from FEA drawn by Abaqus.

The low-order (thin-beam) model and results of modal analysis will be helpful when nonlinearities or applied loads are added, in which modal projections will facilitate dynamic response analysis and parameter studies. The next studies will examine the effects of

aeroelastic forces, gravitational loading, and spin loading and stiffening on the dynamic responses and resonances of the system. Moreover, we will be poised to carry out the analysis on different profile geometries, and expand to floating offshore Darrieus VAWTs.

# CHAPTER 8

# CONCLUSION AND FUTURE WORK

## 8.1 Conclusion

In this research, we studied the vibration analysis of Darrieus wind turbine blades, a vertical axis wind turbine with curved or straight blades. We examined the parametric stability and response characteristics of the structure by solving its equations of motion. We investigated the modal analysis of the curved beam and obtained the mode shapes and modal frequencies. In chapter 2 a vibration model for an H-rotor/Giromill type VAWT under bend and twist deflections was formulated and energy equations for an Eulerian beam under transverse bend and twist deflections was obtained. The system was discretized using reduced order modeling with single assumed mode for each deformation variable. We then applied Lagrange's equation on the assumed modal coordinates to obtain two coupled differential equations of motion. The equations of motion involved external forces due to aero-dynamic forces on blades. The aero-dynamic model was derived based on quasi steady airfoil theory. Lift and drag forces and moments were formulated for an airfoil with changing angle of attack, where stall effects were neglected. The formulas were simplified to cubic order using Taylor series expansion. The resulting system had parametric and direct excitation due to varying flow magnitude and direction relative to blade.

In order to conduct a simple numerical analysis, the system was linearized assuming small deflections for bend and twist. Linearized equations of motion were derived for a specific blade. Referring to Sandia 17m VAWT, a hypothetical Giromill blade was defined for numerical analysis where natural frequencies of the blade for a non rotating system were found. The initial simulations showed that Giromill undergoes large static deflections if the blade length is too large (in the range of the egg-beater style Sandia 17-m reference turbine) when operating at nominal speeds for the Sandia 17-m system. As such we conducted a study of direct and parametric loads and static deflection components for a

variety of blade lengths. Sample cyclic responses were also included. Indeed, the natural frequency is dependent on the rotor speed. Given the parameters, the linearized model has a critical rotor speed at which the natural frequency is reduced to zero, accompanied by instability and unbounded static deflection. While this is linearized behavior, it clearly shows a range of unacceptable parameters, and designs should be made such that structural behavior is sound when operating at typical rotor speeds. The Giromill turbine must have a blade length, or a stiffening system, to keep the natural frequency sufficiently high during rotation.

In chapter 3, we followed up on chapter 2 to learn about the parametric excitation in the system, through damping coefficient. The harmonic balance method combined with Floquet theory was used to attain an analytical approximation to the response of the system. We assumed a truncated Floquet solution and applied the harmonic balance, which led to a relationship between Floquet exponents and the parameters. The exponents were then used to formulate the initial condition responses and their frequency content. The theoretical response of the system and the stability characteristics and their FFT plots were compared with the numerical results and the consistency of the responses for different sets of parameters were shown.

For the case when there was zero mean damping we captured a phenomenon called "coexistence". Coexistence has been recognized to occur when stability boundaries overlap such that the instability wedge disappears. We looked at additional features of coexistence and considered the effect of mean damping on coexistence. Addition of mean damping disrupted the coexistence features, and we quantified how this happens.

In chapter 4, we focused on parametrically excited systems with two-harmonic parametric excitation. The purpose of the work was to determine not only the stability regions but also the characteristics of the responses. We used the Floquet theory combined with harmonic balance to analyze our system. By extracting the Floquet exponents we obtained

information about the stability criteria and the relationship between the excitation frequency and the frequencies of the response.

Comparing analyses of ta wo-harmonic Mathieu equation with a standard Mathieu equation showed that the boundaries of the subharmonic instability do not change visibly. However, the primary and superharmonic wedges can have a remarkable change, either shrinking or enlarging, depending on the phase of the second harmonic of excitation.

By increasing the truncation order we captured more stability tongues for lower values of frequency. Stability diagrams as well as the response frequencies for two different truncation numbers indicated the influence of the order of truncation. The range of accuracy increases as the truncation $n$ increases. There may be a computational limit on $n$, however. We applied the truncated Floquet series expansion to a system with two-harmonic parametric damping and observed that the coexistence in single-harmonic parametric damping turns into a tongue of instability when a second harmonic is added, for the parameters studied.

In addition to aeroelastically induced parametric damping, it is known that aeroelastic effects can cause self-excitation in blades. To represent this in a simplified way, the aeroelastic self excitation was modeled with van-der-Pol-type nonlinearity. We studied the combined effect of parametric excitation and van der Pol nonlinearity, as both can induce instabilities and oscillations.

We studied the resonance of both a forced and unforced van der Pol equation with parametric damping. The first-order method of multiple scales and numerical solutions were used. The parametric damping with no external excitation demonstrated nonresonant and subharmonic resonance cases, where the system shows an oscillatory quasi-periodic behavior in the former case. In the latter resonance case, we found the steady-state amplitude versus the excitation frequency for different damping parameters. When $c_0 = -1$ (negative linear damping as with the van der Pol oscillator), the resonant response amplitude

increases with the parametric damping $c_1$. An increase in the mean value of damping $c_0$, however, decreases the response amplitude.

The dynamics of the amplitude and phase showed saddle-node bifurcations coinciding with phase locking, in which periodically whirling amplitude and phase (quasiperiodic oscillations) were replaced with a fixed steady-state amplitude and phase (periodic oscillations).

We then studied the van der Pol oscillator with both parametric and direct excitation. In the nonresonant case the parametric damping term does not contribute in the solvability condition and therefore it showed the same behavior as the forced van der Pol. The nonresonant system can exhibit the quenching phenomenon when the excitation through the direct forcing is sufficiently large.

The subharmonic resonance behavior was similar to that of the parametric excitation without direct excitation, except that the direct excitation terms complicate and distort the steady solutions. Increasing the parametric damping parameter, $c_1$, increases the steady-state amplitude, and the mean and cyclic direct forcing, $f_0$ and $f_1$, deformed the ellipse.

In addition to the nonresonant and subharmonic resonance, van der Pol oscillator with parametric and direct excitation experienced superharmonic resonance. It was shown that the amplitude of the response increases with parametric damping and direct forcing.

We studied the modal analysis of a half-circular curved Darrieus VAWT. Assumed-modes analysis was applied to find the modal frequencies and the mode shapes of the curved beam with desired boundary conditions at both ends attached to a rigid tower. For a pin-pin boundary condition, we used straight uniform beam modes as the assumed-modes. We performed a numerical simulation in Abaqus for the curved blade to achieve the numerical modal analysis. The theoretical frequency were compared with the numerical results attained by the Abaqus. Yang et al. [118] derived the equations of motion of a half-circular curved beam. Although our equations of motion have a few extra terms compared to Yang's

analysis, our assumed-modes analysis was consistent with their modal frequencies.

The analysis was repeated for the clamp-clamp boundary condition assuming straight beam model as the assumed-modes. The modal frequencies and modes shapes where obtained and verified by numerical results and also Yang's model.

For both boundary conditions, our model provided more accurate modal frequencies for lower frequencies, although for higher frequencies the results stayed quite close to the numerical results. The animated mode shapes demonstrate node points which moves along the blade. The lateral deflection united with the axial deflection could cause the periodic shifting of the "node points" in the node points. The modal frequencies converged as the number of assumed-modes increased and indicated that the higher frequencies require greater number of assumed-modes.

## 8.2 Research Contribution

In the study on the straight bladed Giromill, we will show that spin softening effects may be dangerous to the structure, and that aerodynamic effects may produce parametric damping and stiffness. These findings prompt subsequent studies in this work.

Our work on parametric damping is one of few such studies. It provides an application of the Floquet harmonic balance analysis method. We show effects of parametric damping on free vibration and stability. We also encounter "coexistence", and add some insight into this phenomenon.

The studies on combined parametric damping and parametric stiffness are also new. The analysis shows how these effects combine to influence stability and response characteristics.

The work on curved slender Darrieus blades is one few studies that analyze such structures using a low-order beam-based modeling approach. The work is grounded in fundamental mechanics of strain, and leads expressions of strain energy and kinetic energy, which then generate either a partial differential equation model, or a assumed-mode set of ordinary differential equations. Modal analysis of this model provides modes that can

be used in reduced-order models for the eventual study of the system with spin effects, aeroelastic excitation and floating-platform dynamics.

## 8.3 Ongoing and Future Work

Following the modal analysis in chapter 7, we will expand the analysis and will inquire into implementation of aeroelastic and gravitational loading on the curved structure and analyze the blade's dynamics. We will then proceed from the stationary rotor to a spinning rotor. Eventually the goal is to apply the assumed-modes beam-based method to a floating VAWT with the complex dynamics, considering tipping, spinning and rotation of the rotor. The model can be extended and investigate different blade profiles, either parabola, troposkien, straight-circular-straight, etc. It is expected that the blade shape will contribute to the stiffness of the structure and effect the modal responses.

Ongoing work includes more investigation on the dynamical systems with parametric excitation, in both stiffness and damping terms, with single and higher harmonics. The effect of relative amplitude and phase of the second harmonic, and more details on the effect of multiple harmonics in systems with parametric damping is examined. Studying a third harmonic ($3\omega$) of excitation in place of the $2\omega$ term may also make sense for physical applications.

For future work, vibration experiment could be designed to construct a system having parametric stiffness. For this purpose a concentrated mass will be attached to a string. One end of the string is clamped and the other end is attached to a shaker. The parametric excitation by a shaker causes a parametric term in stiffness term (as with the very well known second order differential equation, Mathieu's equation). The response of the system can be extracted and parametric estimation can be applied in order to obtain the parameters in the system, e.g., the amplitude of the parametric stiffness.

Our numerical studies on the van der Pol oscillator with parametric damping showed the primary resonance as a dominant forced response case. The analysis of this case requires

further investigation that will be done as a subsequent study with weak excitation. Based on previous studies on the cases with forcing and cyclic stiffness, we expect that a second-order multiple-scales analysis should be considered to correctly pull out the contribution of the parametric damping to the different resonance cases.

# BIBLIOGRAPHY


[1] Acar, G. D., M. A. Acar & B. F. Feeny. 2020. Parametric resonances of a three-blade-rotor system with reference to wind turbines. *Journal of Vibration and Acoustics* 142(2). 021013 (9 pages).

[2] Acar, Gizem & B. F. Feeny. 2016. Floquet-based analysis of general responses of the Mathieu equation. *Journal of Vibration and Acoustics* 138(4). 041017 (9 pages).

[3] Acar, Gizem & Brian F Feeny. 2016. Floquet-based analysis of general responses of the Mathieu equation. *Journal of Vibration and Acoustics* 138(4). 041017.

[4] Acar, Gizem D & Brian F Feeny. 2018. Bend-bend-twist vibrations of a wind turbine blade. *Wind Energy* 21(1). 15–28.

[5] Afzali, F., O. Kapucu & B. F. Feeny. 2016. Vibrational analysis of vertical-axis wind-turbine blades. In *Proceedings of the asme 2016 international design engineering technical conferences*, Charlotte, North Carolina. Paper number IDETC2016-60374.

[6] Afzali, Fatemeh, Gizem D Acar & Brian F Feeny. 2017. Analysis of the periodic damping coefficient equation based on floquet theory. In *Asme 2017 international design engineering technical conferences and computers and information in engineering conference*, V008T12A050–V008T12A050. American Society of Mechanical Engineers.

[7] Afzali, Fatemeh, Gizem D Acar & Brian F Feeny. 2020. A Floquet-based analysis of parametric excitation through the damping coefficient. *Journal of Vibration and Acoustics* 143(4).

[8] Afzali, Fatemeh & Brian F Feeny. 2020. Response characteristics of systems with parametric excitation through damping and stiffness. In *Asme international design engineering technical conferences and computers and information in engineering conference*, St. Louis: American Society of Mechanical Engineers. Paper number DETC2020-22457.

[9] Afzali, Fatemeh, Onur Kapucu & Brian F Feeny. 2016. Vibration analysis of vertical-axis wind-turbine blades. In *Asme 2016 international design engineering technical conferences and computers and information in engineering conference*, American Society of Mechanical Engineers.

[10] Alcoa Laboratories. 1979. Design and fabrication of a low cost Darrieus vertical axis wind turbine system, phase i. *Technical Report* ALO-4272. 1–236.

[11] Allen, Matthew S. 2007. Floquet experimental modal analysis for system identification of linear time-periodic systems. In *Asme 2007 international design engineering technical conferences and computers and information in engineering conference*, 823–833. American Society of Mechanical Engineers.

[12] Allen, Matthew S., Micheal W. Sracic, S. Chauhan & Morten Hartvig Hansen. 2011. Output-only modal analysis of linear time-periodic systems with application to wind turbine simulation data. *Mechanical Systems and Signal Processing* 25(4). 1174–1191.

[13] Arnold, V. I. 1978. *Mathematical methods of classical mechanics*. New York: Springer-Verlag.

[14] Ashwill, T. D. 1992. Measured data for the Sandia 34-meter vertical axis wind turbine. Tech. rep. Sandia National Laboratories Albuquerque, NM, and Livermore, CA. SAND91-2228.

[15] Barbosa, Ramiro S, JA Tenreiro Machado, BM Vinagre & AJ Calderon. 2007. Analysis of the van der pol oscillator containing derivatives of fractional order. *Journal of Vibration and Control* 13(9-10). 1291–1301.

[16] Barone, Matthew F & Joshua Paquette. 2012. Vertical-axis wind turbines revisited: A Sandia perspective. Tech. rep. Sandia National Laboratories.

[17] Beer, Ferdinand P, R Johnston, J Dewolf & D Mazurek. 1981. Mechanics of materials, mcgraw-hill. *New York* 150–233.

[18] Benaroya, Haym & Mark L Nagurka. 2011. *Mechanical vibration: Analysis, uncertainties, and control*. Englewood Cliffs: CRC Press.

[19] Benmeddour, A, A Wall, B McAuliffe, PJ Penna & JC Su. 2010. Overview of wind energy research and development at NRC-IAR (Canada). *Revue des Energies Renouvelables* 69–80.

[20] Cantero, Daniel, Anders Rønnquist & Arvid Naess. 2016. Recent studies of parametrically excited mooring cables for submerged floating tunnels. *Procedia Engineering* 166. 99–106.

[21] Caruntu, Dumitru I. 2009. On nonlinear forced response of nonuniform beams. In *Asme 2008 dynamic systems and control conference*, 403–408. American Society of Mechanical Engineers Digital Collection.

[22] Cesari, Lamberto. 2012. *Asymptotic behavior and stability problems in ordinary differential equations*, vol. 16. Springer Science & Business Media.

[23] Chiras, Dan. 2010. *Wind power basics: a green energy guide*. New Society Publishers.

[24] Council, Global Wind Energy. 2019. Global wind report annual market update. online. "http://www.gwec.net/global-figures/graphs/+".

[25] Crisfield, Michael A. 1993. *Non-linear finite element analysis of solids and structures*, vol. 1. Wiley.

[26] Dugundji, John & Vivekananda Mukhopadhyay. 1973. Lateral bending-torsion vibrations of a thin beam under parametric excitation. *Journal of Applied Mechanics* 40(3). 693–698.

[27] Eldridge, Frank R. 1975. *Wind machines: Report*, vol. 75 51. The Foundation.

[28] Energy, Wind. 2019. Global wind report annual market update. online. "http: www.windenergy-the-facts.org/fr/scenarios-and-targets/scenarios-and-targets+".

[29] Eriksson, Sandra, Hans Bernhoff & Mats Leijon. 2008. Evaluation of different turbine concepts for wind power. *renewable and sustainable energy reviews* 12(5). 1419–1434.

[30] Feeny, F., Brian. 2016. Lecture notes on theory of vibrations, .

[31] Fleming, PD & SD Probert. 1984. The evolution of wind-turbines: an historical review. *Applied energy* 18(3). 163–177.

[32] Fowler, Matthew, Diana Bull & Andrew Goupee. 2014. A comparison of platform options for deep-water floating offshore vertical axis wind turbines: an initial study. *Sandia Report, Sandia National Laboratories* .

[33] Fowler, Matthew J, Brian Owens, Diana Bull, Andrew J Goupee, John Hurtado, D Todd Griffith & Marco Alves. 2014. Hydrodynamic module coupling in the offshore wind energy simulation (owens) toolkit. In *Asme 2014 33rd international conference on ocean, offshore and arctic engineering*, V09BT09A027–V09BT09A027. American Society of Mechanical Engineers.

[34] Goswami, I., R. H. Scanlan & N. P. Jones. 1993. Vortex-induced vibration of circular cylinders. ii: New model. *Journal of Engineering Mechanics–ASCE* 119(11). 2288–2302.

[35] Guckenheimer, J. & P. Holmes. 1983. *Nonlinear oscillations, dynamical systems, and bifurcations of vector fields*. New York: Springer Verlag.

[36] Guennoun, K., M. Houssni & M. Belhaq. 2002. Quasiperiodic solutions and stability for a weakly damped nonlinear quasiperiodic Mathieu equation. *Nonlinear Dynamics* 27(3). 211–236.

[37] Ham, N. D. 1977. Flutter of darrieus wind turbine blades. Tech. rep. Wind Turbine Structural Dynamics. DOE Publications CONF-771148.

[38] Hartono & Adriaan Herman Pieter Burgh. 2002. *An equation time-periodic damping coefficient: Stability diagram and an application*. Delft University of Technology.

[39] Hartono & AHP van der Burgh. 2003. A linear differential equation with a time-periodic damping coefficient: stability diagram and an application. *Mekelweg 4, 2628 CD Delft, The Netherlands* .

[40] Holmes, P. J. & D. A. Rand. 1978. Bifurcations of the forced van der Pol oscillator. *Quarterly of Applied Mathematics* 35(4). 495–509.

[41] Horwitz, HT. 1933. On the advent, the first development and the propagation of windrades. *BGTI / TG* 22.

[42] Hsu, C S. 1965. Further results on parametric excitation of a dynamic system. *Journal of Applied Mechanics* 32(2). 373–377.

[43] Hsu, Chieh Su. 1972. Impulsive parametric excitation: theory. *Journal of Applied Mechanics* 39(2). 551–558.

[44] Hsu, CS. 1963. On the parametric excitation of a dynamic system having multiple degrees of freedom. *Journal of Applied Mechanics* 30(3). 367–372.

[45] Ince, EL. 1925. A linear differential equation with periodic coefficients. *Proceedings of the London Mathematical Society* 2(1). 56–74.

[46] Inoue, Tsuyoshi, Yukio Ishida & Takashi Kiyohara. 2012. Nonlinear vibration analysis of the wind turbine blade (occurrence of the superharmonic resonance in the out of plane vibration of the elastic blade). *Journal of Vibration and Acoustics* 134(3). 031009.

[47] Jacobs, Eastman N, Kenneth E Ward & Robert M Pinkerton. 1933. The characteristics of 78 related airfoil sections from tests in the variable-density wind tunnel .

[48] James, G. H., T. G. Carne & P. S. Veers. 1996. Damping measurements using operational data. *Journal of Solar Energy Engineering* 118(3). 190–193.

[49] Johansen, Jeppe. 1999. Unsteady airfoil flows with application to aeroelastic stability .

[50] Kaldellis, John K & Dimitris Zafirakis. 2011. The wind energy (r) evolution: A short review of a long history. *Renewable energy* 36(7). 1887–1901.

[51] Kaza, Krishna Rao V & Raymond G Kvaternik. 1979. Aeroelastic equations of motion of a darrieus vertical-axis wind-turbine blade .

[52] Klausmeier, Christopher A. 2008. Floquet theory: a useful tool for understanding nonequilibrium dynamics. *Theoretical Ecology* 1(3). 153–161.

[53] Kniffka, Till Jochen & Horst Ecker. 2015. Parametererregte mikroelektromechanische Systeme (MEMS). *e & i Elektrotechnik und Informationstechnik* 132(8). 456–461.

[54] Kuchment, Peter A. 2012. *Floquet theory for partial differential equations*, vol. 60. Birkhäuser.

[55] Ladson, Charles L, Cuyler W Brooks Jr, Acquilla S Hill & Darrell W Sproles. 1996. Computer program to obtain ordinates for naca airfoils .

[56] Larsen, Jesper Winther, Søren RK Nielsen & Steen Krenk. 2007. Dynamic stall model for wind turbine airfoils. *Journal of Fluids and Structures* 23(7). 959–982.

[57] Lenci, S, E Pavlovskaia, G Rega & M Wiercigroch. 2008. Rotating solutions and stability of parametric pendulum by perturbation method. *Journal of Sound and Vibration* 310(1-2). 243–259.

[58] Liang, Yang & BF Feeny. 2008. Parametric identification of a chaotic base-excited double pendulum experiment. *Nonlinear Dynamics* 52(1-2). 181–197.

[59] Lilien, Jean-Louis & A Pinto Da Costa. 1994. Vibration amplitudes caused by parametric excitation of cable stayed structures. *Journal of Sound and Vibration* 174(1). 69–90.

[60] Luongo, Angelo & Daniele Zulli. 2011. Parametric, external and self-excitation of a tower under turbulent wind flow. *Journal of Sound and Vibration* 330(13). 3057–3069.

[61] Magnus, Wilhelm & Stanley Winkler. 1979. *Hill's equation*. New York: Dover.

[62] Mandel'shtam, LI & ND Papaleksi. 1934. On the parametric excitation of electric oscillations. *Zhurnal teknicheskoy fiziki* 4(1). 1–47.

[63] solar lights manufacturer. 2019. solarlightsmanufacturer. online. http://www.solarlightsmanufacturer.com/vertical-and-horizontal-axis-wind-turbines/+.

[64] Manwell, James F, Jon G McGowan & Anthony L Rogers. 2010. *Wind energy explained: theory, design and application*. John Wiley & Sons.

[65] Mase, George Thomas & George E. Mase. 1999. *Continuum mechanics for engineers*. Boca Raton: CRC Press 2nd edn.

[66] Meirovitch, Leonard. 1967. *Analytical methods in vibrations*. New York: MacMillan.

[67] Meirovitch, Leonard. 1980. *Computational methods in structural dynamics*, vol. 5. Springer Science & Business Media.

[68] Meirovitch, Leonard. 1997. *Principles and techniques of vibrations*, vol. 1. Prentice Hall New Jersey.

[69] Month, L.A. & R. H. Rand. 1982. Bifurcation of 4-1 subharmonics in the nonlinear Mathieu equation. *Mechanics Research Communications* 9(4). 233–240.

[70] Moussa, Ridha. 2014. On the generalized ince equation .

[71] Musial, Walter & Bonnie Ram. 2010. Large-scale offshore wind power in the united states: Assessment of opportunities and barriers. Tech. rep. National Renewable Energy Lab.(NREL), Golden, CO (United States).

[72] Nayfeh, Ali H. 2008. *Perturbation methods*. New York: John Wiley & Sons.

[73] Nayfeh, Ali H & Dean T Mook. 2008. *Nonlinear oscillations*. New York: John Wiley & Sons.

[74] Ng, L. & R. H. Rand. 2002. Bifurcations in a Mathieu equation with cubic nonlinearities. *Chaos Solitons and Fractals* 14(2). 173–181.

[75] Ng, Leslie & Richard Rand. 2003. Nonlinear effects on coexistence phenomenon in parametric excitation. *Nonlinear Dynamics* 31(1). 73–89.

[76] Owens, Brian, John E Hurtado, Joshua A Paquette, Daniel T Griffith & Matthew F Barone. 2013. Aeroelastic modeling of large off-shore vertical-axis wind turbines: development of the offshore wind energy simulation toolkit. In *54th aiaa/asme/asce/ahs/asc structures, structural dynamics, and materials conference*, 1552.

[77] Owens, Brian C, D Todd Griffith & John E Hurtado. 2014. Modal dynamics and stability of large multi-megawatt deepwater offshore vertical-axis wind turbines: Initial support structure and rotor design impact studies. In *32nd asme wind energy symposium*, 0518.

[78] Owens, Brian C, John E Hurtado, Matthew Barone & Joshua A Paquette. 2013. An energy preserving time integration method for gyric systems: development of the offshore wind energy simulation toolkit. In *Proceedings of the european wind energy association conference & exhibition*, .

[79] Owens, Brian Christopher & D Todd Griffith. 2014. Aeroelastic stability investigations for large-scale vertical axis wind turbines. In *Journal of physics: Conference series*, vol. 524 1, 012092. IOP Publishing.

[80] Pandey, M., R. H. Rand & A. T. Zehnder. 2008. Frequency locking in a forced Mathieu-van-der-Pol-Duffing system. *Nonlinear Dynamics* 54(1-2). 3–12.

[81] Perret-Liaudet, Joël, Alexandre Carbonelli, Emmanuel Rigaud, Brice Nelain, Pascal Bouvet & C Jacques Vialonga. 2014. Modeling of gearbox whining noise. Tech. rep. SAE Technical Paper.

[82] Ramakrishnan, Venkatanarayanan. 2017. *Analysis of wind turbine blade vibration and drivetrain loads*. East Lansing: Michigan State University dissertation.

[83] Ramakrishnan, Venkatanarayanan & Brian F Feeny. 2011. In-plane nonlinear dynamics of wind turbine blades. In *Asme 2011 international design engineering technical conferences and computers and information in engineering conference*, 761–769. American Society of Mechanical Engineers.

[84] Ramakrishnan, Venkatanarayanan & Brian F Feeny. 2012. In-plane nonlinear dynamics of wind turbine blades. In *Asme 2011 international design engineering technical conferences and computers and information in engineering conference*, 761–769. American Society of Mechanical Engineers Digital Collection.

[85] Ramakrishnan, Venkatanarayanan & Brian F Feeny. 2012. Resonances of a forced Mathieu equation with reference to wind turbine blades. *Journal of Vibration and Acoustics* 134(6). 064501.

[86] Rand, Richard, Randolph Zounes & Rachel Hastings. 1999. Dynamics of a quasiperiodically-forced mathieu oscillator. In *Iutam symposium on new applications of nonlinear and chaotic dynamics in mechanics*, 61–70. Springer.

[87] Rand, Richard H. 1969. On the stability of Hill's equation with four independent parameters. *Journal of Applied Mechanics* 36(4). 885–886.

[88] Rand, Richard H. 2012. Lecture notes on nonlinear vibrations, https://ecommons.cornell.edu/handle/1813/28989, .

[89] Recktenwald, Geoffrey & Richard Rand. 2005. Coexistence phenomenon in autoparametric excitation of two degree of freedom systems. *International Journal of Non-Linear Mechanics* 40(9). 1160–1170.

[90] Rhoads, J. F. & S. W. Shaw. 2010. The impact of nonlinearity on degenerate parametric amplifiers. *Applied Physics Letters* 96(23). 234101.

[91] Rhoads, Jeffrey F, Nicholas J Miller, Steven W Shaw & Brian F Feeny. 2008. Mechanical domain parametric amplification. *Journal of Vibration and Acoustics* 130(6). 061006.

[92] Rhoads, Jeffrey F, Steven W Shaw, Kimberly L Turner, Jeff Moehlis, Barry E DeMartini & Wenhua Zhang. 2006. Generalized parametric resonance in electrostatically actuated microelectromechanical oscillators. *Journal of Sound and Vibration* 296(4-5). 797–829.

[93] Roscher, Bjoern. 2014. Structural optimization of a vertical axis wind turbine with aeroelastic analysis. *M. Sc, Wind Energy and Aerospace Engineering, Technical University of Denmark and Delft University of Technology., Denmark* .

[94] Samorani, Michele. 2013. The wind farm layout optimization problem. In *Handbook of wind power systems*, 21–38. Springer.

[95] Sapmaz, Ayse, Gizem D Acar & Brian Feeny. 2017. In-plane blade-hub dynamics of horizontal-axis wind turbine with mistuned blades. In *Asme 2017 international design engineering technical conferences and computers and information in engineering conference*, V008T12A033–V008T12A033. American Society of Mechanical Engineers.

[96] Sartorelli, Jose Carlos & Walter Lacarbonara. 2012. Parametric resonances in a base-excited double pendulum. *Nonlinear dynamics* 69(4). 1679–1692.

[97] Sevin, Eugene. 1961. On the parametric excitation of pendulum-type vibration absorber. *Journal of Applied Mechanics* 28(3). 330–334.

[98] Sheldahl, Robert E, Louis V Feltz & B Fv Blackwell. 1978. Wind tunnel performance data for two-and three-bucket savonius rotors. *Journal of Energy* 2(3). 160–164.

[99] Sofroniou, Anastasia & Steven Bishop. 2014. Dynamics of a parametrically excited system with two forcing terms. *Mathematics* 2(3). 172–195.

[100] South, Peter & Raj Rangi. 1973. performance and economics of the vertical-axis wind turbine developed at the national research council, ottawa, canada .

[101] South, Peter & Raj S Rangi. 1971. Preliminary tests of a high speed vertical axis windmill model .

[102] Sun, Xiaojing, Diangui Huang & Guoqing Wu. 2012. The current state of offshore wind energy technology development. *Energy* 41(1). 298–312.

[103] Sutherland, Herbert J, Dale E Berg & Thomas D Ashwill. 2012. A retrospective of vawt technology. *Sandia Report No. SAND2012-0304* .

[104] Szabelski, Kazimierz & Jerzy Warmiński. 1995. Parametric self-excited non-linear system vibrations analysis with inertial excitation. *International journal of non-linear mechanics* 30(2). 179–189.

[105] Taylor, James H & Kumpati S Narendra. 1969. Stability regions for the damped Mathieu equation. *SIAM Journal on Applied Mathematics* 17(2). 343–352.

[106] Thomas, Robert Nason. 2004. Coupled vortex vertical axis wind turbine. US Patent 6,784,566.

[107] Thomson, William. 1996. *Theory of vibration with applications*. Englewood Cliffs: CRC Press.

[108] Turrittin, HL. 1952. Asymptotic expansions of solutions of systems of ordinary linear differential equations containing a parameter. In *Contributions to the theory of nonlinear oscillations, vol. ii*, 81–116. Princeton University Press Princeton.

[109] van der Pol, B. 1934. The nonlinear theory of electrical oscillations. *Proc. IRE* 22(9). 1051–1086.

[110] Veerman, F. & F. Verhulst. 2009. Quasiperiodic phenomena in the van der Pol-Mathieu equation. *Journal of Sound and Vibration* 326(1-2). 314–320.

[111] Veers, Paul S. 1983. *A general method for fatigue analysis of vertical axis wind turbine blades*. Sandia National Laboratories.

[112] Ward, M. 2010. *Lecture notes on basic floquet theory*. http://www.emba.uvm.edu/ jxyang/teaching/.

[113] Warminski, Jerzy. 2020. Nonlinear dynamics of self-, parametric, and externally excited oscillator with time delay: van der pol versus rayleigh models. *Nonlinear Dynamics* 99(1). 35–56.

[114] Whittlesey, Robert W, Sebastian Liska & John O Dabiri. 2010. Fish schooling as a basis for vertical axis wind turbine farm design. *Bioinspiration & biomimetics* 5(3). 035005.

[115] Worstell, M. 1978. Aerodynamic performance of the 17 meter diameter darrieus wind turbine in the three-bladed configuration: An addendum. *Sandia National Laboratories Report, SAND79-173* .

[116] Worstell, Mark H. 1979. *Aerodynamic performance of the 17-metre-diameter darrieus wind turbine*. Department of Energy, Sandia Laboratories.

[117] Worstell, Mark H. 1980. Aerodynamic performance of the 17-m-diameter darrieus wind turbine in the three-bladed configuration: An addendum. *NASA STI/Recon Technical Report N* 80.

[118] Yang, F, R Sedaghati & E Esmailzadeh. 2008. Free in-plane vibration of general curved beams using finite element method. *Journal of sound and vibration* 318(4-5). 850–867.

[119] Yang, F., R. Sedaghati & E. Esmailzadeh. 2018. Free in-plane vibration of curved beam structures: A tutorial and the state of the art. *Journal of Vibration and Control* 24(12). 2400–2417.

[120] Younesian, D, E Esmailzadeh & R Sedaghati. 2005. Existence of periodic solutions for the generalized form of Mathieu equation. *Nonlinear Dynamics* 39(4). 335–348.

[121] Yu, RC & CD Mote Jr. 1987. Vibration and parametric excitation in asymmetric circular plates under moving loads. *Journal of Sound and Vibration* 119(3). 409–427.

[122] Zhang, Wen-Ming & Guang Meng. 2007. Nonlinear dynamic analysis of electrostatically actuated resonant mems sensors under parametric excitation. *IEEE Sensors Journal* 7(3). 370–380.

## APPENDIX

Euler Angles:

$$\sin\beta_x(s) = \frac{\partial v(s,t)}{\partial s} \tag{8.1}$$
$$\sin\beta_y(s) = \frac{\partial u(s,t)}{\partial s} - \frac{\partial \theta(s)}{\partial s} w(s,t)$$
$$\cos\beta_x(s) = 1 - \frac{1}{2}\left(\frac{\partial v(s,t)}{\partial s}\right)^2$$
$$\cos\beta_y(s) = 1 - \frac{1}{2}\left(\frac{\partial u(s,t)}{\partial s} - \frac{\partial \theta(s)}{\partial s} w(s,t)\right)^2$$
$$\sin(\beta_z(s,t)) = \beta_z(s,t)$$
$$\cos(\beta_z(s,t)) = 1 - \frac{1}{2}\beta_z(s,t)^2$$

Strain Components:

$$\epsilon_{zx} = \frac{1}{2}\left(-y\aleph'(s,t) + y\theta'(s)v'(s,t) - y\phi'(s,t)\right) \tag{8.2}$$
$$\epsilon_{zy} = \frac{1}{2}\left(x\aleph'(s,t) - x\theta'(s)v'(s,t) + x\phi'(s,t)\right)$$
$$\epsilon_{zz} = (1 + x\theta'(s))(-y\aleph(s,t)\theta'(s) + u(s,t)\theta'(s) - y\phi(s,t)\theta'(s) + xw(s,t)\theta''(s) + w'(s,t) + x\theta'(s)w'(s,t) - xu''(s,t) - yv''(s,t))$$

The Expressions for Potential and Kinetic Energies:

$$\begin{aligned}
\hat{V} &= AE\Big(\theta'(s)u(s,t) + w'(s,t)\Big)^2 + I_x(E\theta'(s)^2\phi(s,t)^2 \\
&+2E\theta'(s)\phi(s,t)\left(v''(s,t) + \theta'(s)^2 v(s,t)\right) \\
&+2E\theta'(s)^2 v(s,t)v''(s,t) + Ev''(s,t)^2 + E\theta'(s)^4 v(s,t)^2 + G\phi'(s,t)^2) \\
&+I_y\Big(-6E\theta'(s)u''(s,t)w'(s,t) + 2E\theta'(s)^2 u(s,t)(-2u''(s,t) + 3\theta'(s)w'(s,t) \\
&+2\theta''(s)w(s,t)) + 2E\theta''(s)w(s,t)\left(3\theta'(s)w'(s,t) - u''(s,t)\right) + G\phi'(s,t)^2 \\
&+Eu''(s,t)^2 + E\theta'(s)^4 u(s,t)^2 + 6E\theta'(s)^2 w'(s,t)^2 + E\theta''(s)^2 w(s,t)^2\Big) \\
&+Ep_2\theta'(s)^2\Big(-u''(s,t) + \theta'(s)w'(s,t) + \theta''(s)w(s,t)\Big)^2 \\
&+Ep_7\theta'(s)^2\left(\theta'(s)\phi(s,t) + v''(s,t) + \theta'(s)^2 v(s,t)\right)^2
\end{aligned} \tag{8.3}$$

$$
\begin{aligned}
\hat{T} = m\Bigg( & x_0^2\Omega^2 + 2x_0\Big(\Omega\cos(\theta(s))u(s,t) - \Omega\sin(\theta(s))w(s,t) + \dot{v}(s,t)\Big)\Omega \\
& + \Big(\Omega\cos(\theta(s))u(s,t) - \Omega\sin(\theta(s))w(s,t) + \dot{v}(s,t)\Big)^2 \\
& + \Big(\Omega\sin(\theta(s))v(s,t) + \dot{w}(s,t)\Big)^2 + \Big(\dot{u}(s,t) - \Omega\cos(\theta(s))v(s,t)\Big)^2\Bigg) \qquad (8.4) \\
& + J_y\Bigg( \sin^2(\theta(s))\phi(s,t)^2\Omega^2 + \frac{1}{2}v(s,t)^2\theta'(s)^2\Omega^2 - \frac{1}{2}\cos(2\theta(s))v(s,t)^2\theta'(s)^2\Omega^2 \\
& - \cos(2\theta(s))w(s,t)^2\theta'(s)^2\Omega^2 - \cos(2\theta(s))u'(s,t)^2\Omega^2 + \frac{1}{2}\cos(2\theta(s))\Omega^2 + \frac{\Omega^2}{2} \\
& + \sin(2\theta(s))u'(s,t)\Omega^2 + \sin(2\theta(s))v(s,t)\theta'(s)v'(s,t)\Omega^2 + 2\sin(\theta(s))\phi'(s,t)u'(s,t)\Omega \\
& + 2\cos(\theta(s))\theta'(s)\dot{v}(s,t)\Omega + 2\sin(\theta(s))v(s,t)\theta'(s)^2\dot{w}(s,t)\Omega + 2\cos(\theta(s))\phi'(s,t)\Omega \\
& + 2\sin(\theta(s))\theta'(s)\dot{v}(s,t)u'(s,t)\Omega - w(s,t)\theta'(s)\Big(2\sin(\theta(s))\phi'(s,t) \\
& + 2\sin(\theta(s))\theta'(s)\dot{v}(s,t) + \Omega\Big(\sin(2\theta(s)) - 2\cos(2\theta(s))u'(s,t)\Big)\Big)\Omega \\
& + 2\sin(\theta(s))\phi(s,t)\Big(\Omega\sin(\theta(s))v(s,t)\theta'(s) + \dot{w}(s,t)\theta'(s) - \dot{u}'(s,t) \\
& + \Omega\cos(\theta(s))v'(s,t)\Big)\Omega - 2\sin(\theta(s))v(s,t)\theta'(s)\dot{u}'(s,t)\Omega + \theta'(s)^2\dot{v}(s,t)^2 \\
& + \theta'(s)^2\dot{w}(s,t)^2 + \phi'(s,t)^2 + \dot{u}'(s,t)^2 + 2\theta'(s)\dot{v}(s,t)\phi'(s,t) - 2\theta'(s)\dot{w}(s,t)\dot{u}'(s,t)\Bigg) \\
& + J_x\Bigg(\Omega^2\cos^2(\theta(s)) - \Omega^2v'(s,t)^2\cos^2(\theta(s)) + 2\Omega\theta'(s)\dot{v}(s,t)\cos(\theta(s)) \\
& + 2\Omega\phi'(s,t)\cos(\theta(s)) - 2\Omega\theta'(s)\dot{w}(s,t)v'(s,t)\cos(\theta(s)) + 2\Omega v'(s,t)\dot{u}'(s,t)\cos(\theta(s)) \\
& - 2\Omega w(s,t)\theta'(s)\dot{v}'(s,t)\cos(\theta(s)) + 2\Omega u'(s,t)\dot{v}'(s,t)\cos(\theta(s)) + \Omega^2\sin^2(\theta(s)) \\
& - \Omega^2\sin^2(\theta(s))\phi(s,t)^2 - \Omega^2\sin^2(\theta(s))v(s,t)^2\theta'(s)^2 + \theta'(s)^2\dot{v}(s,t)^2 + \phi'(s,t)^2 \\
& + \dot{v}'(s,t)^2 - 2\Omega\sin(\theta(s))w(s,t)\theta'(s)^2\dot{v}(s,t) - 2\Omega\sin(\theta(s))w(s,t)\theta'(s)\phi'(s,t) \\
& + 2\theta'(s)\dot{v}(s,t)\phi'(s,t) + 2\Omega\sin(\theta(s))\theta'(s)\dot{v}(s,t)u'(s,t) + 2\Omega\sin(\theta(s))\phi'(s,t)u'(s,t) \\
& - 2\Omega\sin(\theta(s))v(s,t)\theta'(s)\Big(\theta'(s)\dot{w}(s,t) + \Omega\cos(\theta(s))v'(s,t) - \dot{u}'(s,t)\Big) \\
& - 2\Omega\sin(\theta(s))\phi(s,t)\Big(\Omega\sin(\theta(s))v(s,t)\theta'(s) + \dot{w}'(s,t)\theta'(s) \\
& + \Omega\cos(\theta(s))v'(s,t) - \dot{u}'(s,t)\Big) - 2\Omega\sin(\theta(s))\dot{v}'(s,t)\Bigg)
\end{aligned}
$$